Co-production of hydrogen and ethylene in an oxygen permeable membrane reactor

by

Faris Ihab Elmanakhly

A thesis
presented to the University of Waterloo
in fulfillment of the
thesis requirement for the degree of
Master of Applied Science
in
Mechanical and Mechatronics Engineering

Waterloo, Ontario, Canada, 2022

AUTHOR'S DECLARATION

I hereby declare that I am the sole author of this thesis. This is a true copy of the thesis, including any required final revisions, as accepted by my examiners. I understand that my thesis may be made electronically available to the public.

Abstract

The demand for low-carbon hydrogen keeps increasing. Hydrogen production from water splitting attracts attention due to the easiness of hydrogen purification from hydrogen-water mixtures and the flexibility of renewable energy integration. A potential technology is oxygen permeable membrane-supported water splitting. The membrane separates oxygen from hydrogen and pushes the thermodynamic equilibrium for higher water conversion ratios. Meanwhile, the call for a more sustainable and less energy-intensive process for ethylene production has always been there. Integrating oxidative coupling of methane (OCM) to membrane-supported water-splitting technology can utilize the oxygen from water splitting to co-produce higher value products (e.g., ethylene).

The technology investigated uses catalysts to increase the number of active sites on the membrane surface, which facilities the production rates and selectivity. On the feed side, the oxygen incorporation process is through the gaseous oxygen and oxygen vacancies at the membrane surface to form lattice oxygen. Then the lattice oxygen diffuses through the membrane driven by potential chemical gradients. Once the lattice oxygen reaches the sweep side, a reaction between lattice oxygen and electron holes at the membrane surface releases gases oxygen. The final step includes the mass transfer of gases oxygen from the membrane surface (sweep side) to the gas (methane) stream, which provides the necessary oxygen molecule for OCM reactions to convert methane to higher hydrocarbons such as ethane and ethylene. The entire process can be driven by renewable energy to co-produce hydrogen and ethylene with limited CO_2 production, thanks to the high selectivity catalysts.

This research develops a high-fidelity membrane reactor model that combines the microkinetic of water splitting, catalytic OCM reactions on the membrane surface, and the charged species diffusion across the membrane. The model helps evaluate the effect of using an oxygen-permeable catalytic membrane reactor on the co-production of ethylene and hydrogen. The results show that using a membrane reactor for this process provides a more controlled oxygen inlet concentration (or partial pressure), increasing ethane and ethylene production rates while enhancing the water conversion ratio. The membrane reactor achieved a C_{2+} yield of 25.64 %, which lies in the industrial range for the C_{2+} yield estimated in this research. This achieved C_{2+} yield promotes this technology to be industrially applicable.

Acknowledgements

I have learned so many things from everyone who contributed to this journey during my graduate program. I want to express my most profound appreciation and sincere gratitude to my supervisor Dr. XiaoYu Wu for his assistance at every research project stage. I have significantly benefited from his wealth of knowledge. I am incredibly grateful that he offered me this opportunity and continued faith in me throughout my masters. I learned from him to always be eager to achieve better not just academically but in my personal life too.

I want to thank my master's thesis committee members, Professor Michael Fowler, Dr. Zhao Pan, and my supervisor Dr. XiaoYu Wu for their feedback and contribution to getting the best version of this research thesis.

Additionally, I would like to extend my sincere thanks to Professor Michael Fowler and Dr. XiaoYu Wu for their academic supervision and Robert Stasko (CEO of Science Concepts International) for his industrial supervision of the Hydrogen business Council project. Working on this project allowed me to understand the importance of the transition into a hydrogen economy linked tightly to my research and contacted various field representatives.

I would also like to thank my colleagues in the greener production research team led by Dr. XiaoYu Wu at the University of Waterloo for their contributions to the field and their valuable insights.

During this uncertain time, it is also essential to recognize the people who made things slightly less uncertain, remind you that everything happens for a reason, and direct you back to the right path. I am grateful for having supportive parents and family who made so many unconditional sacrifices throughout the years, and my only wish is to make them proud. Without their tremendous understanding and encouragement in the past few years, it would be impossible to complete my studies. I also want to thank my friends and colleagues for their mental and moral support along the way.

Lastly, I would like to express how privileged and honored I feel for being a graduate student at Waterloo. My gratitude extends to the MME department at the University of Waterloo for the funding opportunity to undertake my studies.

Table of Contents

List of Figures

List of Tables

Chapter 1

Literature review

1.1 Chapter introduction

Interest in producing hydrogen in an efficient and low emissions process has gradually increased. Various governmental and non-profitable organizations are considering hydrogen as the future fuel. According to the international energy agency (IEA), around 7.2 exa-joules of hydrogen are used every year in global industries [1]. The stats show that most of the global hydrogen production is from hydrocarbons (around 96%), which results in around 500 megatonnes of CO_2 emitted. Water electrolysis only takes a small portion of the hydrogen production market (around 4%) [2].

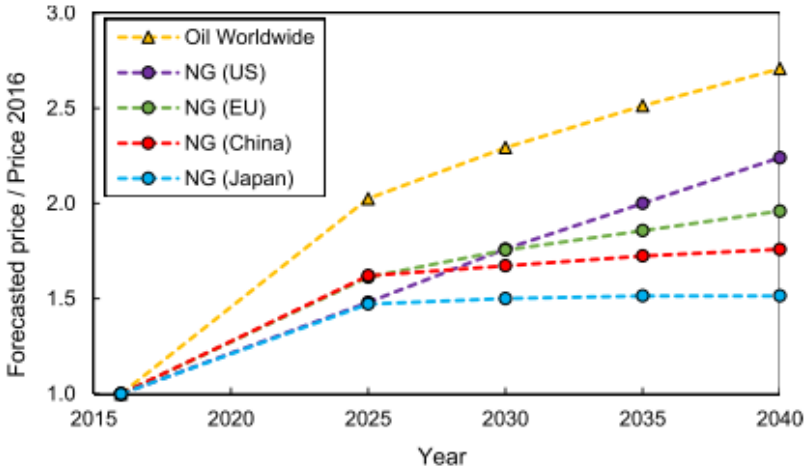

Figure 1-1: Forecast for the normalized price of oil and natural gas (2016 to 2040) [3]

In addition, the price of oil has been gradually increasing in the last year compared to natural gas; this trend is forecasted to continue according to IEA, and as shown in *Figure* 1-1. Natural gas shows a higher level of abundance than oil in the upcoming years [3], which nominates it to be an alternative, especially in the production of hydrocarbons.

The development and availability of technologies that allow for the transformation of natural gas into value-added products nevertheless add a novel dimension to the capabilities of the chemical processing industry.

The co-production of hydrogen and ethylene has been a research topic with high economic potential and a one step closer to zero-emissions energy production. Both products have their contributions to the petrochemical & energy industry. Combining water splitting and oxidative coupling of methane (OCM) in an oxygen-permeable membrane reactor is a promising technology investigated in this research. The membrane reactor technology combines the whole process into one unit without the mechanical movements of the reactor. Economic feasibility, thus, can be achieved. Additionally, the oxygen permeable membrane can shift the thermodynamic equilibrium to split water further to produce hydrogen and increase the ethylene selectivity.

1.2 Ethylene (C_2H_4)

1.2.1 Ethylene production importance

Ethylene is one of the most essential petrochemically derived monomers [4]. 149.7 million tons of ethylene were produced in 2017 worldwide [5]. Ethylene has various industrial uses as it is used directly in polyethylene plastics used in food packagings construction components such as high-efficiency windows, piping, and electrical conduits. The ethylene industry's estimated current global market exceeds 330 billion pounds per year, representing a $200+ billion annual market [6].

1.2.2 Current production methods of ethylene

The petrochemical industry is familiar with steam cracking or thermal cracking to produce ethylene. The process involves heating a feedstock to high temperatures over a catalyst (such as ZSM and SAPO catalysts) [7,8]. Under typical conditions, steam cracking of ethane to ethylene records a conversion rate of around 70 % and 50 % of ethylene yielding [9]. The feedstocks used in the process vary globally; the U.S. and the Middle East use ethane (gas phase) as the primary feedstock. The rest of the world predominately relies on naphtha (liquid phase) [6]. There has been a noticeable increase in the global share of ethane as a feedstock globally in recent years due to its oversupply since the shale gas revolution. The domination of ethane over naphtha can be linked to ethane's relativity lower price than naphtha (18 cents per gallon) [10].

The steam cracking process involves homogeneous pyrolysis, which originates from converting steam-diluted alkanes at high temperatures (approximately 800 °C) in reactor tubes. The feed is preheated with steam up to the initial cracking temperature (500–680 °C). Subsequently, the mixed stream is fed into a high-temperature reactor (750–875 °C) to complete the steam pyrolysis, with residence times of 0.1– 0.5 s. The feed is cracked into small olefins and di-olefins. The effluent has to be quenched within 0.02–0.1 s to avoid product degradation due to the high reactivity of the products. The products are separated by distillation and absorption processes [11].

1.2.3 Limitations of the current ethylene production methods

Several issues accompany the current methods of ethylene production. Firstly, the unpredictable oil prices and the global oil market directly affect the ethylene production rates. Studies [12,13] report how the noticeable price of crude oil -which is currently the primary source of ethylene produced globally- has pressured ethylene production. Secondly, current ethylene production methods are energy-intensive processes. The total energy demand of the produced ethylene is 16 GJ/t (in the case of ethane as a feedstock) and 23 GJ/t (naphtha is used as a feedstock) [9]. Steam cracking is an endothermic process that is an energy-intensive process, and the process requires significant heat input by burning the undesired reaction products for the endothermic dehydrogenation reactions, which results in severe nitrogen oxides (pollutants) [14]. Thirdly, CO_2 emission is another big concern. Steam cracking is estimated to produce nearly 300 million tons of annual carbon dioxide emissions [15]. In another source, the steam cracking process is estimated to produce around 2.6 tons of CO_2 per ton of ethylene produced [16]. These issues make research into alternative technologies more appealing. Intensifying the direct methane conversion methods can lead to more effective and economical ways to produce ethylene.

1.3 Hydrogen (H_2)

1.3.1 Hydrogen production importance

Worldwide natural gas consumption has been rising over the past 20 years. In 2019, natural gas consumption worldwide amounted to nearly 3.9 trillion cubic meters; this resulted in around 36.8 billion tons of carbon dioxide emissions estimated by the global carbon project 2019 [17]. The reality of climate change is a pressing concern and demands action. Global efforts are underway to decrease CO_2

emissions by relying more on renewables, improving generation and end-use efficiency, and, more importantly, switching to low carbon fuels [18].

Hydrogen can be an alternative fuel to reduce the fossil fuel dependency of various sectors such as transportation or heavy industry. Hydrogen from renewables (such as wind, solar, geothermal, and biomass) and low carbon resources (such as nuclear energy) can replace fossil fuel-based feedstocks in CO_2 emission-intensive sectors. The utilization of renewable and low carbon resources to produce hydrogen can effectively contribute to the reduction of carbon emissions as these sources have the lowest recorded carbon intensity (0 to 0.6 kg CO_2-eq (CO_2 equivalent)/kg H_2) [19]. In addition, hydrogen can be combusted in a gas turbine or used directly in a fuel cell to generate work/electricity without GHGs. Hydrogen can also help reduce urban emissions (i.e., SO_x, ozone, PM 2.5, PM 10) [19].

The primary usage of hydrogen in the industry is adhered to the chemical industry, with more than 50% used for ammonia production, which can be further used to produce fertilizers (as shown in *Figure* 1-2). Several market projections predict a substantial increase in the H_2 global market from 10 exa joule to around 78 exa joule. The substitutional increase in H_2 production can be implemented in other industrial sectors, including power generation, transportation (fuel cell cars, locomotive trains), and even buildings heating and internal powering.

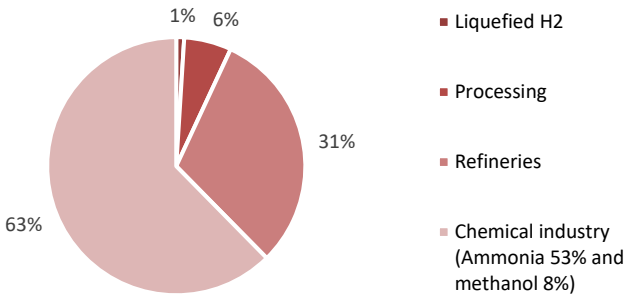

Figure 1-2: Global hydrogen market 2013 [20]

Global efforts are pacing to develop a road map for hydrogen economy transition. A shift towards a "hydrogen economy" can reduce carbon emissions, increase penetration of variable renewable power generation into the grid, and improve energy security. Hydrogen production fulfills this economy's

significant energy needs while reducing urban pollution emissions and the overall carbon footprint. Several countries and regions are developing roadmaps for the deployment of hydrogen technology and building demonstration-scale projects for either hydrogen production or consumption. In Canada, the hydrogen strategy has been considered at the federal level. In 2019, Natural Resources Canada (NRCan) issued a report on potential pathways for hydrogen implementation. The report encourages the establishment of research goals, the development of codes and standards related to hydrogen deployment, and international information sharing and collaboration [21]. The UK Climate Change Act is committed to a 100% emissions reduction from 1990 by 2050. To achieve the necessary carbon reductions in the energy supply to meet this target, the UK Committee on Climate Change has released a series of recommendations for the implementation of hydrogen [22]. Japan is deploying technologies for hydrogen utilization, with 250,000 Combined Heat and Power (CHP) units in buildings and 2,400 hydrogen vehicles [23].

1.3.2 Current production methods of hydrogen

There are various methods to produce hydrogen on an industrial level. As shown in *Figure* 1-3, most industrial hydrogen is produced from natural gas, as this method accounts for around 48 % of the global hydrogen production.

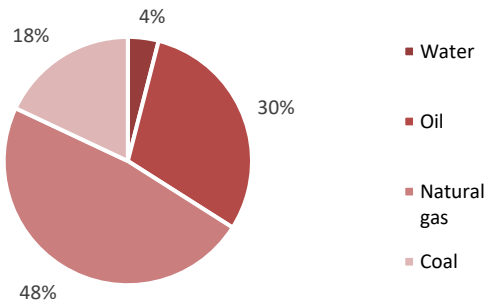

Figure 1-3: Sources of hydrogen production in 2012 [2]

Steam-methane reforming (SMR) is an advanced and mature industrial process built upon the existing pipeline infrastructure for a cost-effective natural gas supply [24]. Methane is the primary gas component in natural gas, which reacts with steam on catalysts (such as nickel or noble metal catalysts)

at high temperatures (700°C - 1000°C) and pressures (3 - 25 bar) to derive syngas. The syngas is made up primarily of carbon monoxide and hydrogen, along with a small amount of carbon dioxide [25]. Next, the syngas undergoes the water gas shift (WGS) reaction, catalyzed by metals or metal oxides (e.g., Fe [26][27][28]and Cu[29]) to convert carbon monoxide with steam to carbon dioxide and additional hydrogen [30]. Finally, the pressure-swing absorption (PSA) separates hydrogen from carbon dioxide and other impurities with CCS.

The chemical reactions involved in the SMR are:

Steam-methane reforming reaction

$$CH_4 + H_2O \rightarrow CO + 3H_2 \qquad \Delta H_r = 206 \text{ kJ/mol} \qquad (1\text{-}1)$$

Water-gas shift reaction

$$CO + H_2O \rightarrow CO_2 + H_2 \qquad \Delta H_r = -41 \text{ kJ/mol} \qquad (1\text{-}2)$$

Where,

- ΔH_r: the standard reaction enthalpy for the specific reactions.

Coal and biomass gasification can also produce hydrogen and power, liquid fuels, and other chemicals [31,32]. For coal gasification, coal ($CH_{0.8}$) reacts with oxygen, steam, or CO_2 under high temperatures and pressures, resulting in syngas, as shown in *Eqn. (1-3)* [33]:

$$2CH_{0.8} + O_2 + H_2O \rightarrow CO + CO_2 + 1.8H_2 \qquad (1\text{-}3)$$

Next, solid impurities such as dust are removed, followed by the WGS reaction to convert carbon monoxide to carbon dioxide while producing more hydrogen from steam [33]. A separation process must be employed to achieve a high purity hydrogen gas product. Traditional gas separation methods include cryogenic distillation, pressure swing adsorption, and membrane separation. Membranes such as polymeric membranes, metal-organic framework (MOF) membranes, zeolite membranes, and mixed

ionic and electronic conducting membranes have been developed with higher energy efficiency and intensified processes [34–36].

The water electrolysis process (also called water splitting reaction) involves decomposing water in its liquid and gas state into oxygen and hydrogen gas by introducing an electric current (as shown in *Eqn.* (1-4)*)*. The easiness of hydrogen purification from hydrogen-water mixtures made this approach more desirable, and it is now the only water splitting process that is economically utilized [37].

$$2\mathrm{H}_2O \rightarrow 2H_2 + O_2 \qquad \Delta H_r = 285.85 \text{ kJ/mol} \qquad (1\text{-}4)$$

There are three major technologies for electrolysis, each of which has a respective fuel cell technology: alkaline electrolyzers or fuel cells (AEL or AFC), polymer electrolyte membrane (PEM) electrolyzers/fuel cells, and solid oxide electrolyzers (SOEC or SOFC). Each technology has its benefits and drawbacks. Alkaline electrolysis is currently the most mature and widespread technology among the three technologies. The solid oxide electrolysis is still primarily in its development phase, with few commercial systems available.

Table 1-1 : Comparison of various hydrogen production methods [38]

Parameter	SMR	Coal Gasification	Electrolysis
Efficiency	74%-85% [39]	60%-75% [39]	46%-81% [40]
Hydrogen cost [US$/kg] [39,41]	2.27 (with CCS) 2.08 (no CCS) 2005 dollars	1.63 (with CCS) 1.34 (no CCS) 2005 dollars	5.78-23.27 (solar PV, 2007 dollars) 5.10-10.49 (solar thermal, 2007 dollars) 5.89-6.03 (wind, 2005 dollars) 2.17-2.63 (nuclear, 2007 dollars)

Lifecycle $CO_{2\text{-eq}}/H_2$ [kg/kg] [42]	11.893	11.299	0.970 (wind) 2.412 (solar)

1.3.3 Limitations of the current hydrogen production methods

SMR process for hydrogen production has a relatively low cost per kg of H_2 ($ US 1.6/kg H_2) compared to other processes such as electrolysis ($ US 4.14 – 5.12 /kg H_2). The relatively cheaper cost of hydrogen production from natural gas reforming is the low feedstock price of around $6.09/mmBTU ±50% [43]. However, the SMR process releases significant life cycle greenhouse gas (GHG) emissions ranging between 11,000–13,000 $tonnes_{CO2\text{-}eq}/tonnes_{H2}$[44]. Coal gasification might be an economically viable approach providing the highest potential to become competitive on a large scale. However, coal gasification also has relatively high CO_2 emissions (around 200 gCO_2e/MJ_{H2}) than a traditional coal plant [45].

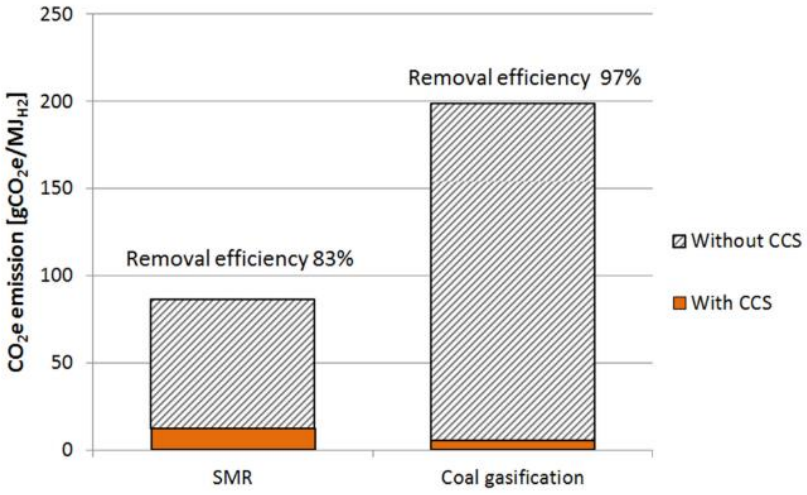

Figure 1-4: Emission of CO_2 during hydrogen production through SMR and coal gasification with and without CCS [46]

Figure 1-4 shows the CO_2 emissions released during hydrogen production through SMR and coal gasification. The figure also shows the significant impact of applying the carbon capture & storage (CCS) system on these processes. All the different technologies for the electrolysis of pure water to produce hydrogen share the same limitations. One of these limitations involves the requirement of excess energy in the form of overpotential to overcome the various activation barriers present. In addition, electrolysis is normally a more capital expensive method of hydrogen generation than steam reforming; the electricity required to split the water into hydrogen and oxygen accounts for around 80% of the cost of hydrogen generation [47].

1.4 What is next?

Various limitations hinder the current industrial production of higher hydrocarbons through the conversion of natural gas (methane is the principal component) and the efficient generation of hydrogen as an energy carrier. CO_2 emission has been a major global warming contributor [48]. International Energy Agency (IEA) predicts that the CO_2 emissions rate will double by 2030 since its value was reported in 1990 [49]. Seeing as the current industrially applicable production methods for both hydrogen and ethylene have a significant CO_2 emission output, as showcased in *Sections 1.2.3* and *1.3.3*, it is necessary to investigate processes that involve the co-production of ethylene and hydrogen as a by-product in a more economical way and, more importantly, more environmentally friendly.

Natural gas valorization, which involves ethylene production through the conversion of methane, overcomes the limitations of traditional ethylene production, such as the steam cracking process. Using natural gas (methane) as a feedstock (instead of ethane) in a direct catalytic reaction in a membrane reactor (instead of a furnace) can help decrease the energy consumption noticeable in the case of steam cracking and increase the selectivity toward ethylene production. The ethylene production from natural gas can occur via two distinct routes, discussed next. An indirect route involves the conversion of natural gas into syngas (a mixture of CO and H_2), and a direct route involving the oxidative coupling of methane (OCM) aims to produce ethylene. This reaction involves various homogeneous and heterogeneous reactions in the primary and secondary steps explained further in *Section 1.6*.

1.5 Direct & indirect methane conversion to ethylene

The various attempts to shift the energy production industry from fossil fuel-based to a cleaner energy source have developed much interest in converting methane to value-added hydrocarbons and chemicals efficiently and cost-effectively.

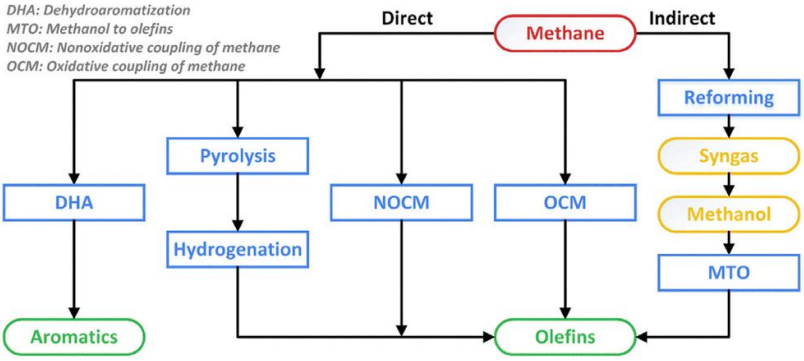

Figure 1-5: Methane conversion scheme [50]

According to *Figure 1-5*, there are two paths for methane conversion to olefins (ethylene, propylene, and butadiene) [51]. The indirect route involves the conversion of natural gas into syngas (a mixture of CO and H_2). A secondary step occurs where higher hydrocarbons are further cracked to produce ethylene. More commonly known in the industry as methanol-to-olefins (MTO), this process occurs via a multistep catalytic reaction involving SAPO-34, ZSM-5, and ZSM-22 as catalysts, as reported by the literature [50]. Various parties have already commercialized the MTO process, including the Dalian Institute of Chemical Physics (DICP) [52] and several other companies that have developed (but not commercialized the technology), including ExxonMobil [7]. This indirect route for methane conversion to olefins currently has more than 60% of the capital cost for methane reforming to syngas [53].

The direct methane conversion (DMC) processes to chemical and fuels trounce the conventional syngas production approach when it comes to the complexity of multi-step reaction and energy losses penalties. However, this technology cannot be considered industry robust due to the high inertness of C-H bonds in methane and difficulty controlling the reaction selectivity.

Several DMC processes depend on the heterogeneous functionalist of CH_4 and showed promising conversion performance. Some of these processes are methane aromatization (MA), Non-oxidative

methane conversion, and oxidative coupling of methane (OCM) [54]. Other DMC processes involve homogeneous chain-growth of CH_4, such as methane cracking and homogeneous methane conversion, but these are not the focus of this study. Firstly, MA is a process that involves the production of aromatic compounds, which include C_2H_6 (benzene) and $C_{10}H_8$ (naphthalene) reactions. The MA is usually processed in non-oxidative conditions and performs well when using a catalyst that combines metal oxides and zeolites, such as Mo/ZSM-5 zeolites. A bi-functional mechanical activates CH_4 on the formed MoC sites. The oligomerization reaction follows on the acidic sites in zeolites [55].

$$6CH_4 \rightarrow 9H_2 + C_6H_6 \qquad \Delta H_r = 531 \text{ kJ/mol} \qquad (1\text{-}5)$$

One of the limitations of this process is the deposition of coke on acidified sites, which eventually leads to the deactivation of the catalyst and limits the thermodynamic yield of the reaction. Recent attempts to overcome thermodynamic limitations on aromatic yields by selective removal of the hydrogen coproduct include the development of membrane reactors [56,57]. Similarly, the direct non-oxidative methane conversion is used to produce benzene predominantly with only little olefins in the absence of O_2. Most of the catalysts used in this process are based on Mo/zeolite catalysts. Like the MA process, the direct nonoxidative methane conversion is accompanied by high coke yields and the catalyst deactivation caused by coking. In addition, employing a catalytic direct non-oxidative methane conversation includes many steps that involve compression and separation sections for product recovery and purification and recovery and recycling of unreacted methane, along with refrigeration, power generation, and utility sections. In this research, the attention is shifted toward an oxidative couple of methane as a direct process for methane conversion into higher hydrocarbons. The process has shown high potential since its discovery in the 1980s. However, it has not been commercially practiced for various reasons discussed in the following sections.

1.6 Oxidative coupling of methane (OCM)

1.6.1 Process

As discussed in *Section 1.2.3*, finding a more accessible source of ethylene production that overcomes the utilization of endothermic, high input temperatures, and costly stream reforming processes is indispensable to moving forward with the energy sector. Many laboratories have

investigated natural gas conversion due to its potential to reestablish the higher carbons production industry. Converting the methane component of natural gas into less volatile and more valuable products has attracted interest in recent years. OCM is considered one of the most promising processes that effectively utilize the pattern of natural gas cleanly and economically through the direct route of methane conversion into higher valuable hydrocarbons such as ethane or ethylene [58]. The overall OCM reaction involves the following:

$$2CH_4 + O_2 \rightarrow C_2H_4 + 2H_2O \qquad \Delta H_r = -209.3 \text{ kJ/mol}CH_4 \qquad (1\text{-}6)$$

The primary reaction is accompanied by many homogeneous and heterogeneous reactions in the primary and secondary steps [59].

$$2CH_4 + \frac{1}{2}O_2 \rightarrow C_2H_6 + H_2O \qquad \Delta H_r = -20.2 \text{ kJ/mol}CH_4 \qquad (1\text{-}7)$$

$$CH_4 + 2O_2 \rightarrow CO_2 + 2H_2O \qquad \Delta H_r = -802.6 \text{ kJ/mol}CH_4 \qquad (1\text{-}8)$$

$$CH_4 + \frac{1}{2}O_2 \rightarrow CO + 2H_2 \qquad \Delta H_r = -36.0 \text{ kJ/mol}CH_4 \qquad (1\text{-}9)$$

In addition, the OCM reaction involves the reaction of CH_4 and O_2 over a heterogeneous catalyst at elevated temperatures to form the desired products. The process overcomes the issue of energy loss by avoiding the synthesis of gas or syngas (H_2 /CO mixture) as an intermediate, which is typically followed by the conversion into other chemicals by Fischer-Tropsch reactions or via methanol as a second intermediate [60].

OCM reactions occur in high-temperature conditions that range between 900-1200 K, depending on the catalyst used. Higher temperatures are essential to activate the C-H bond in the methane molecule. The main feed components of the OCM reactions involve high concertation of CH_4 and O_2 to stay in the safe range and limit the nonselective gas-phase reactions. The molar ratio of CH_4/O_2 ranges between 3-12 with or without diluents at moderate pressures (generally atmospheric pressure) [61].

The mechanism of OCM is based on the so-called heterogeneous-homogeneous (H-H) mechanism [62]. Based on the H-H mechanism, the correlation between the adsorption energy of methane and its activation energy on oxide surfaces has been established using theoretical calculations.

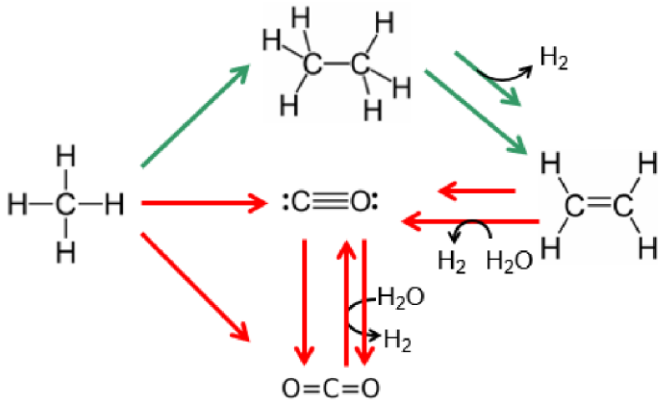

Figure 1-6: Oxidative coupling of methane (OCM) tradition reaction scheme [63]

The selective route of CH_4 involves the direct conversions to C_2H_6, C_2H_4, and H_2O in O_2 and a suitable catalyst [54]. The first step involves the abstraction of H from CH_4 by the catalyst to form methyl radicals (CH_3•) [64]. The review paper by Lunsford in 1995 [62] suggests that the following step involves the coupling of two CH_3• which leads to the creation of ethane. Dehydrogenation of ethane then produces ethylene. According to Conway et al.[65] This reaction is accompanied by the formation of C_2 hydrocarbons by the addition of CH_3• to C_2H_4.

1.6.2 OCM limitations

Despite how robust the OCM reactions seem to be on a research level. The process is still considered inadequate for industrial application. Several limitations arise that hinder the adsorption of the OCM process as an industrial method of ethylene production. Parishan et al. [13] and Jaso et al. [66] claim that a 30 % C_{2+} yield is necessary to make OCM competitive. While Kuo et al. [67] claim in their work that a conversion above 35 %, coupled with a C_{2+} selectivity above 85%, renders OCM economically attractive. However, the OCM process is not quite there yet.

The most impactful limitation that the OCM faces is the reported C_{2+} yield values. As stated in *Section 1.6.1*, methane is converted to ethane in a primary step. However, breaking the C-H bond requires high temperatures above 750 °C in most cases, causing the enhancement of undesired complete

and incomplete combustion reactions, which will result in a limitation in the overall C_{2+} selectivity. Along with those mentioned above, the oxidative and the non-oxidative dehydrogenation of ethane into ethylene during the OCM secondary steps can decrease the selectivity of C_{2+} even further. Due to the complexity of the set of primary and secondary reactions of the OCM process. Low yields value always accompanies the process of OCM in the published experimental work, as most of the published studies report yields that range between 20-25% [59].

Furthermore, dissociating one hydrogen from methane molecule (CH_3-H) to form methyl radial is complex due to the scission of the first C-H bond (ca. 435 kJ/ mol). In order to overcome this limitation, the activation energy required for methane activation has to be higher than the other significant products included in the reaction. This can lead to non-selective and sequential oxidation of desired products, especially in the absence of a selective catalyst; a tradeoff must usually happen for OCM reaction at high temperatures over an active catalyst between conversion and product selectivity. In addition, as pointed out by Cruzprat et al. [68], the direct route to H_2 and C_2H_4 will be thermodynamically disfavored, which means it would require high temperatures, consequently resulting in poor selectivity. Another economic limitation highlighted by Jiang et al. [58] is that ethylene produced by OCM reaction with an abundant supply of methane is still relatively more expensive than other industrial alternatives.

Finally, the limitations mentioned above are why great efforts have been carried out to improve the performance of the OCM process since the 1980s. The complexity of the OCM reaction relates to two important factors. Firstly, the necessity of developing novel catalysts which could contribute to maintaining higher selectivity toward the desired product. OCM catalyst and their impact will be discussed in *chapter 2*. Secondly, developing suitable reactors that can operate at low temperatures with high methane conversion and high selectivity is essential to maintain a high yield for the product. Also, it will help minimize the CO and CO_2 generated from the undesirable surface and gas-phase combustion reactions and, more importantly, avoid the intrusion of the homogenous gas phase free radical (i.e., combustion) that can be a determinant factor for the C_{2+} products. Various efforts were directed toward developing the reactor configuration that houses the OCM process. Some of these developed involves using a membrane reactor discussed in *Section 1.10*.

1.7 Membranes

1.7.1 Principle

A membrane can be defined as a region of discontinuity interposed between two phases. Membranes can be both a permeable or semi-permeable medium and are characterized by permeation and perm-selectivity. In other words, the membrane may have the ability to transport one component more readily than others due to the differences in physical and chemical properties between the membrane and the permeating components [69].

The membrane separation process is characterized by using a membrane to accomplish a particular separation. The membrane can separate the feed stream into a retentate and permeate by controlling the relative transport rates of various species, as shown in *Figure 1-7*. The separation process is evaluated regarding permeation rate or permeation flux (mol/m^2 s) [69]. The permeation flux is defined as the molar (or volumetric or mass) flow rate of the fluid permeating through the membrane per unit area, more in *Chapter 3*.

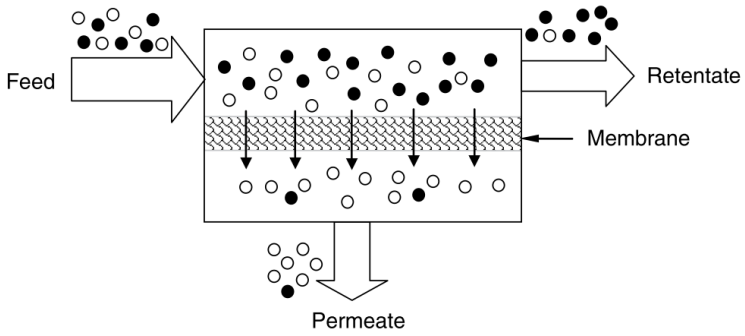

Figure 1-7: Membrane separation process [69]

1.7.2 Classification

Membranes can be classified according to different viewpoints. Membrane materials, morphology, the structure of the membranes, preparation methods, separation principles, and application areas are all criteria for membrane classifications. Membranes can be characterized based on their structure and separation principle, determining the membrane application. Based on this fact, membranes can be arranged into porous and dense (non-porous) membranes.

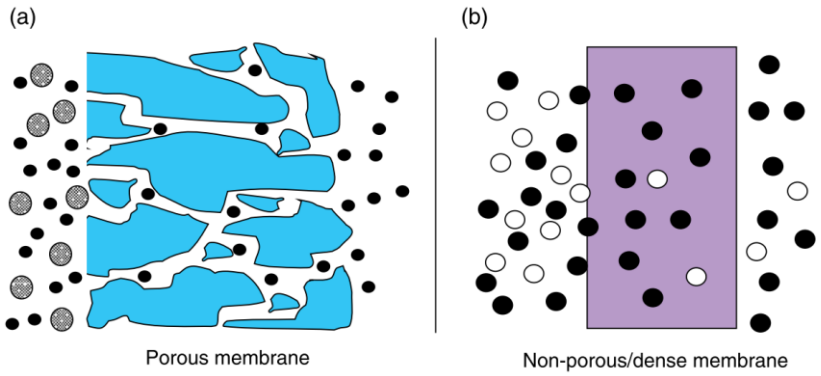

Figure 1-8: Porous membrane vs. dense membrane [69]

The porous membrane comprises a porous separation layer and induces separation by discriminating between particle (molecular) sizes. The porous ceramic membrane's separation characteristics (i.e., flux and selectivity) are directly impacted by pore size, thickness, and surface porosity [69]. One of the most significant industrial advantages of porous ceramic membranes is their cost, either membrane materials or membrane production. Thus, large-scale production for porous materials is more wildly standard.

Dense (non-porous) membranes are characterized by their dense separation layer. The separation process in this type of membrane happens due to differences in solubility or reactivity and the mobility of various species. A dense ceramic membrane contains crystalline ceramic materials such as perovskite or fluorite, a mixture of solid oxides and metals, and the mixed ionic electronic conducting property. This membrane type provides a high selectivity towards oxygen (or hydrogen) if the prepared membrane is dense and defect-free while impermeable to most other gases. The mechanism involves transporting the gas component (usually oxygen or hydrogen) in a dissociated or ionized form rather than conventional molecular diffusion [70].

Hazbun et al. [71] studied the effect of using a dense ceramic oxygen permeation membrane on the selectivity and conversion of the C_{2+} compounds in an OCM reaction. The study involved a two-layer tubular membrane, a 10 % Y_2O_3, 89% ZrO_2, 1% TiO_2 layer for oxygen permeation, and a $LiO/MgO/ZrO_2$ layer as the catalyst. The reactive tubular membrane is tested for methane conversion activity by placing the tube in a test apparatus that allows heated air or oxygen to flow outside the tube and the methane gas within the tube. The feed gas, including methane, is gradually introduced inside the tube with an inert gas carrier. The reaction of methane with the oxygen conducted through the mixed conducting membrane occurs at the catalytic Mn sites resulting in higher hydrocarbon products,

coproduct water, and H_2 and carbon oxides. The study concluded that C_{2+} yields much higher at 20-25% and around 50–60 % selectivity with a 35–45 % conversion rate at 700–750 ºC. Thus, it can be concluded that using a high oxygen permeable dense ceramic membrane with an OCM catalytically active surface is crucial to achieving high C_{2+} yields.

1.7.3 Performance

The overall performance is evaluated based on permeability, selectivity, and stability. High selectivity and permeability are both favored for ideal membranes. However, according to Tan et al. [69], a compromise must be made to enhance these two factors, negatively affecting the other. According to the same source, low permeability can be compensated to a certain extent by increasing membrane surface area. In contrast, low selectivity leads to multi-stage processes, which are not economical compared with established conventional processes.

1.8 Inorganic membranes (principle, classification, and configuration)

Inorganic membranes are characterized by high chemical and thermal resistances and high mechanical stability; they are applied in demanding applications. On the other hand, they exhibit the shortcoming of high cost because of their long and complicated production route in which multi-step high-temperature treatment is required. They usually consist of several layers from one or more different inorganic materials.

A porous substrate with large pores (1–15 μm for low flow resistance) but sufficient mechanical strength is used to support a thin selective layer for separation. Al_2O_3, ZrO_2, TiO_2, Si_3N_4, carbon, glass, and stainless steel are commonly used for macroporous support. In addition, a separation layer is also an essential layer of the inorganic membranes. The separation layer may be dense (non-porous), such as Pd-alloy membranes for hydrogen separation and mixed (electronic, ionic) conducting oxide membranes for oxygen separation, or porous, such as metal oxides and silicalite or zeolite membranes. A thin and defect-free separation layer is used to determine the flux and selectivity of inorganic membranes [69].

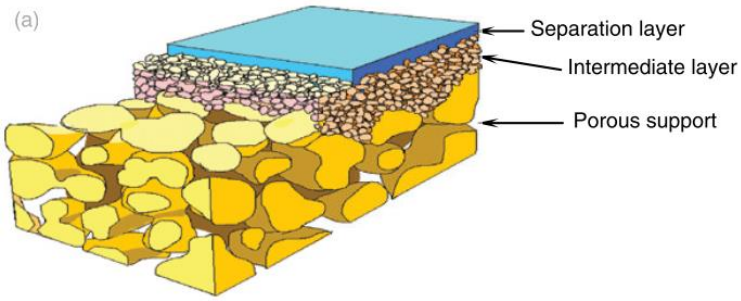

Figure 1-9: Multi-layered asymmetric structure of inorganic membranes [69]

Inorganic membranes can be produced in the flat disk, tubular, monolithic multi-channel, or hollow fiber configurations. The multi-channel monolithic form (which is shown in *Figure 1-10*) is developed to increase the mechanical robustness and the surface area-to-volume ratio to around 130– 400 m^2/m^3 compared with 30–250 m^2/m^3 for tubular designs; this gives more separation area per unit volume of the membrane element.

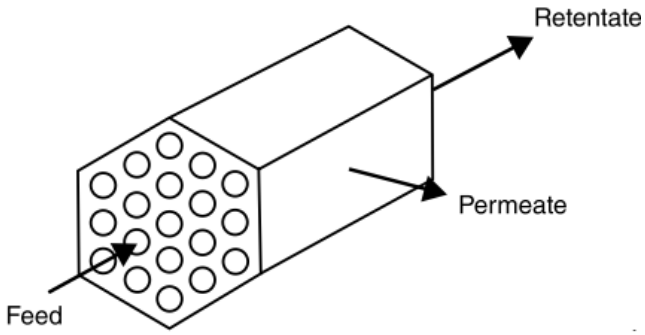

Figure 1-10: Multi-channel monolithic membrane [69]

In the monolithic membranes, the monolith bulk is made up of a porous support, and the separation layer is produced on the inner surface of the channels. Therefore, feed is introduced in the channels, and the permeate is obtained from the membrane wall.

1.9 Mixed ionic-electronic conductive perovskite membranes

Mixed ionic-electronic conductive (MIEC) perovskite membranes are inorganic membranes and attractive candidates for oxygen permeation. This membrane type is based on solid electrolytes' oxygen

ionic conduction performance and is commonly perovskite and fluorite materials. The temperature range for their application typically goes from 700 °C up to 1100 °C [72]. This type of membrane's selectivity towards oxygen avoids using an air separation unit usually required to feed pure oxygen into the reactor.

Perovskite membranes achieve higher oxygen fluxes than other membranes, such as fluorite membranes, by varying the cations and adding dopants. A subset of perovskite exhibits both ionic and electronic conductivities at elevated temperatures. Usually, alkaline-earth metal ions are doped in the A site to create oxygen vacancies, while transition metal ions in B sites improve the electronic properties [73].

When exposed to ample oxygen partial pressure gradient, the MIEC perovskite is oxygen selective-permeable and demonstrates high ionic and electronic conductivity and high thermal and chemical stability. The oxygen diffusion capabilities in perovskite materials are attributed to oxygen vacancies and the mobility of charged species, i.e., electrons, holes, lattice oxygen, and oxygen vacancies. The performance of an oxygen-permeable membrane for hydrogen and ethylene co-production is examined based on the following [74] :

(1) **High oxygen permeability**: the oxygen permeability is directly proportional to the hydrogen production rate on the feed side. Oxygen permeation depends on the ambipolar diffusion of ions and electrons/holes across the membrane.

(2) **High active surface area:** surface reactions are essential steps on both sides of the membrane; the overall C_{2+} formation and H_2O splitting performance depend on the surface reactions, such as the adsorption/desorption and heterogeneous gas-solid reactions.

(3) **Good chemical and mechanical stabilities**: the oxygen permeable membrane operates at elevated temperatures, especially the perovskite membrane, as the conduction of oxygen ions requires a high temperature (> 700 °C) since the process depends on the presence of oxygen vacancy sites that increase with temperature [75]. The stability of the membrane materials during heating/cooling and under long-term operations is of great importance for industrial applications.

(4) **Low operating temperature**: High operating temperature leads to higher surface reaction kinetics and better oxygen permeability. However, this enhancement is accompanied by higher operational costs

since more insulation materials are required to decrease heat loss. Nevertheless, optimization is also required to have the reactor operating at appropriate temperatures to achieve the best performances [76].

According to Wu et al. [37], this type of membrane can be implemented in water splitting technologies and integrated into Partial Oxidation of Methane (POM) to co-produce high purity hydrogen and syngas. The study also noted the relationship between the operating temperatures and the performance of the membrane reactor, which directly affects the hydrogen production rates. Mixed perovskite-type oxides were examined in the OCM process to convert methane into higher C_{2+} products such as ethylene and ethane [77].

1.9.1 Barium based perovskite (BCFZ)

Yao et al. [78] examined the BCFZ membranes morphology to determine its ability for oxygen separation. The paper included examining the phase structure of BCFZ membranes using a diffractometer with Cu radiation. In addition to that, the cross-section morphology of the membrane was studied using a field emission scanning electron microscope at an excitation voltage of 15 kV. The study results concluded that the BCFZ membranes adhere to a dense ceramic structure. The results also show how the oxygen permeability of the BCFZ membranes increased with increases in the operating temperature. The paper also examines the oxygen permeation flux of the membrane, and it shows an increasing trend initially and then a decrease with increasing Zr content.

A study by Jiang et al. [79] in 2010 examined (BCFZ) oxygen-permeable membrane reactor. The study involved increasing the hydrogen production rate by increasing the temperature and pressure difference and reducing gases such as methane to the permeate side to consume the permeated oxygen. A hydrogen production rate of 3.1 $cm^3\ min^{-1}\ cm^{-2}$ was obtained at 950 °C. Jiang et al. [79] explain that the continuous removal of oxygen from water dissociation led to continuously shifting the equilibrium to the product side. Furthermore, the methane feeding to the permeate side provided a more significant driving force for oxygen transport, which increases the amount of hydrogen produced.

1.9.2 Calcium based perovskite (LCF-91)

$La_{0.9}Ca_{0.1}FeO_{3-\delta}$ (LCF-91) is a ceramic-based mixed conducting oxide membrane. This type of membrane possesses a mixed ionic conductivity with prevailing electronic conduction. According to

the quantitative energy-dispersive X-ray spectroscopy (EDX) study, the stoichiometry of LCF-91 membrane material is shown in *Table 1-2*.

Table 1-2: Quantitative EDX results for LCF-91 membrane materials [80]

Elements	**La**	**Ca**	**Fe**
Atomic concentration [%]	42.41 ± 1.16	5.53 ± 0.56	52.06 ± 1.24
Calculated stoichiometry	0.885 ± 0.023	0.115 ± 0.011	1.09 ± 0.025

The Goldschmidt tolerance factor, TG, is often used to identify whether the chemical compound can form a stable perovskite lattice. LCF-91 has a tolerance factor in $0.954 < TG < 1.00$, indicating that at least the material LCF-91 is in a stable perovskite structure [81]. In this research, the focus would be on this type of perovskite membrane. The membrane will be used to develop the framework for the reactor design, which is modeled in *Chapter 3*.

The ability of LCF-91 membranes to enhance the water thermolysis reaction is investigated using different oxygen sources and sweep cases, in the case methane is added to the sweep side of the reactor. Wu et al. [80] performed water thermolysis experiments using 0.9 mm thick $La_{0.9}Ca_{0.1}FeO_{3-\delta}$ (LCF-91) perovskite membranes at 990 °C in a lab-scale button-cell reactor. LCF perovskite membranes are chosen for this investigation for their stability in various conditions. The paper concluded that the water thermolysis rate is enhanced when using the LCF-91 membrane, especially when fuel is added to the sweep gas.

1.9.3 Oxygen permeation in mixed ionic-electronic conductive membranes

According to Wu et al. [80], one of the ways to decrease the cost of H_2 production from water is to adopt a process that utilizes heat and chemical potential to drive the water-splitting. This process can be achievable by enhancing water thermolysis reaction by removing one of the products from the reaction zone using oxygen-permeable dense mixed ionic–electronic conductive (MIEC) membranes. This type of membrane makes the equilibrium reaction shift to the product side, which helps increase the reaction conversion beyond the thermodynamic limits [82]. Shifting the reaction equilibrium to the

product side also helps maintain high conversion at lower temperatures, avoiding the deactivation of catalyst and undesirable side reactions [83].

The oxygen permeation process through a perovskite mixed ionic-electronic conducting membrane involves several sub-steps: oxygen adsorption, dissociation, recombination, and charge transfer [84]. Since a perovskite material is an ideal structure that shows limited capabilities for producing oxide ions, the presence of point defects or imperfection is crucial for the bulk diffusion (lattice diffusion in oxides) to take place [85,86]. Kroger and Vink first adopted the concept of defects and their importance for mixed conduction ceramic materials [87]. Several defects may occur in a structure, such as vacancies and interstitial atoms. In this research, the focus is directed more toward the vacancies mechanism. The vacancy mechanism involves the presence of a vacancy in the site left by an atom or ion that is just moved from its normal position to an adjacent unoccupied lattice site. Many oxygen vacancies are formed by doping aliovalent cations [70]. The generated oxygen vacancies tend to be filled with oxygen atoms and the formation of two-electron holes, as shown in *Eqn.* (1-10).

$$\frac{1}{2}O_2 + V_O^{\bullet\bullet} \Leftrightarrow O_O^x + 2h^{\bullet} \tag{1-10}$$

Where the charged defects are defined using Kröger–Vink notation.

- O_O^x : lattice oxygen
- $V_O^{\bullet\bullet}$: oxygen vacancy
- h•: positive electron-hole

Electron holes are conducted when an electron deficiency arises in charges deviating from the standard lattice ions. In a mixed ion and electron conductor (or, in this case, mixed ionic-electronic conducting membrane), its overall conductivity performance arises from ionic and electronic defects contributions. When this type of membrane experiences an oxygen chemical potential gradient that is imposed on the membrane at high temperature, oxygen anions tend to permeate through the interface of the membrane along the electron holes from the side containing the high oxygen chemical potential side to the low oxygen chemical potential side, as shown in *Figure 1-11*. Meanwhile, the overall charge neutrality is maintained by a counterbalancing flux of electrons [88].

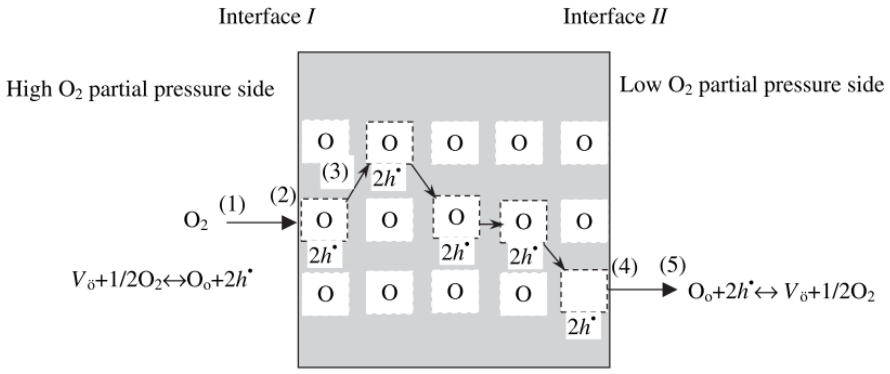

Figure 1-11: Oxygen permeation process from high oxygen chemical potential side to the low oxygen chemical potential side [88]

One of these two mechanisms follows the oxygen permeation process in this research. One of the mechanisms suggests that the oxygen molecule -that comes up from the lattice oxygen- reacts with methane on the catalyst and forms ethylene and water. The other mechanism suggests that the oxygen diffuses into the catalyst becoming an oxygen lattice; methane then reacts with the catalyst forming the same products as the first mechanism. The difference between the ionic conductivity of the catalyst and the membrane used should indicate which mechanism applies, and this will be investigated more in *Chapter 2*.

1.10 Membrane Reactors

1.10.1 Principle of Membrane Reactors

In order to achieve higher dissociation ratios, it is desirable to separate the products and shift the thermodynamic equilibrium of these splitting reactions. Several methods were proposed to shift the equilibrium, such as quenching [89] and heat-exchanger-loop [90]. However, the perm-selective permeable membrane reactor has attracted the most attention due to its advantages in separating products and continuous fuel production from splitting.

Integrating a membrane within a reactor allows the membrane to have a variety of uses, including serving as a product separator, catalyst support, or reactant distributor. The membrane is usually used to restrict the transport of certain species as it acts as a permeable or semi-permeable medium. This membrane function allows for the transportation of one particular component more readily; this

permeation process occurs due to the differences in physical and chemical properties between the membrane and the permeating components [69].

The capital and operational costs can be reduced significantly because the reaction and separation processes happen simultaneously within a membrane reactor. Combining chemical reactions with the membrane in a single-step process has several positive impacts, shifting the equilibrium reaction to the product side, controlling the addition of a reactant by supplying only a particular reactant to the reaction zone, gives an optimum concentration ratio of the two reactant streams and controlling the way for gases to contact catalysts.

All the above will significantly improve the conversion and yield rates beyond equilibrium values and obtain a conversion at less grave conditions, which will minimize the catalytic deactivation from coke deposition and provide an improved catalyst life in the long run [69].

1.10.2 Classification of Membrane Reactors

Several types of membrane reactors are mainly listed in *Table 1-3*. The most commonly referred to the reactor is the packed bed membrane reactor (PBMR), in which the reaction function is provided by a packed bed of catalysts in contact with the membrane. This type of membrane reactor configuration is ideal for highly selective membranes and situations where two reactions occur on either side of the membrane – the product of the reaction on one side acting as a reactant on the other side. In contrast, the exothermicity of the other compensates for the endothermicity of one reaction [69].

Table 1-3: Types of membrane reactors [69]

Membrane reactor type	Description	Acronym
Packed-bed membrane reactor	Additional catalysts are packed in the membrane reactor	PBMR
Fluidized-bed membrane reactor	Catalysts in the reactor are present in a fluidized mode	FBMR
Inert membrane reactor	Membrane does not participate directly in the reaction	IMR
Catalytic membrane reactor	Membrane functions as both catalyst and separator	CMR
Catalytic non-selective membrane reactor	Membrane is not selective but serves as a catalytic site for reactions	CNMR
Flow-through catalytic membrane reactor	Catalytic reactions take place while the reactants flow through the membrane	FTCMR
Membrane microreactor	Membrane is integrated with the microreactor having a characteristic length of <1 mm	MMR
Electrolyte membrane reactor	An external electrical circuit is applied to complete reactions	EMR

1.10.3 Configuration of Membrane Reactors

Unlike conventional reactors, membrane reactors usually have two separate compartments separated by a membrane. They are designed and fabricated based on the membrane configuration and the application conditions. There are three main MRs configurations [69]:

- **Tubular MRs** consist of feed streams on opposite sides of the membrane concurrently or counter. Sweep gas is employed on the permeate side to reduce the build-up of products and therefore reduce the potential rise in mass transfer resistance on the permeate side of the membrane.
- **Disk/flat sheet MRs** are easily fabricated with a relatively small amount of membrane material in the laboratory. Catalyst is usually packed on the membrane or coated on the membrane surface**.**
- **Hollow fiber MRs**: following the same procedures as tubular MRs, hollow fiber membranes can be assembled into reactors. They can offer a much greater packing density but suffer from poor mechanical strength

1.11 Chapter summary

This chapter illustrated the current production methods of ethylene and hydrogen. Various limitations hinder the current industrial production of higher hydrocarbons through the conversion of natural gas (methane is the principal component) and the efficient generation of hydrogen as an energy carrier. Direct and indirect methane conversion methods were illustrated, and the focus was then shifted toward investigating the OCM process and its limitations. An oxygen permeable membrane-supported water splitting is a potential technology that utilizes thermochemical energy to split water. Membrane-supported water-splitting technology can be integrated with the OCM process to co-produce high purity hydrogen and ethylene in a membrane reactor.

The membranes are classified based on their materials, morphology and structure, preparation methods, separation principles, or application areas. This research focuses on a mixed ionic perovskite membrane for its transport properties, chemical and thermal stability, and oxygen permeation. The oxygen permeability in a composite mixed ionic-electronic conductive membrane is illustrated in this chapter. Lastly, the principle of the membrane reactor is presented in this chapter. Integrating a membrane within a reactor allows the membrane to have a variety of uses, including serving as a product separator, catalyst support, or reactant distributor.

This thesis consists of a total of 5 chapters. The incorporation of a catalyst in a membrane reactor is discussed in *Chapter 2*. A catalyst is applied in the membrane reactor to control significant reactions

and obtain intermediate products, such as C_{2+} hydrocarbons. A one-dimensional model of the catalytic oxygen-permeable membrane reactor is developed in *Chapter 3*. A base case with a particular operating condition is discussed in *Chapter 4. I*n addition, sensitivity analysis and a parametric study are performed to identify the critical parameters that affect the co-production performances in a membrane reactor. Finally, *Chapter 5* illustrates the research conclusions and recommendations for future work.

Chapter 2

Catalyst microkinetics of OCM reactions

2.1 Chapter introduction

Combining water splitting and OCM in an oxygen-permeable membrane reactor is a promising technology that can use water splitting to co-produce a higher value product. *Chapter 1* established the fundamentals of the OCM process and presented the necessary background information about the new membrane reactor technology proposed in this research.

One way to improve the surface kinetics and enhance the overall performance of the membrane reactor is by implementing an appropriate OCM catalyst. This chapter investigates the importance of catalyst implementation in OCM reactions. This chapter also investigates the nature of active sites where highly reactive intermediates (i.e., chemisorbed species) are stabilized long enough to react. This stabilization of a reactive intermediate is critical in catalytic reactions. For clarity, the actives sites are divided into active catalytic and membrane-active sites, investigated in this chapter.

MATLAB is used to model a 10-step kinetic model of the OCM to C_{2+} hydrocarbons over a La_2O_3/CaO catalyst developed based on kinetic measurements in a micro catalytic fixed-bed reactor. The kinetics catalyst model is based on the model developed by Stanch et al. [91], which is considered one of the most accurate experimental and statistical analysis models. The model developed in this chapter predicts the catalyst kinetics for the one-dimensional oxygen-permeable membrane reactor model developed and analyzed later in chapters *Chapters 3* and *4.*

2.2 Importance of catalyst implementation in OCM reactions

Implementing active and selective catalysts offers a greater reaction control and intermediate products, such as C_{2+} hydrocarbons. For inorganic membranes, the oxygen flux can be significantly improved by either decreasing the membrane thickness or improving the surface exchange kinetics. Improving the surface kinetics is by implementing an appropriate OCM catalyst with adequate intrinsic catalytic properties [69]. In a gas phase catalytic reaction, adsorption of the reactants on the catalyst's surface is essential. The adsorption process can be divided into two types:

(1) Physical adoption

(2) Chemisorption

The chemisorption details how the reactants' chemical structure becomes more reactive by interacting with the catalyst that causes their bonds to be stretched, making them easier to break; this directly affects the rate of the chemical reaction.

The ideal catalyst for the OCM reactions is the one that eases the breaking of a C-H bond in a methane molecule (CH_4) and the dimerization of methyl radicals (CH_3). These two reactions are susceptible to the coupling reaction toward higher hydrocarbons such as ethane and ethylene while minimizing the carbon monoxide bond (C-O) formation at high conversion levels. However, if the oxygen permeation rate is greater than the rate consumed in the methane coupling, deep oxidation of methyl radical and C_{2+} products to CO_x will occur, and the C_{2+} yield will be reduced [69].

According to Lomonosov et al. [92], the Mars–Van Krevelen mechanism is the most accepted hypothesis as it details how the CH_4 reacts with the adsorbed O_2 that is located at the active site of the catalyst (as explained in a previous section) in order to form a methyl radical. In addition, the most favorable OCM catalyst favors the equilibrium that allows for rapid transformation of oxygen species responsible for the deep oxidation (O_2^-) to catalytically more desirable surface species (O^{2-}). Zavyalova et al. [64] provided several other properties that suitable OCM catalysts should have. These properties include intrinsic basicity, oxygen-anion conductivity, ability to form oxygen vacancies, fast exchange rates between atomic oxygen species on the surface, bulk oxygen-anion vacancies, and low sticking coefficients of methyl radicals (CH_3) on the catalyst surface.

2.2.1 Incorporation of catalyst in membrane reactors

According to Tan et al.[69] there are four ways to incorporate catalysts in the membranes of MRs:

(1) **Catalyst physically separated from an inert membrane**: the catalyst pellets are usually packed or fluidized on the inert membrane, which acts as an extractor for fractionation of products and as a distributor for controlled addition of reactants

(2) **Catalyst coated on the membrane surface**: the catalyst is coated on the membrane surface using a catalyst paste. The catalyst layer is generally porous and is integrated with the membrane into a single body

(3) **Catalyst dispersed in the porous membrane structure**: the catalyst is dispersed in the porous substrate of the membrane to form a membrane catalyst

(4) **Inherently catalytic membranes**: the membrane material is inherently catalytic, and the membrane serves as both catalyst and separator

Both methods 1 and 2 can be applied for the membrane reactor design discussed in this research. The choice is based on the membrane channel height dimensions and whether the catalyst layer is relatively thin compared to the channel height. If that is the case, coating a catalyst on the membrane surface is suitable. The packing catalyst pellets method can also be used, but a small amount of catalyst mass must be used.

2.3 OCM catalysts

2.3.1 Lanthanum-oxide catalyst (La_2O_3)

Various studies examined the OCM reactions over lanthanum oxide catalyst (La_2O_3). Simon et al. [60] simulated the OCM reaction over lanthanum oxide (La_2O_3) in a catalytic jet-stirred reactor while varying the operating conditions. The study presents a mechanism (shown in *Figure 2-1*) that entails the initiation of the reaction, production of CO_2, and the decomposition of C_2H_6 mechanisms for the OCM reactions. The study also points out two OCM pathways common in various catalysts, not just the La_2O_3. The first pathway leads to oxygenated species, and the second pathway leads to hydrocarbons.

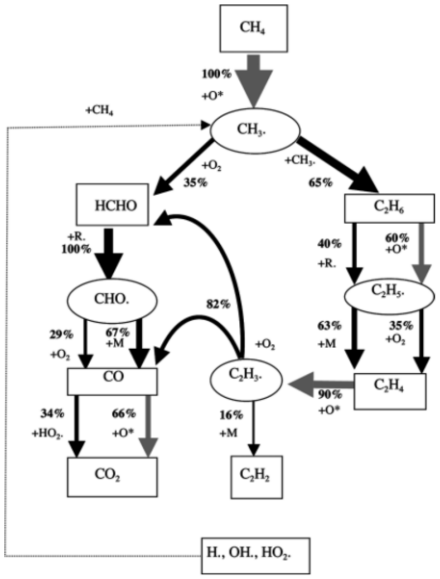

Figure 2-1: Mechanism of OCM over La_2O_3 catalyst (1023 K, 10 % CH_4 methane conversion) – dark arrows (homogeneous reactions) and light arrows (surface reactions) [60]

According to the mechanism presented by Simon et al. [60] (shown in *Figure 2-1*), the presence of La_2O_3 catalyst increases the C_{2+} selectivity when the gas space-time is low by introducing new surface initiation processes. Then, for higher gas space-time, the secondary reaction (shown in *Eqn.* (2-1)) is responsible for decreasing C_{2+} selectivity.

$$C_2H_3\bullet + O_2 \rightarrow CHO\bullet + HCHO \tag{2-1}$$

Furthermore, La_2O_3 catalysts showed several industrial limitations. Alexiadis et al. [93] reported that despite showing reasonable but not industrially feasible, C_{2+} yields values in these studies, the poor selectivity remains one of the significant hinders for the La-based catalyst to be fully commercialized for the OCM reaction-based applications. Also, Van et al. [94], in their study on the temperature and conversion dependence of selectivities in the oxidative coupling of methane on La_2O_3 catalysts, emphasize the limitation of La-based catalysts by concluding that for all the La_2O_3 catalysts investigated, the C_{2+} selectivity decreases linearly with methane conversion at temperatures above 900 °C. In addition, the studies from 1994 [95,96] examined the La_2O_3 under a wide range of temperatures (1023-1173 K) and various catalyst qualities. The study reported that C_{2+} selectivity drastically decreases with the increase in the conversion of methane.

On the other hand, Weiss et al. [97] showed results when analyzing the effect of maintaining low-temperature conditions (at around 100 K) lower than the temperature used for industrial La_2O_3 catalysts for catalyst reactions. The study suggests that using La_2O_3 with a larger specific area (12 m^2/g) showed more enhanced performance at low temperatures due to the noticeable increase in the defects on the catalytic surface, which plays an essential role in adsorption and activation of the O_2.

Based on the above, maintaining a low reactor temperature and low gas space-time for the La_2O_3 catalysts is the best approach to get the most suitable C_{2+} selectivity.

2.3.2 Lanthanum-calcium-oxide catalyst (La_2O_3/CaO)

Lanthanum-calcium oxide catalyst kinetics has proven the most reliable and comprehensive for OCM applications [66,98], which is why it has been chosen to simulate the OCM reactor for this research. La_2O_3/CaO can be prepared using wet impregnation of $CaCO_3$ with an aqueous solution of La

$(NO_3)_3 \bullet 6H_2O$. Wenzhao et al. [99] developed a study about the inhibition of gas-phase oxidation of ethylene in the oxidative conversion of methane La_2O_3/CaO. According to the study, lanthanum would act as an inhibitor of methyl radical or methane oxidation calcium oxide as a promoter for ethane dehydrogenation into ethylene and hydrogen, thus favoring oxidative dehydrogenation. A study by Mleczko et al. [63] examined the oxidative coupling of methane over a La_2O_3/CaO catalyst was in a laboratory-scale fluidized-bed reaction while supplying undiluted feed (p_{CH_4} > 60 kPa). The study pointed out how very reactive La_2O_3/CaO tended to be in an OCM reaction and reported a maximum selectivity of 73.8 % and a maximum yield of 16 %; this is considered one of the highest published values fluidized-bed reactors. However, the maximum yield tends to be lower at around 15.8 % for the fixed-bed reactor. Godini et al. [66] developed a comparative analysis of three different reactor structures, including a fixed-bed reactor and two different feeding structures of packed bed membrane reactors. Three types of kinetic models have been used: La_2O_3/CaO, Mn/Na_2WO_4 /SiO_2, and PbO/Al_2O_3. The study's quantitative results reported that La_2O_3/CaO has higher activity than other catalysts. This property enables oxygen to react rapidly and to remain at a low level in the reaction side. Consequently, it makes reaction more selective towards coupling products.

On the other hand, there are some limitations to using the OCM process over lanthanum-calcium oxide. For instance, Ching et al. [100] examined the OCM process using La_2O_3/CaO catalyst by running simulations of the OCM process in a fixed bed reactor for isothermal, adiabatic, and non-adiabatic operations. The reactor chosen for the study was a conventional tubular reactor packed with La_2O_3/CaO catalyst. The reactor operated at 110 kPa total pressure. The study pointed out that using La_2O_3/CaO as a catalyst for OCM reaction results in a yield drop with the increase in the concentration of methane in the feed. It is harder to find the optimum feed composition when using La_2O_3/CaO as a catalyst for OCM reaction.

Lastly, it is essential to analyze the material's ability to conduct oxygen anions through their structure as it facilitates the bulk transport of ions through the structure. One way to measure such an ability is by using ionic conductivity. According to Etsell et al. [101], they were reported in their study about the electrical properties of lanthanum oxide-calcium oxide solid electrolytes that the ionic conductivity of La_2O_3/CaO is about 2.4E-2 Ω^{-1} cm^{-1} at 1273.2 K and 15 % CaO composition. La_2O_3/CaO also exhibits an n-type and p-type conductivity mixture at different catalyst compositions, temperatures, and oxygen pressures. Etsell et al. [101] reported the conditions that favor the ionic conductivity over the other

types of conductivities in the La_2O_3/CaO catalyst, including low temperatures, intermediate oxygen pressures, and CaO ratio of the La_2O_3/CaO catalyst.

2.4 Heterogeneous surface reactions

A description of the heterogeneous chemistry is needed to characterize a perovskite membrane's catalytic activity and examine its coupling with oxygen permeation, gas-phase transport, and elementary reactions. In a heterogeneous catalytic reaction, several steps occur respectively:

(1) **Mass transfer (diffusion) of the reactant(s)** from the bulk fluid to the external surface of the catalyst pellet through the boundary layer of thickness

(2) **Diffusion of the reactant** through the catalyst pores to the immediate vicinity of the internal catalytic surface

(3) **Adsorption of reactant(s)** onto the catalyst surface

(4) **Catalyst surface reaction:** That is where the role of active sites is essential, where the catalytic reaction occurs. Several mechanics are used to describing the catalytic reactions [102] :

a. **Single site:** only the site on which the reactant is adsorbed is involved in the reaction.

b. **Dual site:** The adsorbed reactant interacts with another site (either unoccupied or occupied) to form the product.

c. **Eley–Rideal:** an adsorbed molecule and a molecule in the gas phase, such as the reaction of propylene and benzene

d. **Langmuir–Hinshelwood mechanism**: between two molecules over the surface of a heterogeneous catalyst suggests that both molecules have to be adsorbed on the neighboring sites to react and produce a particular product.

(5) **Desorption of the products** from the surface

(6) **Diffusion of the products** from the interior of the pellet to the external surface

(7) **Mass transfer of the products** from the external surface to the bulk fluid

It is essential to point out that when heterogeneous reactions are carried out at a steady state, the rates of each of the three reaction steps in series (adsorption, surface reaction, and desorption) are equal.

2.4.1 Nature of active sites

Defining the role of active sites has changed along the way since its first established back in 1928 by Hugh Stott Taylor [103], who suggested that the catalytic reaction does not occur over the entire solid surface but only at specific active sites or centers. Fogler [102] defined the active sites in his book as sites where highly reactive intermediates (i.e., chemisorbed species) are stabilized long enough to react. This stabilization of a reactive intermediate is critical in designing any catalyst.

2.4.2 Catalytic active sites

La_2O_3-based catalysts have high activity compared to other OCM catalysts [104], and that is why several experimental investigations have centered around its OCM chemistry. For homolytic C–H bond cleavage (breaking), surface oxygen species possessing oxidizing properties and a high hydrogen atom affinity is necessary for methane activation [92].

Palmer et al. [105] analyzed the possibility of surface peroxides as active sites being involved in hydrogen atom abstraction from methane in the presence of La_2O_3. The proposed model for OCM over La_2O_3-based catalysts suggested that the surface peroxides as the active oxygen source. The mechanism is laid down as follows:

(1) The cycle is initiated by dissociative adsorption of molecular oxygen over an oxide-covered surface to form a pair of surface peroxide sites.

(2) H-abstraction from CH_4 at the surface O_2^{2-} sites.

(3) Abstraction from CH_4 generates a gas-phase $\bullet CH_3$ radical (as shown in *Eqn.* (2-2)).

$$O_{2(s)}^{2-} + CH_4 \rightarrow O_{2(s)}^{2-} - H + \bullet CH_3 \qquad (2\text{-}2)$$

Where,

- $O_{2(s)}^{2-}$: peroxide site
- $\bullet CH_3$: methyl radicals

Coupling of gas-phase $\bullet CH_3$ radicals to produce ethane. CH_3 radicals are required for dimerization (dimerization is an addition reaction in which two molecules of the same compound react with each

other to give the adduct) to ethane, as shown in *Eqn.* (2-3). The methyl radical generated via the mechanism above combines ethane instead of reacting with surface oxygen-producing methoxy species. The ethane undergoes dehydrogenation, producing ethylene, as shown in *Eqn.* (2-4) and *Eqn.* (2-5).

$$\bullet CH_3 + \bullet CH_3 \rightarrow C_2H_6 \quad (2\text{-}3)$$

$$\bullet CH_3 + C_2H_6 \rightarrow CH_4 + \bullet C_2H_5 \quad (2\text{-}4)$$

$$\bullet C_2H_5 + \bullet CH_3 \rightarrow C_2H_4 + CH_4 \quad (2\text{-}5)$$

Where,

- $\bullet C_2H_5$: ethyl radicals

Several other mechanisms are used to explain the surface reaction mechanisms. Langmuir–Hinshelwood mechanism [106], which explains the reaction between two molecules over the surface of a heterogeneous catalyst, suggests that both molecules have to be adsorbed on the neighboring sites to react and produce a specific product through a biomolecular reaction. Eley–Rideal mechanism [107], on the other hand, suggests that only one of the molecules can be adsorbed while the other can directly react in its gas phase without adsorbing. However, according to Stanch et al. [91], the Eley-Rideal reaction mechanism cannot be used to consider the interaction of methane and oxygen molecules and adsorption of methane and oxygen on different active sites for the La_2O_3/CaO catalyst. The reason is that the Eley-Rideal reaction mechanism could not describe the linear dependency of the hydrocarbons formation on the methane partial pressure established in Stanch et al.'s [91] kinetic model of the OCM over the La_2O_3/CaO catalyst. However, the Eley-Rideal mechanism was proposed for $(CaO)_x$ and $(CeO_2)_{1-x}$ catalysts.

Mars-Van Krevelen Mechanism is based on the idea that adsorption of one molecule occurs on top of another molecule that had previously been adsorbed [107]. The mechanism also suggests that the solid catalyst undergoes an oxidation-reduction cycle, in which electrons are removed and returned to the solid catalyst between two sites in a catalytic process which means the solid catalyst undergoes an oxidation-reduction cycle.

In summary, various groups suggest different mechanisms for OCM catalyst surface reactions. Most of the OCM catalysts are similar in that they contain surface oxygen species with a high hydrogen atom affinity and can activate hydrocarbon molecules. These species can exist on the surface of OCM catalysts even when the gas phase contains no oxygen [92].

2.4.3 Membrane active sites

In this research, the feed side of the membrane reactor contains the water-splitting reaction. The water is the only source of oxygen and is injected into the reactor by an inert gas carrier. Therefore, the oxygen incorporation/dissociation reaction or the forward/reverse water thermolysis reaction occurs. Assuming one-step heterogeneous reaction between the gas phase and the solid membrane surface.

$$H_2O + V_O^{\bullet\bullet} \xleftrightarrow{k_{r,H}/k_{f,H}} O_O^x + 2h^{\bullet} + H_2 \tag{2-6}$$

This step can be expanded into,

$$H_2O_{(g)} \rightarrow \frac{1}{2}O_{2(g)} + H_{2(g)} \tag{2-7}$$

$$\frac{1}{2}O_{2(g)} + V_O^{\bullet\bullet} \Leftrightarrow O_{O(s)}^x + 2h^{\bullet} \tag{2-8}$$

Where,

- O^x_O: lattice oxygen
- V_O••: oxygen vacancy
- h•: positive electron-hole
- $k_{r,H}$ and $k_{f,H}$: forward and reverse reaction rate constants for water-splitting process

Eqn. (2-7) describes the gaseous water splitting process. In contrast, *Eqn.* (2-8) describes the overall oxygen incorporation/discharge process, a reversible reaction on the feed and sweep sides membrane surfaces. However, according to Ghoniem et al. [108], when fuel conversion occurs on the membrane surface, this overall reaction may not accurately capture the surface reactions because the fuel

conversion reactions might influence some of the intermediate oxygen surface exchange processes. That is why Ghoniem et al. [108] suggested two surface reactions :

$$O_2 + 2(s) \xleftrightarrow{k_{f,1}/k_{b,1}} 2O^-(s) + 2h^\bullet \tag{2-9}$$

$$O^-(s) + V_O^{\bullet\bullet} \xleftrightarrow{k_{f,1}/k_{b,1}} O_O^x + (s) + h^\bullet + H_2 \tag{2-10}$$

Where,

- (s): vacant surface site
- O^-: singly adsorbed charged surface oxygen anion

Eqn. (2-9) and *Eqn.* (2-10) can be used to describe the heterogenous reaction that occurs on the membrane surface as follows [108] :

(1) **Adsorption/desorption of gas-phase oxygen molecules** onto/ from the membrane surface.

(2) **Dissociation/association of adsorbed oxygen molecules** into/ from oxygen atoms.

(3) **Electron transfer with the lattice** to form singly charged surface oxygen anions/oxygen atoms.

(4) **Incorporation into/discharge from the crystalline structure** by filling/forming an oxygen vacancy.

(5) **Electron transfer with the lattice** to form fully charged/singly charged bulk oxygen anions.

Steps 1, 2, and 3 are associated with *Eqn.* (2-9), while steps 4 and 5 are associated with *Eqn.* (2-10). In addition, on the sweep side of the membrane reactor, there are active sites for the association of oxygen ions to form molecular oxygen, followed by desorption; this results in a slightly higher surface exchange rate. The catalyst will be directly applied to the membrane surface on the sweep side. The non-existence of oxygen molecules as a feed component will mean that the catalyst used has to have the capability of storing lattice oxygen in its crystal structure to generate higher hydrocarbons. The lattice oxygen diffuses out of the surface of the membrane. There are two paths for the diffusion of lattice oxygen out of the surface of the membrane on sweep side:

(1) Reacting with electron holes to produce oxygen molecules.

(2) Diffusion through the catalyst if the trigger has higher oxygen conductivity.

LCF membrane ionic conductivity (σ) gives 3E-2 S cm^{-1} and 7E-2 S cm^{-1} at 973K and 1073K compared to about 2.4E-2 Ω^{-1} cm^{-1} (2.4E-2 S cm^{-1}) at 1273.2 K and 15 % CaO composition of ionic conductivity for La_2O_3/CaO catalyst as mentioned in *Section 2.3.2* [109]. This information can be used to eliminate the second path of oxygen diffusion and supports the idea that the oxygen lattice can react with the electron-hole to leave the surface of the membrane and transform to gas-phase oxygen, as shown in *Eqn.* (2-11).

$$O_O^x + 2h^\bullet \xleftrightarrow{k_{r,O}/k_{f,O}} \frac{1}{2}O_2 + V_O^{\bullet\bullet} \tag{2-11}$$

Where,

- $k_{f,O}$ and $k_{r,O}$: forward and reverse reaction rate constants for oxygen incorporation reaction

2.5 La_2O_3/CaO OCM catalyst microkinetics model

Stansch et al. [91] provide a study that offers a 10-step kinetic model of the oxidative coupling of methane to C_{2+} hydrocarbons in a micro-catalytic fixed-bed reactor covering many reaction conditions. ($1 < P_{O2} < 20$ kPa, $10 < P_{CH4} < 95$ kPa, $700 < T < 955$ °C, $0.76 <$ space-time < 250 kg s/m^3). According to Daneshpayeh et al. [98], the probability of the model of Stansch et al. [91] being valid exceeds 99.99%, which is significantly higher than the probability for other models. Such a high probability proves that Stansch et al.'s [90] reaction network has a better validation than other models despite the greater number of reactions and parameters. In other words, this model has a more realistic description of OCM reaction behaviors. Therefore, this model was selected as a reaction network in this study.

Stansch et al. [91] provided a model that considered an almost complete set of elementary reactions consisting of nine heterogeneous and one homogeneous reaction step. According to this model, methane is converted into three parallel reactions:

(1) Formation of ethane by oxidative coupling of methane.

(2) Nonselective total oxidation of methane to carbon dioxide.

(3) Partial oxidation of methane to carbon monoxide. In which the carbon monoxide is then oxidized to carbon dioxide.

In consecutive steps, ethane conversion proceeds by two parallel routes, i.e., by heterogeneous catalytic oxidative dehydrogenation of ethane and thermal gas-phase dehydrogenation of ethane to ethylene. In addition, ethylene can be converted to carbon monoxide in two parallel ways, i.e., partial oxidation and steam reforming. Also, the carbon monoxide to carbon dioxide ratio is influenced by the water-gas-shift reaction, which proceeds in both directions. In this reaction network model, direct oxidation of ethane to carbon oxides was neglected, and reactions of ethane and ethylene to higher hydrocarbons (C_{3+}) with less than 5% selectivity were also neglected.

Step 1 : $CH_4 + 2O_2 \rightarrow CO_2 + 2H_2O$
Step 2 : $2CH_4 + 0.5O_2 \rightarrow C_2H_6 + H_2O$
Step 3 : $CH_4 + O_2 \rightarrow CO + H_2O + H_2$
Step 4 : $CO + 0.5O_2 \rightarrow CO_2$
Step 5: $C_2H_6 + 0.5O_2 \rightarrow C_2H_4 + H_2O$
Step 6 : $C_2H_4 + 2O_2 \rightarrow 2CO + 2H_2O$
Step 7 : $C_2H_6 \rightarrow C_2H_4 + H_2$
Step 8 : $C_2H_4 + 2H_2O \rightarrow 2CO + 4H_2$
Step 9 : $CO + H_2O \rightarrow CO_2 + H_2$
Step 10 : $CO_2 + H_2 \rightarrow CO + H_2O$

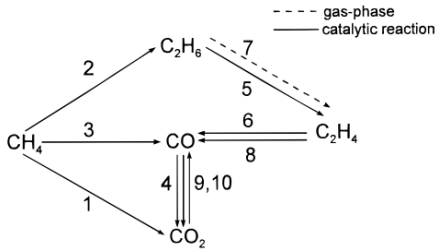

Figure 2-2: Set of stochiometric equations from Stansch et al. kinetic model [91]

The model used a combination of the Hugoen-Watson equation and power-law rate equations to describe the reaction rates equations. In order to describe the inhibiting effect of oxygen and carbon dioxide, a Hougen-Watson type rate equation was applied, as shown in *Eqn.* (2-13) and *Eqn. (2-12)*, respectively. For the oxidation reactions, an inhibiting effect of carbon oxide ($\Delta H_{ad,CO_2}$) had to be considered. In addition, the inhibiting effect of oxygen ($\Delta H_{ad,O_2}$), directly impacts the primary selective reaction step of ethane formation.

$$r_u = \frac{k_u \times e^{\frac{-E_u}{R \times T}} \times {p_C}^{m_u} \times {p_{O_2}}^{n_u}}{[1 + (K_{i,CO_2} \times e^{\frac{-\Delta H_{ad,u,CO_2}}{R \times T}} \times p_{CO_2})]^n} \quad , \ u = 1,3\text{-}6 \qquad (2\text{-}12)$$

$$r_2 = \frac{k_2 \times e^{\frac{-E_2}{R \times T}} \times (K_{O_2} \times e^{\frac{-\Delta H_{ad,O_2}}{R \times T}} \times p_{O_2})^{n_2} \times p_{CH_4}}{[1 + (K_{O_2} \times e^{\frac{-\Delta H_{ad,O_2}}{R \times T}} \times p_{O_2})^{n} + (K_{2,CO_2} \times e^{\frac{-\Delta H_{ad,CO_2}}{R \times T}} \times p_{CO_2})]^2} \quad (2\text{-}13)$$

In addition, in order to determine rates of thermal dehydrogenation, steam reforming of ethylene, and the water gas shift reaction, power-law rate equations were applied to quantify the rate equations for steps from 7 – 10, which is shown in the set of *Eqn.* (2-14).

$$\begin{aligned} \mathrm{r}_7 &= \mathrm{k}_7 \times e^{\frac{-E_7}{R \times T}} \times p_{C_2H_6} \\ \mathrm{r}_8 &= \mathrm{k}_8 \times e^{\frac{-E_8}{R \times T}} \times p_{C_2H_4}{}^{m_8} \times p_{H_2O}{}^{n_8} \\ r_9 &= \mathrm{k}_9 \times e^{\frac{-E_9}{R \times T}} \times p_{CO}{}^{m_9} \times p_{H_2O}{}^{n_9} \\ r_{10} &= \mathrm{k}_{10} \times e^{\frac{-E_{10}}{R \times T}} \times p_{CO_2}{}^{m_{10}} \times p_{H_2}{}^{n_{10}} \end{aligned} \quad (2\text{-}14)$$

Where,

- u: reaction step 1-10
- r_j: reaction rate (catalytic), [mol/g s]
- k_u: pre-exponential factor
- $E_{a,j}$: activation energy in the reaction step 'j', [J/mol]
- R: gas constant, [J/ mol K]
- T: temperature, [K]
- p: partial pressure, [Pa]
- m_u: reaction order
- n_u: reaction order
- n: estimated power exponent (0.40 at T > 1073.15 K, 0.65 at 1023.15 K and 1.00 at 973.15 K)
- K_{u,CO_2}: CO_2 adsorption constant, [Pa^{-1}]
- K_{2,O_2}: O_2 adsorption constant for reaction step 2, [Pa^{-1}]
- $\Delta H_{ad,CO_2}$: adsorption enthalpy for CO_2, [J/mol]
- $\Delta H_{ad,O_2}$: adsorption enthalpy for O_2, [J/mol]

2.5.1 La_2O_3/CaO catalyst microkinetics model computing process

In order to present the developed La_2O_3/CaO catalyst microkinetics model, a flow chart detailing the computing process is shown in *Figure 2-3*. The process starts by declaring the initial operating conditions, discussed further in *Section 2.5.2*. The estimation for the time step is discussed in *section 2.5.3*, followed by estimating the partial pressure inlet species. The process also includes the declaration of the kinetics parameters presented in *Section 2.5.4*. The model is based on a loop condition that details the step that corresponds to the point at which the total volume of the species reacted is equal to or higher than the total volume of the reactor, which indicates whether the input species have covered the entire volume of the reactor. The loop condition is explained further in *Section 2.5.5*.

A decision command is used to compute the loop condition, in which the maximum length developed reactor corresponds to the length at which the output molar flow rates are printed. The model will print out the molar flow rates at the corresponding step if the condition is satisfied. If the condition is not satisfied, the molar fractions, partial pressures, and reaction rates are computed at time step (j). The formation/destruction rates are then computed based on the reaction rates obtained. Lastly, the formation and destruction rates are used to obtain the new molar flow rates at the new time step (j+1), illustrated in *Section 2.5.7.*

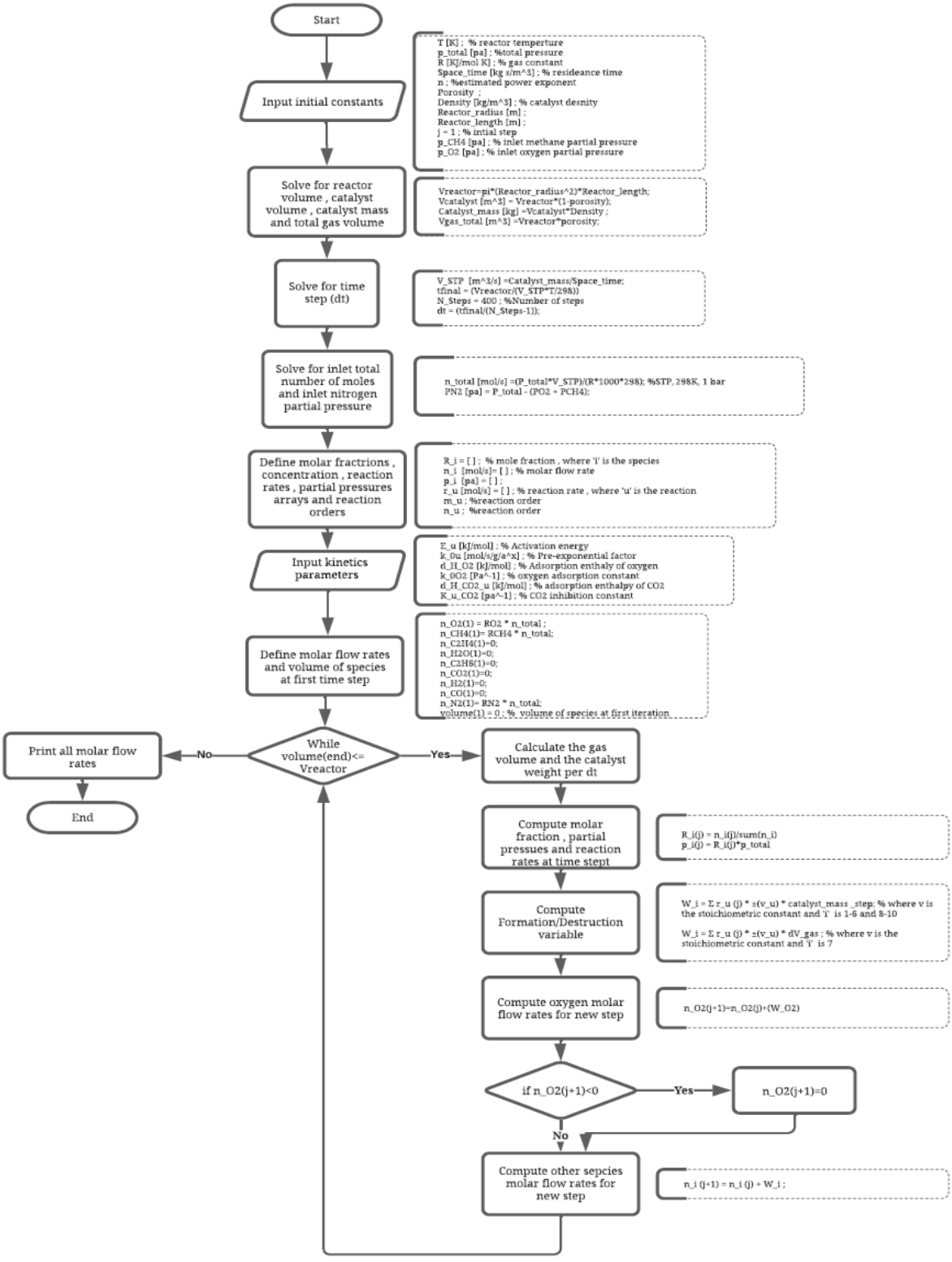

Figure 2-3: Flow chart showing computing process of La_2O_3/CaO catalyst microkinetics model

2.5.2 Reactor geometry and operating conditions

The MATLAB model developed depicts similar dimensions and operating conditions to the comprehensive 10-step kinetic model developed by Stansch et al. [91] to ensure that the catalyst model developed can accurately predict the La_2O_3/CaO catalyst kinetics. The model is based on a micro catalytic fixed-bed reactor covering various reaction conditions presented in *Table 2-1*.

Table 2-1: Dimensions and initial operating conditions (La_2O_3/CaO catalyst model)

Parameter	**Value**
Reactor radius ($r_{reactor}$) [m]	3E-3
Reactor length ($L_{reactor}$) [m]	2.27E-1
Reactor volume ($V_{reactor}$) [m^3]	6.42E-6
Gas constant (R) [kJ/mol K]	8.31E-3
Total pressure (p_{total}) [Pa]	100000
Temperature (T) [K]	$973.15 \leq T \leq 1103.30$
Space time [kg s/m^3]	1.86 - 49.97
Volumetric flow rate ($\dot{V}_{STP}$) [m^3/s]	4.9E-3
Total gas volume (V_{gas}) [m^3]	3.85E-6
Catalyst porosity (φ)	0.6
Catalyst volume ($V_{catalyst}$) [m^3]	2.58E-6
Catalyst mass ($m_{catalyst}$) [kg]	9.2E-3
Catalyst density ($\rho_{catalyst}$) [kg/m^3]	3600
Inlet methane partial pressure ($p_{CH_4,inlet}$) [pa]	$10 \leq P_{CH_4,inlet} \leq 80$
Inlet oxygen partial pressure ($p_{O_2,inlet}$) [pa]	$1.2 \leq P_{O_2,inlet} \leq 18.1$

For the reactor dimensions, the reactor developed has a cylindrical shape based on the reactor schematic presented in the kinetic model developed by Stansch et al. [91]. The reactor volume was calculated based on the cylindrical shape shown in *Eqn.* (2-15). The reactor radius and length shown in *Table 2-1* are also estimated based on the reactor schematic presented in a kinetic model developed by Stansch et al. [91].

$$V_{reactor} = \pi \times (r_{reactor})^2 \times (L_{reactor}) \tag{2-15}$$

Where,

- $V_{reactor:}$ volume of the reactor, [m^3]
- $_{reactor:}$ reactor radius, [m]
- $L_{reator:}$ reactor length, [m]

According to the kinetic model developed by Stansch et al. [90], methane, oxygen, and nitrogen are all inlet species for the operating condition. The inlet pressures of methane and oxygen are varied to examine a wide range of reactor conditions. The partial inlet pressure of nitrogen is calculated based on the assigned partial pressures of methane and oxygen, as shown in *Eqn.* (2-17). The partial pressures of the inlet species are used to calculate the initial molar ratios, as shown in *Eqn.* (2-16).

$$R_i = \frac{p_i}{p_{total}} \tag{2-16}$$

Where,

- R_i: Mole ratio for species ‘i'
- p_i: partial pressure for species ‘i', [pa]

$$p_{N_2} = p_{total} - (p_{O_2} + p_{CH_4}) \tag{2-17}$$

Where,

- p_{N_2}: nitrogen partial pressure, [pa]
- p_{O_2}: oxygen partial pressure, [pa]

- p_{CH_4}: methane partial pressure, [pa]
- p_{total}: total inlet pressure, [pa]

In order to find the total catalyst mass and volume, an estimation of the porosity is required. Due to the porous nature of the La_2O_3/CaO catalyst used. The catalyst bulk consists of a porous catalyst pellet made of small porous particles. The small porous particle is assumed to have a sphere-like core and a cubic outer shape, as shown in *Figure 2-4.*

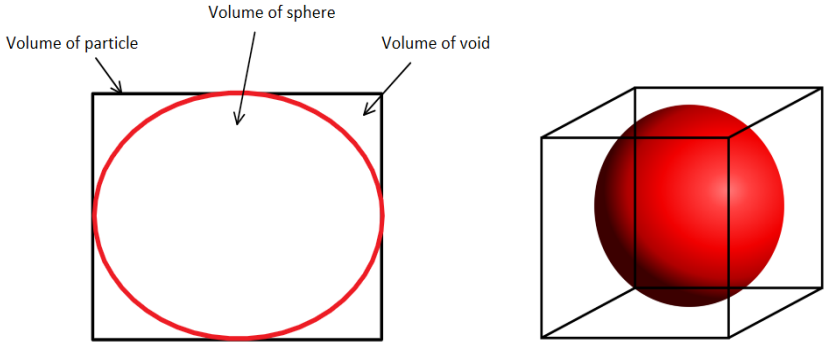

Figure 2-4: Schematic showing the catalyst's small porous particle

The radius of the catalyst's small porous particles can be estimated by equating its area and volume ratio and the catalyst BET surface area and its specific volume, as shown in *Eqn.* (2-18). The porosity is then estimated based on the ratio between the void volume between the core of the catalyst's particle and its outer shape and the total volume of the catalyst's small porous particles.

$$\frac{A_{catalyst,particle(sphere)}}{V_{catalyst,particle(sphere)}} = \frac{BET}{\upsilon} \tag{2-18}$$

$$\phi = \frac{V_{void}}{V_{total}} = \frac{V_{catalyst,particle} - V_{catalyst,particle(sphere)}}{V_{catalyst,particle}} \tag{2-19}$$

Where,

- $A_{catalyst,particle(sphere)}$: catalyst small porous particle area (sphere core), [m^2]
- $V_{catalyst,particle(sphere)}$: catalyst small porous particle volume (sphere core), [m^3]

- BET : catalyst's BET surface area, [m^2/kg]
- υ : specific volume (reciprocal of the density)
- ϕ : catalyst porosity
- V_{void} : volume of the void, [m^3]
- V_{total} : total volume, [m^3]

The total volume of the porous catalyst pellet (formed by compressing many small porous particles) is estimated using *Eqn.* (2-21) based on the catalyst porosity calculated by *Eqn.* (2-19). The catalyst porosity was estimated using *Eqn.* (2-19) can also be used to define the relationship between the volume of the gaseous mixture and the total volume of the reactor, seeing as the porosity is independent of the number of small porous particles that make up the porous catalyst pellet. Lastly, the total catalyst mass used in the reactor is calculated based on the total volume of the porous catalyst pellet and its density, as shown in *Eqn.* (2-22). The catalyst density is provided by Stansch et al. [91], shown in *Table 2-1*.

$$\phi = \frac{V_{void}}{V_{total}} = \frac{V_{gas}}{V_{reactor}} = \frac{V_{gas}}{(\frac{V_{catalyst}}{1-\phi})} \tag{2-20}$$

$$V_{catalyst} = V_{reactor} \times (1-\phi) \tag{2-21}$$

$$m_{catalyst} = V_{catalyst} \times \rho_{catalyst} \tag{2-22}$$

Where,

- $V_{catalyst}$: porous catalyst pellet volume, [m^3]
- $m_{catalyst}$: total catalyst mass, [kg]

2.5.3 Estimation of the time step (Δt)

The time step (Δt) is used to calculate the volume of the gas and the mass of the catalyst per iteration. The total time the species take to react inside the reactor fully has to be estimated. The estimated final time is found using *Eqn. (2-23).* As shown in the equation, to follow the assumed STP conditions, the reactor temperature is divided by 298 K (standard temperature).

The estimation of the time step might not be accurate; however, the accuracy of the time step does not impact the model output. As explained, the reactor model is assessed based on the reactor volume in which the total volume of the species reacted compared to the total volume of the reactor, which indicates whether the input species have covered the entire volume of the reactor. The manually assigned number of steps or iterations is 400 steps. The change in time parameter (Δt) is estimated using *Eqn.* (2-24).

$$t_{final} = \frac{V_{reactor}}{\frac{\dot{V}_{STP} \times T}{T_{STP}}} \tag{2-23}$$

$$\Delta t = \frac{t_{final}}{n_{steps} - 1} \tag{2-24}$$

Where,

- t_{final}: estimated final time, [s]
- T: reactor temperature, [K]
- T_{STP}: standard temperature (298 K), [K]
- n_{steps}: manually allocated number of iterations

2.5.4 Defining the activation energies, reaction orders, and enthalpy of adsorption

Table 2-2 presents all the kinetics parameters extracted from those listed in Stanch et al. [91] kinetics model. As mentioned, the kinetics developed by Stanch et al. [91] applies the Hougen-Watson type rate equation to describe the inhibiting effect of oxygen and carbon dioxide on the formation of ethane.

Table 2-2: Kinetics parameters from Stanch et al. [91]

Reaction	k_j [mol/g s $pa^{-(m+n)}$]	$E_{a,j}$ [kJ/mol]	K_{j,CO_2} [Pa^{-1}]	$\Delta H_{ad,CO_2}$ [kJ/mol]	K_{2,O_2} [Pa^{-1}]	$\Delta H_{ad,O_2}$ [kJ/mol]	m_j	n_j
1	0.2E-5	48	0.25E-12	-175	-	-	0.24	0.76
2	23.2	182	0.83E-13	-186	0.23E-11	-124	1	0.4
3	0.52E-6	68	0.36E-13	-187	-	-	0.57	0.85
4	0.11E-3	104	0.40E-12	-168	-	-	1	0.55
5	1.7E-1	157	0.45E-12	-166	-	-	0.95	0.37
6	6E-2	166	0.16E-12	-211	-	-	1	0.96
7	1.2E+7*	226	-	-	-	-	-	-
8	9.3E+3	300	-	-	-	-	0.97	0
9	0.19E-3	173	-	-	-	-	1	1
10	0.26E-1	220	-	-	-	-	1	1

*Reaction 7 units [mol/s m^3 Pa^1]

2.5.5 While loop condition

A 'while loop' is used to calculate the molar flow rates of species at each time step along with the reactor length. The loop condition (volume(end) < = Vreactor) is based on the total volume of the species reacted compared to the total volume of the reactor, which indicates whether the input species have covered the entire volume of the reactor. Once the total volume of the species exceeds the total volume of the reactor, this indicates that there is no further reaction because the catalyst is fully consumed.

2.5.6 Gas volume and catalyst per time step

In order to divide the reactor into a defined set of iterations, it is crucial to consider the amount of catalyst per iteration and the total volume of species per iteration. Firstly, the change in the gas volume at every iteration is calculated based on the ideal gas assumption (PV=nRT), as shown in *Eqn. (2-25)*. The change in total volume inside the reactor ($\Delta V = \Delta V_{gas} + \Delta V_{catatlyst.}$) is calculated using the porosity and calculated change in gas volume as shown in *Eqn. (2-26)*.

$$dV_{gas} = \frac{\sum \dot{n}_i \times R \times T}{p_{total}} \times (dt) \tag{2-25}$$

$$dV_{total} = \frac{dV_{gas}}{\phi} \tag{2-26}$$

The change in the catalyst volume is calculated in *Eqn.* (2-27) based on the relationship established in the porosity calculated shown in *Eqn.* (2-19). The change in the catalyst mass is calculated using the predefined catalyst density of 3600 kg/m^{3,} as shown in *Eqn.* (2-28).

$$dV_{catalyst} = dV_{total} \times (1 - \phi) \tag{2-27}$$

$$dm_{catalyst} = dV_{catalyst} \times \rho_{catalyst} \tag{2-28}$$

Where,

- $dV_{catalyst}$: change in catalyst volume, [m^3]
- dV_{gas}: change in gas volume, [m^3]
- dV_{total}: change in total volume (catalyst and gas), [m^3]
- $dm_{catalyst}$: change in catalyst mass per step, [m^3]

2.5.7 Molar flow rates for the new time step

As explained in *Section 2.5*, the model used a combination of the Hugoen-Watson equation and power-law rate equations to describe the reaction rates equations. The partial pressures of each species directly affect the reaction rates of the elementary steps, as shown in *Eqn.* (2-12), *Eqn.* (2-13), and *Eqn.* (2-14). The partial pressures are calculated based on the molar ratios of each species, as shown in *Eqn.* (2-30). The mole ratio of every species is calculated based on its corresponding molar flow rate and the summation of all the molar flow rates for the specific iteration, as shown in *Eqn.* (2-29).

$$R_i^{(j)} = \frac{\dot{n}_i^{(j)}}{\sum \dot{n}_i} \tag{2-29}$$

$$p_i^{(j)} = R_i^{(j)} \times p_{total} \tag{2-30}$$

The formation and destruction rate ($\dot{W}_i$) is calculated based on the reaction rates shown in *Eqn.* (2-12), *Eqn.* (2-13), and *Eqn.* (2-14), in addition to the species' stoichiometric coefficients. It is favorable for formation rates and negative for destruction rates. Lastly, all the species' output molar flow rates at the new step are calculated based on their corresponding formation and destruction rates and their corresponding molar flow rates at the previous step, as shown in *Eqn.* (2-32).

$$\dot{W}_i = \Sigma r_u \times \pm \nu_u \tag{2-31}$$

$$\dot{n}_i^{(j+1)} = \dot{n}_i^{(j)} + \dot{W}_i \tag{2-32}$$

Where,

- $\dot{W}_i$: formation/destruction rate of species 'i', [mol/s]
- $R_i^{(j)}$: mole ratio of species 'i' at iteration 'j.'
- $n_i^{(j)}$: molar flow rate of species 'i' at iteration 'j', [mol/s]
- $\Sigma \dot{n}_i$: summation of molar flow rates at iteration 'j.'
- $p_i^{(j)}$: partial pressure of species 'i' at iteration 'j,' [pa]
- r_u: rates for reaction 'u', [mol/s]
- v_u: stoichiometric coefficient
- $n_i^{(j+1)}$: molar flow rate of species 'i' at iteration 'j+1', [mol/s]

2.6 Chapter summary

Implementing active and selective catalysts offers a greater reaction control and intermediate products, such as C_{2+} hydrocarbons. Several researchers have investigated various OCM catalysts' kinetics, including lanthanum-calcium oxide catalyst (La_2O_3/CaO) kinetics, which has proven to be the most reliable and comprehensive for OCM applications [66,98]. It has been chosen to simulate the OCM reactor for this research.

Heterogeneous surface reactions are examined in this chapter to characterize the catalytic activity of a perovskite membrane and examine its coupling with oxygen permeation and gas-phase transport and reactions. The heterogeneous surface reactions include investigating the nature of catalytic and active membrane sites. The proposed model for OCM over La_2O_3-based catalysts suggested that the surface peroxides as the active oxygen source. The mechanism is laid down in *Section 2.4.2*. In addition, Ghoniem et al. [108] offered two surface reactions that describe the heterogeneous reaction on the membrane surface, shown in *Section 2.4.3*.

Lastly, a MATLAB model is developed in this chapter to predict the La_2O_3/CaO catalyst kinetics in a micro-catalytic fixed-bed reactor covering many reaction conditions. The model depicts similar dimensions and operating conditions to the comprehensive 10-step kinetic model developed by Stansch et al. [91] to ensure that the catalyst model developed can accurately predict the La_2O_3/CaO catalyst kinetics.

In *Chapter 3*, a one-dimensional oxygen-permeable membrane reactor model is developed. The membrane reactor model builds on the catalyst model developed in this chapter to combine the microkinetic of water splitting, catalytic OCM reactions on the membrane surface, and the charged species diffusion across the membrane.

Chapter 3

One-dimensional oxygen-permeable membrane reactor model

3.1 Chapter introduction

This chapter investigates the co-production of hydrogen and ethylene from water splitting and OCM, respectively. Unlike the chemical looping or redox cycles where the oxygen carriers move between the oxidizing and reducing environments at high temperatures [110,111], this membrane technology combines the oxidizing and reducing processes into one unit without mechanical movements of the reactor. More effortless operation, thus, can be achieved. Additionally, the oxygen permeable membrane can shift the thermodynamic equilibrium to split water further to produce hydrogen.

This chapter showcases the development of a one-dimensional model of an oxygen-permeable membrane reactor for the selectivity of higher hydrocarbons in OCM reactions by providing a more controlled oxygen inlet concentration (or partial pressure). The model is based on a plug-flow reactor that mimics a monolith membrane reactor design. The multi-channel monolithic form is developed to increase the mechanical robustness and the surface area-to-volume ratio and allow the introduction of the feed in the channels. At the same time, the permeate is obtained from the membrane wall.

The model combines the microkinetics of water splitting, catalytic OCM reactions on the membrane surface, and the charged species diffusion across the membrane, which includes the development of a resistant-network permeation model and estimation of the oxygen flux through the membrane. In addition, the La_2O_3/CaO catalyst microkinetics model developed in *Chapter 2* will be incorporated into this model to investigate the effect of fixing a catalyst on the membrane surface.

Ordinary differential equation solver from MATLAB is used to solve the governing differential equations that concern mass balance and pressure drop along the length of the reactor.

3.2 Implementation of OCM process in oxygen-permeable membrane reactors

In a membrane reactor, chemical reactions and membrane separations are combined in one unit. A lower fabrication cost can be achieved due to the integration of reaction and separation [69]. Porous or dense inorganic membrane reactors for OCM applications can allow for much higher C_{2+} hydrocarbon selectivity and yield [112]. In addition, dense mixed conducting ceramic membranes have excellent

permselectivity toward oxygen. Therefore, air/water can be used directly as a source of oxygen needed for the OCM process.

In this research, the implementation of dense ceramic membranes can have an effective oxygen distribution along the reactor into the catalyst bed. The local hydrocarbon to oxygen ratio in the reaction zone is high, leading to much higher selectivity. As a result, the product yield can be significantly increased since the total amount of oxygen participating in the reaction is not reduced. In addition, methane loss is prevented due to back-permeation, one of the dense membrane characteristics.

The modification of the high-oxygen-permeable ceramic membrane surfaces with a proper OCM catalyst can contribute to the overall yield of the membrane reactor [69]. It is also possible to increase the yield by matching the oxygen permeation rate of the membrane and surface catalytic activation of the methane on the membrane surface because the overall C_{2+} yield is determined by the combined effects of both crucial factors [69]. Enhancing the surface catalytic activation of the methane on the membrane surface may be performed by enhancing catalyst kinetics on the membrane surface. When the oxygen permeation rate is greater than the rate consumed in the methane coupling, deep oxidation of methyl radical and C_{2+} products to CO_x occurs, reducing the C_{2+} yield. Therefore, to reduce the gap between OCM achieved yield (25 % in conventional OCM reactors [88]) and the desirable industrial values (economically attractive C_{2+} yield threshold of 30 % [88]), improving the surface catalytic activation of methane and the oxygen permeation rate must happen concurrently.

3.3 The one-dimensional oxygen-permeable membrane reactor model

The model design is based on a multi-channel monolithic form divided into a feed channel that sweep channel. The two channels are considered two plug flow reactors that work simultaneously, and a membrane separates them and allows for the oxygen permeation process between the feed and sweep sides, as shown in *Figure 3-1*. On the feed channel, water (mole fraction = 0.8) is fed into the channel alongside nitrogen (mole fraction = 0.2) which acts as an inert carrier gas. As a result of the water-splitting process in the channel, three species are produced at the channel's outlet: unreacted water, hydrogen, and nitrogen.

The oxygen-permeable membrane used is an LCF-91 membrane which acts as a reactant provider as it allows the oxygen to permeate through it. As shown in *Figure 3-1,* the La_2O_3/CaO catalyst is deposited on the surface of the membrane.

The sweep side-channel allows for methane injection (mole fraction = 0.7) and nitrogen (mole fraction = 0.3) as an inert gas; this allows the OCM process to occur in which the membrane is providing oxygen. The sweep side outlet shows unreacted oxygen, methane, C_{2+} species (ethane and ethylene), water, CO_x (carbon monoxide and carbon dioxide), hydrogen, and nitrogen.

The membrane reactor model developed considers the membrane's surface reactions and the mass transfer between the gas bulk and the membrane surface. Several operating conditions assumptions were applied:

(1) Isothermal temperatures condition is considered, and the feed, sweep, and membrane temperatures are constant and consistent. According to Bhatia et al. [100], the isothermal operation was considered appropriate to study the influence of the changes in different operating variables without added temperature effect.

(2) Steady operation, so the reaction rates on the feed and sweep side are correlated with the oxygen flux across the membrane

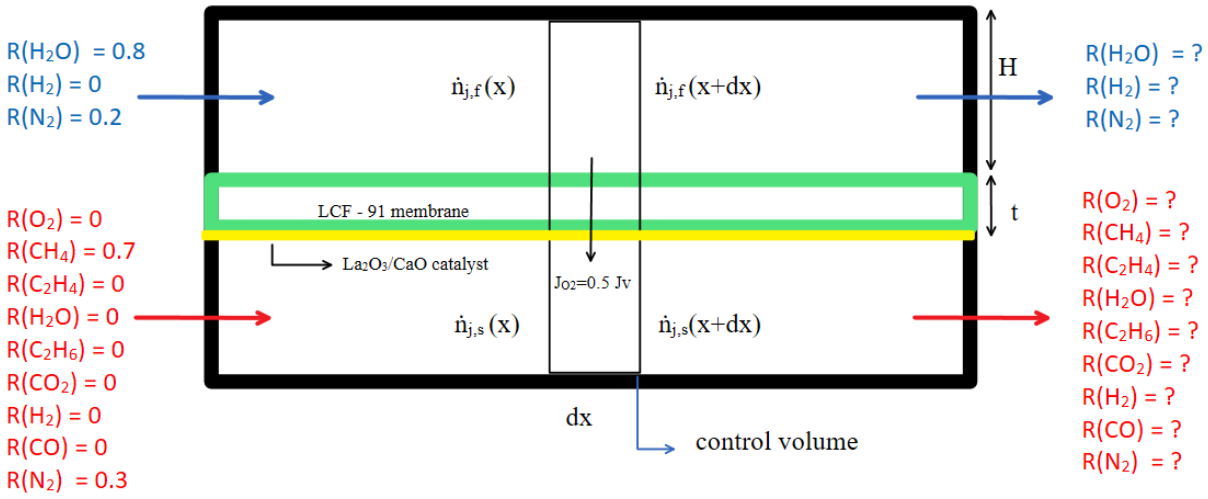

Figure 3-1: Plug flow membrane reactor model showing feed side, sweep side, and membrane

3.3.1 Mechanism of the co-production process of hydrogen and ethylene using membrane technology

Water is fed to the reactor on the feed side, and nitrogen is used as an inert carrier gas to carry the desired amount of water into the feed side chamber. Water molecules react with the oxygen vacancies on the oxygen permeable membrane to produce hydrogen and lattice oxygen, as shown in *Eqn. (2-6)*.

The oxygen atom from water incorporates the lattice oxygen and diffuses through the oxygen-permeable membrane due to the potential chemical gradient. A three-resistance model which details the permeation process of oxygen through the membrane is shown in *Section 3.3.3.1.3*. The three-resistance model is used to solve the vacancy flux (J_v), which relates to the formation/destruction rate of the species on the feed side. J_v is a function of the concentration of water and oxygen on the sweep side, seeing as the water-splitting rate must equal the rate of formation of the oxygen molecule on the sweep side. The oxygen flux (J_{O_2}) is half of the J_v, which can then be used to find the concentration of oxygen permeated from the feed side to the sweep side.

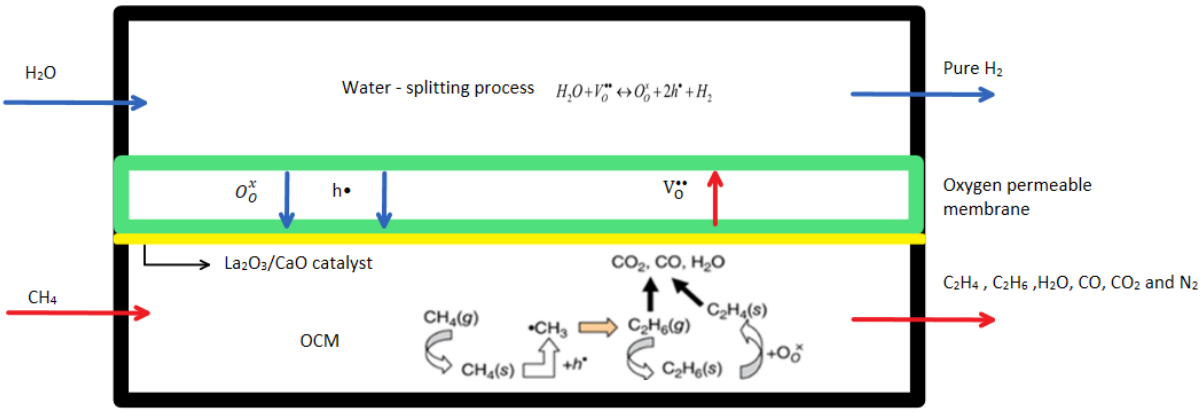

Figure 3-2: Co-production of C_2H_4 and H_2 using oxygen-permeable membrane

On the sweep side, the OCM catalytic reaction occurs in which CH_4 is fed into the sweep side compartment and nitrogen as an inert gas. Nitrogen carries the task of controlling the temperature in the reactor and overcoming the challenge of hot spot formation since OCM is a highly exothermic reaction [100]. Thermal NO_x can be formed by the oxidation of nitrogen in the air and requires sufficient temperature and time to produce NO_x. A rule of thumb is that below approximately 1700K, the formation of thermal NO_x is not significant enough [113]. The thermal NO_x formation can be

neglected since the membrane reactor temperature is maintained at around 1300 K. Incorporating the water-splitting process on the feed side channel will result in an overall endothermic process for the entire reactor.

The CH_4 reacts directly with the gaseous oxygen molecule to produce ethane, which then goes through the dehydrogenation process to produce ethylene as part of the OCM process on the sweep side *(Figure 2-2*). The oxygen molecule resulted in oxygen diffusion out of the membrane surface, as shown in *Eqn.* (2-11). La_2O_3/CaO catalyst is applied to the surface membrane, and the reaction rates of the primary OCM reactions (according to the kinetics provided by Stansch et al. [91]) are applied to find the rates of formation/destruction of both the inlet species and products including higher hydrocarbons and CO_2, CO, and hydrogen.

The products on different sides of the membrane (i.e., hydrogen and ethylene) can be collected for further applications. For example, ultrahigh-purity hydrogen can be separated from the steam-hydrogen mixture on the feed side using a pressure-dependent absorption-desorption process which can be used to split hydrogen from the hydrogen and nitrogen gas mixture [114]. The hydrogen can be used for fuel cell or semiconductor industries [115]. The ethylene from OCM on the sweep side can be separated from the gas mixture using cryogenic distillation [15] and used for various industrial applications, as explained in *Section 1.2.1*.

3.3.2 Membrane reactor geometry

As explained in *Section 3.3*, the membrane reactor is divided into two plug flow reactors, one of which acts as a feed side compartment, and the other reactor acts as a sweep side. These two reactors are divided by a membrane in which the permeation process of oxygen across the membrane occurs.

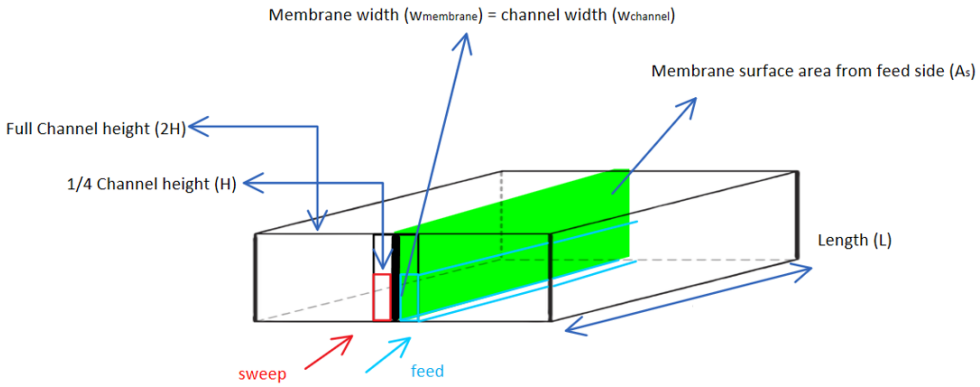

Figure 3-3: Feed and sweep channels and membrane dimensions

The channels dimensions of the membrane reactor are shown in *Figure 3-3*. As shown, the feed and sweep sides control volumes are assumed to be 1/4 of the entire reactor channel. This estimation is possible due to symmetry, which means the boundaries of the chosen control volumes can be assumed to have no interactions with the surrounding channels that share the same walls. This assumption will allow studying the heat and mass transfers between the membrane and the two feed and sweep sides.

Based on the schematic shown in *Figure 3-3*, the surface area of the membrane is calculated using *Eqn.* (3-1). While the cross-sectional area of the channels is calculated using *Eqn.* (3-2). Lastly, the total volume of the reactor is calculated based on the rectangular cross-sectional area of the channels. The total volume of the reactor is calculated using.

$$A_{s,membrane} = L_{membrane} \times w_{membrane} \tag{3-1}$$

$$A_{c,channel} = H_{channel} \times w_{channel} \tag{3-2}$$

$$V_{reactor} = L_{channel} \times H_{channel} \times w_{channel} \tag{3-3}$$

Where,

- $A_{s,membrane}$: surface area of the membrane, [m^2]
- $L_{membrane}$: membrane length (which is equal to the channel length), [m]
- $A_{c,channel}$: cross-sectional area of channels, [m^2]
- $V_{reactor}$: total volume of the reactor, [m^3]

3.3.3 Governing equations

3.3.3.1 Mass balance

Figure 3-4 shows the mass balance at each (Δx) (change in reactor length) along with the 1/4 of the entire reactor channel based on the symmetry configuration discussed in *Section 3.3.2*.

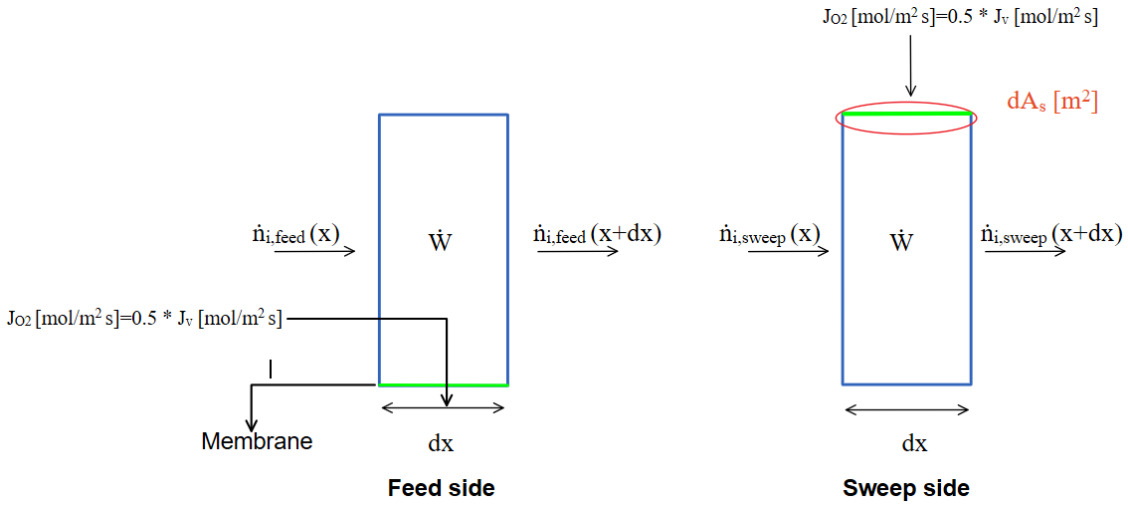

Figure 3-4: Control volumes for feed and sweep sides, showing mass balances at each (Δx) (change in reactor length

The mass balance governing equation is shown in *Eqn. (3-4)* based on *Figure 3-4* and the assumptions described in *Section 3.3*. As shown in the figure, the feed side and sweep side are related through the J_v and J_{O_2} , which will be explained in *Sections 3.3.3.1.3* and *3.3.3.1.4*.

$$\frac{d(\dot{n}_{i,s})}{dx}[mol/s\ \mathrm{m}] = \frac{\dot{W}_{i,s}(x)}{dx}[mol/s\ \mathrm{m}] \qquad (3\text{-}4)$$

Where,

- $d(\dot{n}_{i,s})$: change in molar flow rate of species ‘i’ and for channel ‘s’ [mol/s]
- dx : change in reactor length, [m]
- $\dot{W}_{i,s}$: formation/destruction rate of species ‘i’ and for channel ‘s’ in relation to reactor length, [mol/s]

3.3.3.1.1 Formation and destruction rates

On the feed side, the water-splitting process occurs in which water is fed to the reactor on the feed side, and nitrogen is used as the carrier gas to carry the desired amount of water into the feed side chamber. Water molecules react with the oxygen vacancies on the oxygen permeable membrane to produce hydrogen and lattice oxygen, as explained in *Section 3.3*. The microkinetic of water splitting and catalytic OCM reactions on the membrane surface on the sweep side are related through the charged species diffusion across the membrane. That is why the formation/destruction rate of species 'i' is proportional to the J_v [mol/m^2 s], as shown in *Eqn.* (3-5). The (+) sign corresponds to species formation, and the (-) sign corresponds to the consumption of species.

$$\dot{W}_{i,\,feed}[mol/s] = (\pm)J_v\ [\mathrm{mol/m^2\ s}] \times \mathrm{dA}_{s,membrane}[\mathrm{m^2}] \tag{3-5}$$

Where,

- $\dot{W}_{i,feed}$: formation/destruction rate of species 'i' and for feed channel, [mol/s]
- J_v : vacancy flux, [mol/m^2 s]
- $\mathrm{dA}_{s,membrane}$: change in membrane surface area, [m^2]

On the sweep side, OCM catalytic reaction occurs in which CH_4 is fed into the sweep side compartment and nitrogen as an inert gas. La_2O_3/CaO catalyst is applied to the surface membrane, and the primary OCM reactions' reaction rates are explained in *Section 3.3.* The kinetics of the OCM catalyst reaction is based on the La_2O_3/CaO OCM catalyst microkinetics model developed in *Chapter 2, section 2.5.* Therefore, the formation and destruction rate ($\dot{W}_i$) is calculated using *Eqn.*(2-31) which is based on the reaction rates shown in *Eqn.*(2-12), *Eqn.* (2-13), and *Eqn.* (2-14), in addition to the species' stoichiometric coefficients, positive for formation rates and negative for destruction rates.

3.3.3.1.2 Change in catalyst mass and gas volume per Δx

According to elementary reaction steps shown in *Figure 2-2*, given that the heterogeneous reactions on the sweep side take place on the catalyst's surface, reaction rates (1-6, 8-10) are multiplied by the change of catalyst mass per Δx. Meanwhile, the homogenous gaseous reaction rate (7) is multiplied by the change in gas volume per Δx. The change of total volume over (Δx) [m^3] is calculated using *Eqn.* (3-6).

$$dV_{total} = dx \times A_{c,channel} = dx \times H_{channel} \times w_{channel} \quad (3\text{-}6)$$

Where,

- dV_{total} : change in total reactor volume, [m^3]

The change of gas volume [m^3] is calculated using *Eqn.* (3-7).

$$dV_{gas} = \phi \times dV_{total} = \phi \times dx \times H_{channel} \times w_{channel} \quad (3\text{-}7)$$

Where,

- dV_{gas} : change in gas volume, [m^3]
- ϕ : porosity, [dimensionless]

Using the relation between the volume of gas and the catalyst volume, the change of catalyst volume [m^3] is calculated using *Eqn.* (3-8).

$$dV_{catalyst} = (1 - \phi) \times dV \quad (3\text{-}8)$$

Where,

- $dV_{catalyst}$: change in catalyst volume, [m^3]

The change of catalyst mass [kg] is calculated using *Eqn.* (3-9).

$$\begin{aligned} dm_{catalyst} &= dV_{catalyst} \times \rho \\ dm_{catalyst} &= (1 - \phi) \times (dx \times H_{channel} \times w_{channel}) \times (\rho) \end{aligned} \quad (3\text{-}9)$$

Where,

- $dm_{catalyst}$: change in catalyst mass, [kg]

3.3.3.1.3 Resistance network for oxygen permeation across the membrane

Wu et al. [74] developed the resistance-network kinetics model for oxygen permeation across the membrane (from high oxygen concentration to low oxygen concentration). The oxygen permeation process through an MIEC membrane can be divided into five steps, two mass transfer steps between

the gas phase and the surface, two surface reaction steps, and a bulk diffusion step through the membrane. The resistance network treats each step as a 'resistance' for oxygen permeation. A series of resistances are then identified to summarize the barriers to the oxygen permeation from the oxygen source on the feed side to the oxygen sink on the sweep side. The kinetics of the model will change according to oxygen sources. The feed side involves H_2O direct-incorporation mechanism. On the sweep side, oxygen formation involves Mars-van Krevelen (MvK) mechanism for fuel oxidation, as shown in *Table* 3-1. According to Wu et al. [74], several assumptions were taken in order to simplify the permeation model and solve for vacancy fluxes as follows :

Water feed side

$$J_v^{'} = k_{r,H} C_{H_2O}^{'} C_V^{'} \tag{3-10}$$

Where,

- $J_v^{'}$: the absolute value of oxygen vacancy flux at the feed side, [mol/m^2 s]
- $k_{r,H}$: the reverse reaction rate constant for the hydrogen oxidation reaction, [m^4/mol s]
- $C_{H_2O}^{'}$: the concentrations of water on the feed side, [mol]
- $C_V^{'}$: the oxygen vacancy concentration on the feed side, [mol]

Oxygen vacancy diffusion rate in the bulk

The Nernst-Planck equation models the charged species transfer as shown in *Eqn.* (3-11).

$$J_v = -D_V \frac{\partial C_V}{\partial y} = D_V \frac{C_V^{''} - C_V^{'}}{t} \tag{3-11}$$

Where,

- J_v: oxygen vacancy diffusion rate in bulk, [mol/m^2 s]
- D_V: diffusivity of oxygen vacancy, [m^2/s]
- $C_V^{''}$: the oxygen vacancy concentration on the sweep side, [mol]
- t: membrane thickness, [m]

Sweep side

$$J_v^{"} = \tilde{k}_{r,O}(C_O - C_V^{"}) - k_{f,O} C_{O_2}^{"\,0.5} C_V^{"} \tag{3-12}$$

Where,

- $\tilde{k}_{r,O}$ and $k_{f,O:}$ reaction rate constants for the oxygen incorporation/dissociation, [$m^{2.5}/mol^{0.5}$ s]
- C_O : concentration of oxygen sites in the lattice, [mol/cm^3]
- $C_{O_2}^{"}$: concentrations of oxygen on the sweep side, [mol]

By equating the oxygen vacancy flux on the feed side surface, *Eqn.* (3-10), through the bulk *Eqn.* (3-11) and on the sweep side surface *Eqn.* (3-12), the vacancy flux equation can be expressed in the potential difference over the sum of three resistances, as shown in *Eqn.* (3-13).

$$J_v = \frac{\Delta P}{R_f + R_b + R_s} \tag{3-13}$$

Where,

- Δ P: potential difference.
- R_f, R_b, and $R_{s:}$ the feed side surface reaction resistances, bulk diffusion, and sweep side surface reaction, respectively.

Table 3-1: Resistance network [74]

Oxygen source	Water
Sweep side mechanism	Inert sweep
Feed side reaction	$H_2O + V_O^{\bullet\bullet} \xleftrightarrow{k_{r,H}/k_{f,H}} O_O^x + 2h^{\bullet} + H_2$
Sweep side reaction	$O_O^x + 2h^{\bullet} \xleftrightarrow{k_{r,O}/k_{f,O}} \frac{1}{2}O_2 + V_O^{\bullet\bullet}$

Potential gradient (Δ P)	$\frac{\tilde{k}_{r,O}\, C_O}{\tilde{k}_{r,O} + k_{f,O} C_{O_2}^{''\,0.5}}$
Surface reaction resistance (feed side) (R_f)	$\frac{1}{k_{f,H_2O} C_{H_2O}^{'}}$
Bulk resistance [R_b]	$\frac{t}{D_v}$
Surface reaction resistance (sweep side) (R_s)	$\frac{1}{\tilde{k}_{r,O} + k_{f,O} C_{O_2}^{''\,0.5}}$

The vacancy flux is calculated using *Eqn. (3-14)* based on the above.

$$J_v\ [\mathrm{mol/m^2 s}] = \left[\frac{\frac{\tilde{k}_{r,O}\, C_O}{\tilde{k}_{r,O} + k_{f,O} C_{O_2}^{''\,0.5}}}{\frac{1}{k_{f,H_2O} C_{H_2O}^{'}} + \frac{t}{D_v} + \frac{1}{\tilde{k}_{r,O} + k_{f,O} C_{O_2}^{''\,0.5}}} \right] \tag{3-14}$$

Where,

- C_O: concentration of oxygen sites in the lattice, assumed to be a constant value (82500 mol/m^3, estimated from the XRD measurements of the stoichiometric LCF-91 lattice size in the air) [116].
- k_{r,H_2O}: water splitting reaction rate constant, [m^4/mol s]
- $\tilde{k}_{r,O}$ and $k_{f,O}$: reaction rate constants for the oxygen incorporation/dissociation, [m$^{2.5}$/mol$^{0.5}$ s]
- $C_{H_2O}^{'}$: surface concentration of water on the feed side, [mol]
- $C_{O_2}^{''}$: surface concentration of oxygen on the sweep side, [mol]
- $C_V^{'}$ and $C_V^{''}$: concentrations of oxygen vacancies on the feed and sweep side, respectively, [mol]

- t: membrane thickness, [m]
- D_v: vacancy diffusivity, [m^2/s]

As explained in *Section 3.3.1*, the vacancy flux is a function of water concentration on the feed side and oxygen on the sweep side. The water-splitting rate must equal the oxygen molecule formation rate on the sweep side. That is how the microkinetics of water splitting and catalytic OCM reactions on the membrane surface are combined through the charged species diffusion across the membrane.

The homogeneous reaction in the gas phase is neglected on the feed side due to the slow kinetics compared to the heterogeneous surface reaction. Therefore, the formation and destruction rates of species 'i' on the feed side are proportional to the vacancy flux, as shown in *Eqn. (3-15)*, *Eqn. (3-16)*, *Eqn. (3-17)*. The destruction rate of water is related to vacancy flux, as shown in *Eqn. (3-15)*. The negative sign is the water species being consumed on the feed side-channel.

$$\dot{W}_{H_2O,\,feed} = -J_v \times w_{membrane} \tag{3-15}$$

The formation rate of water is related to vacancy flux, as shown in *Eqn.* (3-16). The positive sign is the hydrogen produced on the feed side-channel. Hydrogen production is the primary purpose of water thermolysis.

$$\dot{W}_{H_2,\,feed} = J_v \times w_{membrane} \tag{3-16}$$

Nitrogen gas is inert and does not react with the other species, as shown in *Eqn.* (3-17).

$$\dot{W}_{N_2,\,feed} = 0 \tag{3-17}$$

Where,

- $\dot{W}_{H_2O}$: destruction rate of water on the feed side, [mol/s]
- $\dot{W}_{H_2}$: formation rate of water on the feed side, [mol/s]
- $\dot{W}_{N_2}$: formation rate of water on the feed side, [mol/s]

On the sweep side, the vacancy flux is related to the oxygen flux, which indicates the amount of diffused oxygen from the feed side to the sweep side and can be used to find the concentration of oxygen transported from the feed side to the sweep side. The oxygen flux is formulated in the next *Section 3.3.3.1.4.*

3.3.3.1.4 Oxygen flux

According to Sunarso et al. [73], as the oxygen diffuses across the perovskite membrane in the form of oxygen ions or oxygen vacancies, the oxygen flux is half of the vacancy flux, as shown in *Eqn.* (3-18).

$$J_{O_2}[\text{mol/m}^2\text{s}] = \frac{1}{2} J_v = \frac{1}{2} \times \left[\frac{\dfrac{\tilde{k}_{r,O} C_O}{\tilde{k}_{r,O} + k_{f,O} C_{O_2}^{''0.5}}}{\dfrac{1}{k_{f,H_2O} C_{H_2O}^{'}} + \dfrac{\mathrm{t}}{\mathrm{D}_v} + \dfrac{1}{\tilde{k}_{r,O} + k_{f,O} C_{O_2}^{''0.5}}} \right] \tag{3-18}$$

The syms function in MATLAB is used to create symbolic scalar variables. This function is used in the 1-D model to simultaneously solve *Eqn.* (3-10), *Eqn.* (3-11), and *Eqn.* (3-12) to estimate the flux and the oxygen fluxes at every iteration. Based on the function results, the oxygen mass balance on the sweep side is formulated as follows:

Based on the mass balance showcased in *Section 3.3.3.1* and *Figure 3-4*, the change in oxygen molar flow rate at every change in reactor length is estimated using *Eqn.* (3-19) and *Eqn.* (3-20).

$$\dot{n}_{O_2,sweep}(x + dx) - \dot{n}_{O_2,sweep}(x) = \dot{W}_{O_2,sweep} + (J_{O_2} \times dA_{s,membrane}) \tag{3-19}$$

$$\frac{d\,\dot{n}_{O_2,sweep}}{dx} = \frac{\dot{W}_{O_2,sweep}}{dx} + \frac{(J_{O_2} \times w_{membrane})}{dx} \tag{3-20}$$

Where,

- $d\dot{n}_{O_2,sweep}$: change of oxygen molar flow rate on the sweep side, [mol/s]

- $\dot{W}_{O_2,sweep}$: destruction rate of oxygen and on the sweep side in relation to reactor length, [mol/s]

3.3.3.1.5 Reaction constants

The forward water-splitting reaction rates are shown in *Eqn.* (2-6) will be fitted with water splitting data. The reaction rate constants for the oxygen incorporation/dissociation are shown in *Eqn.* (2-11) will be equipped using water feed – inert sweep data from Wu et al. [80]. The reaction rate constants are fitted using the Arrhenius form, as shown in *Eqn.* (2-21).

$$k_i = A_i \bullet exp\left(\frac{-Ea_i}{RT_{membrane}}\right) \tag{3-21}$$

Where,

- k_i: reaction rate constant, [m^4/mol s & $m^{2.5}$/$mol^{0.5}$ s]
- A_i: pre-exponential factor, [m^4/mol s & $m^{2.5}$/$mol^{0.5}$ s]
- Ea_i: activation energy, [kJ/mol]
- R: gas constant, [kJ/mol K]
- $T_{membrane}$: membrane temperature, [K]

Table 3-2 summarizes the pre-exponential factor, the activation energies for water splitting, and the kinetic oxygen incorporation/dissociation reactions.

Table 3-2: Summary of the reaction kinetic parameters on LCF-91 membrane [74]

Parameter	Pre-exponential factor (A)	Activation energy (Ea)
k_{f,H_2O}	1.93E-6 [m^4/mol s]	7.875 [kJ/mol]
k_{f,O_2}	5.66E-5 [$m^{2.5}$/$mol^{0.5}$ s]	10.6 [kJ/mol]
$\tilde{k}_{r,O_2}$	1.45E-3 [m/s]	111 [kJ/mol]
D_{v*}	4.98E-7 [m^2/s]	59.6 [kJ/mol]

* oxygen vacancy diffusivity (D_v) for LCF-91 was derived from separate transient dilatometry studies [117]

3.3.3.1.6 Gas species diffusion

The binary diffusion coefficient is used to model different gas species diffusion on either the feed or sweep side. The binary diffusion coefficients D_{AB} between species A and B are calculated using *Eqn.* (3-22).

$$D_{AB} = \frac{1\times10^{-3}T_s^{1.75}(1/M_A + 1/M_B)^{1/2}}{p_{total,s}\left[\left(\Sigma_A \upsilon_s\right)^{1/3} + \left(\Sigma_B \upsilon_s\right)^{1/3}\right]^2} \tag{3-22}$$

Where,

- T_s: the temperature for side 's', [K]
- M_A and M_B: atomic mass for species A and B, respectively, [g/mol]
- $\Sigma_A \upsilon_s$ and $\Sigma_B \upsilon_s$: diffusion volumes of molecules A and B, respectively.
- $p_{total,s}$: total pressure for side 's', [Pa]

3.3.3.1.7 Mass diffusion

Mass diffusion in the gas phase is used to solve the surface concentrations for both the water and the oxygen. The mass diffusion in the gas phase is modeled as shown in *Eqn. (3-23).*

$$J_i = h_{m,i,s}(X_{bulk,i,s} - X_{surface,i,s})C_{bulk,s} \tag{3-23}$$

Where,

- $h_{m,i,s}$: mass transfer coefficient for species 'i' on the side 's', [m/s]
- $X_{bulk,i,s}$: mole fraction of bulk species 'i' on the side 's'
- $X_{surface,i,s}$: mole fraction of surface species 'i' on the side 's'
- $C_{bulk,s}$: total molar concentration of the gas on the side 's', [mol/m^3]

The mass transfer coefficient is calculated directly using the gas-specific diffusion and Sherwood number, which is 3.61 for laminar flow in a square-shaped channel [110].

$$h_{m,i,s} = \frac{Sh}{2 \times H_s} \times D_i \tag{3-24}$$

Where,

- Sh: dimensionless number used in the mass-transfer operation, estimated as 3.61 for laminar flow.
- H_s: channel height in both feed and sweep sides 's'
- D_i: diffusivity of the species 'i'

3.3.3.2 Pressure drop

As the gas travels through the pipes, the friction causes the pressure to drop so that the pressure at the outlet is always lower than the pressure at the inlet, which is called friction loss or pressure drop. In general, the pressure drop is a function of several parameters, bed characteristics, e.g., bed height, particle diameter, porosity, and its distribution, and fluid characteristics, e.g., viscosity, density, and velocity [118].

The feed side channel is assumed to be a pipe, in which the concept of pressure gradient and Darcy friction factor in a fully developed flow can be used to solve the pressure drop in the feed side. Meanwhile, on the sweep side, seeing as the amount of catalyst mass used in the model is significantly low, which is related to the increase in porosity, it can be remarked that the porosity will not have significance on the pressure drop. The same concept of pressure gradient and friction factor in a fully developed flow can be applied to solve the pressure drop on the sweep side. The pressure drops for a gas flowing through a pipe can usually be neglected because of low gas density. However, when the flow is significantly high, and the channel is long and narrow, which is the case for the current suggested design, the pipe wall friction loss can signification, leading to a pressure drop. It is convenient to use the Darcy friction factor, which accounts for the pressure drop due to the friction with the pipe walls. Several assumptions are applied to use the Darcy friction factor to solve the pressure drop in the reactor's channels:

- Darcy friction factor (f) is assumed constant throughout the channel.

- Reactor channels are assumed to be operating at a steady state, which means the mass flow rate at any point down the reactor is equal to the entering mass flow rate ($\rho_0 \dot{V}_0 = \rho \dot{V}$).
- The ratio between the length of the reactor channel and the hydraulic diameter (L/D) is assumed to be very large since Darcy frictional factor is only applicable in such conditions.
- As the pressure drop gradient across the reactor length is calculated, a negative sign is added to convey the pressure dropping as the length changes (Δx).

$$\frac{\Delta p}{dx} = -f \times \frac{\rho \times u_m^2}{2D_h} \tag{3-25}$$

Where,

- f: Darcy friction factor, [dimensionless]
- ρ : fluid density, [kg/m^3]
- u_m: mean velocity, $[m/s]$
- D_h: hydraulic diameter, [m]

The Darcy friction factor is estimated based on flow condition and its Reynolds number. The Darcy friction factor is calculated for a fully developed laminar flow, as shown in *Eqn.* (3-26).

$$f = \frac{64}{\mathrm{Re}} \tag{3-26}$$

For fully developed turbulent flow, the Darcy friction factor also depends on the channel surface condition and increases with the increase of the surface roughness (*e*). The Darcy friction factor is estimated as shown in *Eqn.* (3-27).

$$\frac{1}{\sqrt{f}} = -2\log\left[\frac{e/D}{3.7} + \frac{2.51}{\mathrm{Re}\sqrt{f}}\right] \tag{3-27}$$

The Darcy friction factor is estimated for a smooth surface condition that encompasses an extensive Reynolds number range, as shown in *Eqn.* (3-28).

$$f = (0.790 \ln \mathrm{Re} - 1.64)^{-2} \ , \ 3000 \leq \mathrm{Re} \leq (5 \times 10^{6}) \tag{3-28}$$

Where,

- Re: Reynold's number, [dimensionless]
- *e*: surface roughness, [µm]
- D: channel diameter, [m]
- e/D: relative surface roughness

The hydraulic diameter is used to solve the pressure drop, seeing as the chosen membrane reactor depicts a rectangular-shaped cross-sectional area for both sweep and feed side channels. The hydraulic diameter for both the channels is estimated using *Eqn.* (3-29).

$$D_{h,s} = \frac{2 \times A_{c,channel}}{H + w_{full-channel}} \tag{3-29}$$

Where,

- $D_{h,s}$: hydraulic diameter for channel 's', [m]
- $A_{c,\ channel}$: a cross-sectional area for the channel, [m^2]
- H: full channel height, [m]
- $w_{full\text{-}channel}$: full channel width, [m]

The mean velocity of the gas flow is used to estimate the pressure drop. The mean velocity is estimated based on the volumetric flow rate and the cross-sectional area of the channel, as shown in *Eqn.* (3-30).

$$u_{m,s} = \frac{\dot{V}_{STP,\ s}}{A_{c,channel}} \tag{3-30}$$

Where,

- $u_{m,s}$: mean velocity of gas flow for channel 's', [m/s]

- $\dot{V}_{STP,S}$: volumetric flow rate at STP conditions for channel 's', [m^3/s]

3.3.3.2.1 Estimating the flow condition and length of the entrance region

A flow is described as a fully developed flow when the velocity profile does not change with streamwise direction. Physically, there would be no change in velocity profile towards the streamwise direction ($\delta u/\delta x = 0$). It is essential to compare the length of the entrance region (the distance traveled by the flow before it becomes fully developed and the size of the reactor to determine if the flow is fully developed. Suppose the entrance region is smaller than the length of the channel. In that case, it means that the inviscid core in the flow and boundary layer meet at the end of the entrance layer by the axis of the channel and results in one dense area, and it can be claimed that the flow is fully developed. The thickness of the boundary layer grows as the fluid flows downstream, and eventually, the layer edge reaches the channel centerline. Based on the aforementioned, the thickness of the boundary layer is half of the channel height.

(1) Reynolds number

$$\mathrm{Re}_s = \frac{\rho_s \times D_{h,s} \times u_{m,s}}{\mu_s}$$

$$\mathrm{Re}_s = \frac{\rho_s \times \frac{2A_{c,channel}}{(H + w_{Full-channel})} \times \frac{\dot{V}_{STP,s}}{A_{c,channel}}}{\mu_s} \quad (3\text{-}31)$$

Where,

- Re_s: Reynold's number for channel 's'
- ρ_s : fluid density for channel 's' (calculated using "Cantera" extension), [kg/m^3]
- $u_{m,s}$: mean velocity of gas flow for channel 's', [m/s]
- $D_{h,s}$: hydraulic diameter for channel 's', [m]
- μ_s : viscosity of fluid for channel 's' (calculated using "Cantera extension"), [kg/m s]

(2) Length of entrance region (laminar flow conditions)

$$\frac{L_{entrance}}{D_{h,s}} = 0.06 \times \mathrm{Re}_s \tag{3-32}$$

Where,

- $L_{entrance}$: entrance region length, [m]

Based on the above equations, the flow condition and the length of the entrance region are estimated for both the feed and sweep channels. *Table 3-3* shows the results obtained from estimating the Reynolds number. The Reynolds number is estimated to be 27.70 and 32.40 for the feed and sweep channels, respectively. The estimated Reynolds number lies in the laminar flow region (Re < 2300) which means the flows in both the feed and sweep channels are laminar flows. The entrance region for laminar flow conditions is calculated as shown in *Eqn.* (3-32). The entrance region is 6.5E-3 and 7.6E-3 m for the feed and sweep channels, respectively. The length of the feed and sweep channels is much longer than the estimated length of the entrance region, and therefore the flow in both channels is considered fully developed.

Table 3-3: Reynolds number and length of entrance region for feed and sweep sides

Parameter	Feed side	Sweep side
Re	27.70	32.40
ρ [kg/m^3]	0.22	0.21
A_c [m^2]	5E-5	5E-5
$H_{channel}$ [m]	2E-3	2E-3
$w_{full\text{-}channel}$ [m]	0.1	0.1
$\dot{V}_{STP}$ [m^3/s]	2.66E-4	2.66E-4
μ [kg/m s]	4.11E-5	3.44E-5
$L_{entrance}$ [m]	6.5E-3	7.6E-3
D_h [m]	3.9E-3	3.9E-3
$L_{channel}$ [m]	1.5	1.5

3.3.4 Ode45 MATLAB solver

MATLAB's standard solver for ordinary differential equations (ODEs) is used to model the one-dimensional plug flow membrane reactor in this research. This function implements a Runge-Kutta method with a variable time step for efficient computation. The ODE45 function is suitable for this model because it can solve first-order equations. The first step would be to develop first-order governing equations investigated in *Section 3.3.3.* The ode 45 functions are usually coded as follows:

$$[t, x] = \text{ode45}(@\text{fname}, \text{tspan}, \text{xinit}, \text{options}) \tag{3-33}$$

Where,

- fname: the name of the function Mfile used to evaluate the right-hand-side function
- tspan: the vector defining the beginning and end limits of integration
- xinit: the vector of initial conditions
- options: usually used to assign tolerances
- t: the value of the independent variable at which the solution array x is calculated
- x: an array (or matrix) with size length(t) by length (xinit)

3.3.5 Cantera extension

Cantera is an open-source suite of tools for problems involving chemical kinetics, thermodynamics, and transport processes. Cantera extension for MATLAB was used to define the gas mixture and determine some of its properties to solve the pressure and temperature change along the reactor length. The properties calculated using the Cantera extension are as follows:

(1) Defining the gas mixture

The mixture is defined as a class that inherits low-density gases that obey the ideal gas equation of state. Standard mass-action reaction rate expressions for low-density gases are also implemented. The set function defines the gas mixture properties and equates them to the temperature, pressure, and mole fractions.

```
gas_f = IdealGasMix('gri30.cti','gri30_mix')
gas_s = IdealGasMix('gri30.cti','gri30_mix')
```

set(gas_f,'T',T_f,'P',P_f,'X',X_gf)

set(gas_s,'T',T_s,'P',P_s,'X',X_gs)

(2) Thermal conductivity of gas mixture (feed and sweep gas mixtures)

Using the function 'thermalConductivity(gas)' returns thermal conductivity of gas in [W/m K]

thermalConductivity(gas_f)

thermalConductivity(gas_s)

(3) Non-dimensional enthalpies

Using the function 'enthalpies_RT(gas)' returns the non-dimensional enthalpies of all species and are divided by RT

enthalpies_RT(gas_f)

enthalpies_RT(gas_s)

(4) Specific heat capacities

Using the original function returns molar-basis specific heats at constant pressure with unit[J/kmol-K]

cp_mole(gas_f)

cp_mole(gas_s)

(5) Gas mixture density (feed and sweep gas mixtures)

Using the function 'density(gas) results in the density of the gas mixture in [kg/m^3]

density(gas_f)

density(gas_s)

(6) Gas mixture viscosity (feed and sweep gas mixtures)

Using the function 'Viscosity(gas)' returns the viscosity of the gas mixture in [kg/m s]

viscosity(gas_f)

viscosity(gas_s)

3.3.6 Tolerances

Relative tolerances measure the error relative to the magnitude of each solution component. It controls the number of correct digits in all solution components, except those more diminutive than the absolute tolerance. This tolerance is a threshold below which the solution's value becomes unimportant. If the solution |y| is smaller than absolute tolerance, the solver does not need to obtain any correct digits in |y|. The absolute and relative tolerances were altered to examine their effect on the oxygen molar flow rates and determine the most suitable tolerances. Adjusting the relative tolerance did not significantly affect the molar flow rates; it was kept at 1E-7. On the other hand, alerting the absolute tolerance (while keeping the relative tolerance constant) affects the molar flow rates, as shown in *Figure 3-5*. The figure shows oxygen molar flow rates versus absolute tolerance (in log scale).

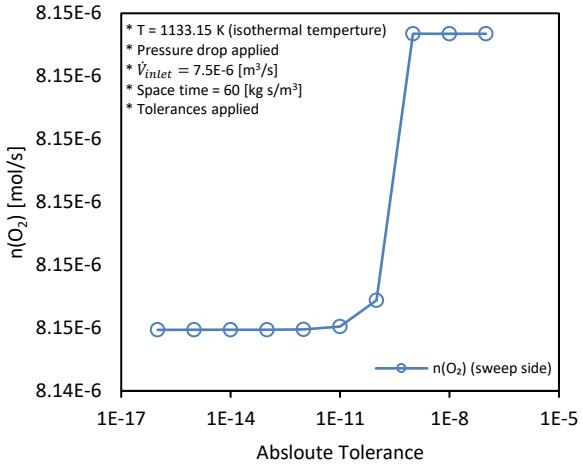

Figure 3-5: Absolute tolerances effect on oxygen molar flow rate

Figure 3-6 shows the oxygen trend versus the reactor length for scenarios with different absolute tolerances. The figure shows that all the scenarios maintain the same oxygen trend. However, the change of the absolute tolerance (while maintaining fixed relative tolerances) alters the number of iterations and the step size.

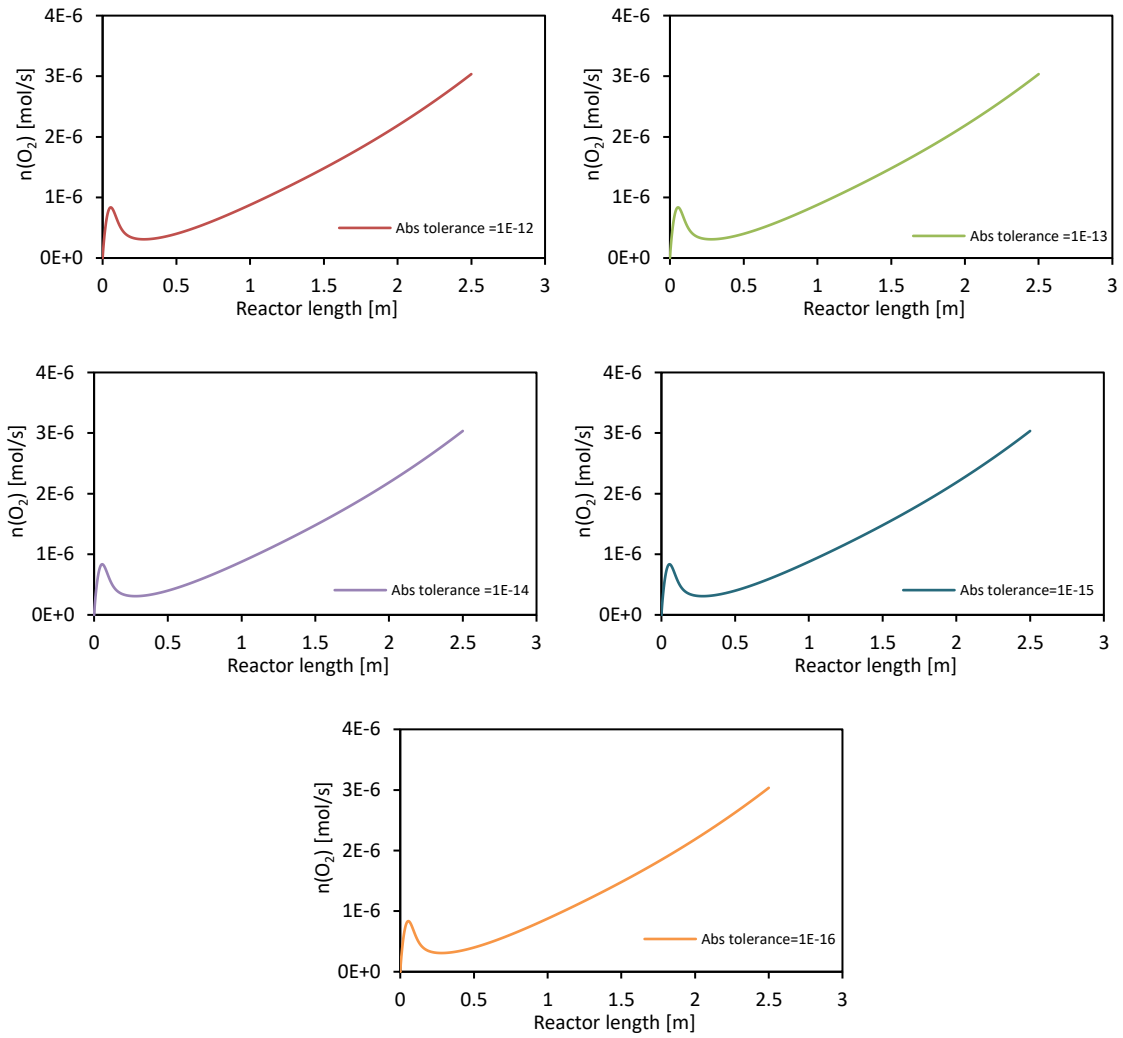

Figure 3-6: Oxygen trend versus the reactor length for different absolute tolerances (T = 1133.15 K (isothermal temperature), pressure drop applied, $\dot{V}_{inlet}$ = 7.5E-6 [m^3/s], space time = 60 [kg s/m^3] and Rel tolerance = 1E-7)

As shown in *Table* 3-4, increasing the absolute tolerance increases the number of steps, making the code more reliable. In addition, the table shows the minimum calculated step size (Δx) for every scenario. A more significant number of steps significantly reduces the step size by integrating more steps. This reduction in step size allows the model to mimic a more realistic membrane reactor by minimizing the homogeneous blocks assumption.

Table 3-4: Effect of change of absolute tolerance on the number of steps and step size

Absolute	Relative	N. of steps	Δx
1E-12	1E-7	461	4.60E-5
1E-13	1E-7	685	1.01E-5
1E-14	1E-7	785	2.44E-6
1E-15	1E-7	825	2.94E-7
1E-16	1E-7	861	8.72E-8

An absolute tolerance of 1E-14 is chosen for the model for several reasons. Firstly, the trend shown in *Figure* 3-5 can determine the most suitable absolute tolerance to use, seeing as the oxygen molar flow rates started to stabilize, starting from 1E-14 tolerance to 1E-16 tolerances. Secondly, the absolute tolerance of 1E-14 averages a suitable number of iterations and step size for analysis purposes.

3.4 Model validation

The inlet and output molar flow rates of the species are used to calculate conversion, selectivities, yield, and rates of formation values. The model was validated by comparing the theoretical predictions of differential kinetics with the experimental results for OCM in a micro catalytic fixed-bed reactor with La_2O_3/CaO as a catalyst, reported by Stansch et al. [91]. The validation of the membrane reactor model was performed to ensure that the mathematical models could reasonably predict the oxygen-permeable membrane reactor performance. Several assumptions were applied to the developed membrane reactor to validate the kinetics of the sweep side:

(1) The membrane's function of transporting oxygen from the feed side to the sweep side is switched off; instead, oxygen is fed directly to the sweep side.
(2) Feed side water-splitting reaction is neglected (since it depends on J_v).
(3) Temperature change along the reactor length is assumed negligible (isothermal condition).
(4) Pressure drop along the reactor length is assumed negligible.
(5) The sweep side-channel cross-sectional area is equated to the cross-sectional area provided in the catalyst paper by Stanch et al. [91], assuming a square-shaped channel for the membrane reactor (as shown in *Eqn.* (3-34) and *Eqn.* (3-35)).

$$A_{(circular\ cross-sectional)} = A_{(\text{rectangular } cross-sectional)}$$
$$\frac{\pi d^2}{4} = L \times w \tag{3-34}$$

Assuming a squared shaped channel for the membrane reactor for simplification,

$$A_{(circular\ cross-sectional)} = A_{(\text{squared } cross-sectional)}$$
$$\frac{\pi d^2}{4} = H \times H$$
$$\frac{\pi d^2}{4} = H^2 \tag{3-35}$$
$$H = \sqrt{\frac{\pi d^2}{4}}$$

Where,

- L: channel length for membrane reactor, [m]
- w: channel's width membrane reactor, [m]
- H: channel's height membrane reactor, [m]
- d: diameter of circular channel for catalyst reactor, [m]

The reactor's dimensions and the inlet operating conditions for both the reactors are kept consistent to ensure the validation has high accuracy. The reactor's dimensions and the inlet operating conditions are shown in *Table 3-5*. The dimensions for the micro catalytic mixed bed reactor by Stansch et al. [91] are based on the reactor schematic shown in the referenced paper. The operating conditions are all based on Figure 6 in the referenced paper.

Table 3-5: Micro catalytic fixed-bed reactor vs. membrane reactor (dimensions and inlet operating conditions)

Parameter	Microcatalytic fixed-bed reactor by Stansch et al. [91]	Membrane reactor
Channel length ($L_{channel}$) [m]	0.227	0.227
Channel height ($H_{channel}$) [m]	-	5.3E-3
Channel width ($w_{channel}$) [m]	-	5.3E-3
Channel radius ($r_{channel}$) [m]	3E-3	-
Cross sectional area ($A_{cross\ sectional}$) [m^2]	2.83E-5	2.83E-5
Space-time [kg s/m^3]	1.86	1.86
Volumetric flow rate ($\dot{V}_{STP}$) [m^3/s]	4.9E-3	4.9E-3
Number of steps	239	239
Inlet oxygen partial pressure (p_{O_2}) [Pa]	5304.9	-
Inlet methane partial pressure (p_{CH_4}) [Pa]	70000	-
Inlet nitrogen partial pressure (p_{N_2}) [Pa]	24695	-
Inlet oxygen mole ratio (R_{O_2}) [Pa]	-	0.18
Inlet methane mole ratio (R_{CH_4}) [Pa]	-	0.7
Inlet nitrogen mole ratio (R_{N_2}) [Pa]	-	0.12

3.4.1 Influence of oxygen partial pressure on the formation rate of C_{2+} hydrocarbons and the formation rate of CO_x

The influence of altering the oxygen partial pressure (p_{O_2}) the rate of formation of C_{2+} hydrocarbons and carbon oxides has been investigated in this section. The initial conditions are adjusted to take into consideration the influence of altering the initial oxygen partial pressure ($p_{O_2,inlet}$) (2.93 and 18.35 kPa

at 973.1 K) and (1.23 and 18.12 kPa at 1073.2 K) while considering a constant initial partial pressure of methane ($p_{CH_4,inlet}$) and also alternating between two different reactor temperatures. The corresponding initial nitrogen partial pressure is calculated based on *Eqn.* (2-17) shown in *Chapter 2.* Altering the partial pressure affects the initial molar ratio of the inlet species and affects the species' initial mole ratio, as shown in *Eqn.* (3-36) and *Eqn.* (3-37), respectively.

$$R_{(i)} = \frac{p_{(i)}}{p_{total}} \tag{3-36}$$

$$\dot{n}_{(i)} = R_{(i)} \times \dot{n}_{total} \tag{3-37}$$

Where,

- R_i: Mole ratio for species 'i', [dimensionless]
- p_i: partial pressure for species 'i', [pa]
- p_{total}: total inlet pressure, [pa]
- $\dot{n}_{(i)}$: molar flow rate for species 'i', [mol/s]
- $\dot{n}_{total}$: total molar flow rate for species, [mol/s]

In addition, the rate of formation of CO_x and higher hydrocarbon (C_{2+}) is calculated using *Eqn.* (3-38) and *Eqn.* (3-39), respectively.

$$R_{C_{2+}} = \frac{\dot{n}_{C_2H_6,(outlet)} + \dot{n}_{C_2H_4,(outlet)}}{\mathrm{m}_{catalyst}} \tag{3-38}$$

$$R_{COx} = \frac{(\dot{n}_{CO_2,(outlet)} + \dot{n}_{CO,(outlet)}) - \dot{n}_{CO_2,(inlet)}}{\mathrm{m}_{catalyst}} \tag{3-39}$$

Where,

- $R_{C_{2+}}$: rate of formation of C_{2+} hydrocarbons, [mol/kg s]

- R_{CO_x}: rate of formation of carbon oxides (CO_x), [mol/kg s]

The initial oxygen partial pressures were varied from 1.23 to 5.30 kPa. At the same time, the isothermal reactor temperature was alternated between 1073.2 and 973.1 K. The solid lines show the experimental results obtained from Stansch et al. [90]. While the dotted lines show the developed membrane reactor results. *Figure 3-7* shows the influence of $P_{O_2,inlet}$ on the formation rate of C_{2+} hydrocarbons and the formation rate of CO_x reaction conditions. For the C_{2+} rate of formation, at higher temperature (1073.2 K), the rate of hydrocarbon formation passed through its maximum; this is because the increasing temperature led to an increase in the reaction rates and also the diminishing of the inhibiting effect of oxygen at higher temperatures [91]. At the same temperature, the rate of carbon oxides formation also increased with the partial pressure of oxygen. The rate was almost a linear function of the partial pressure of oxygen. This might be because the formation of carbon oxides was not inhibited by oxygen, as observed for the formation of C_{2+} hydrocarbon.

At lower temperatures (973.1 K), the formation of C_{2+} hydrocarbons significantly decreased; this might be due to the inhibiting effect of carbon dioxide. The increasing partial pressure of carbon dioxide led to a decrease in the ethylene-to-ethane ratio [91]. The results obtained show that the developed membrane model can predict the effect of altering the reactor operating conditions on the rate of formation of the primary products, including C_{2+} hydrocarbons and carbon oxides.

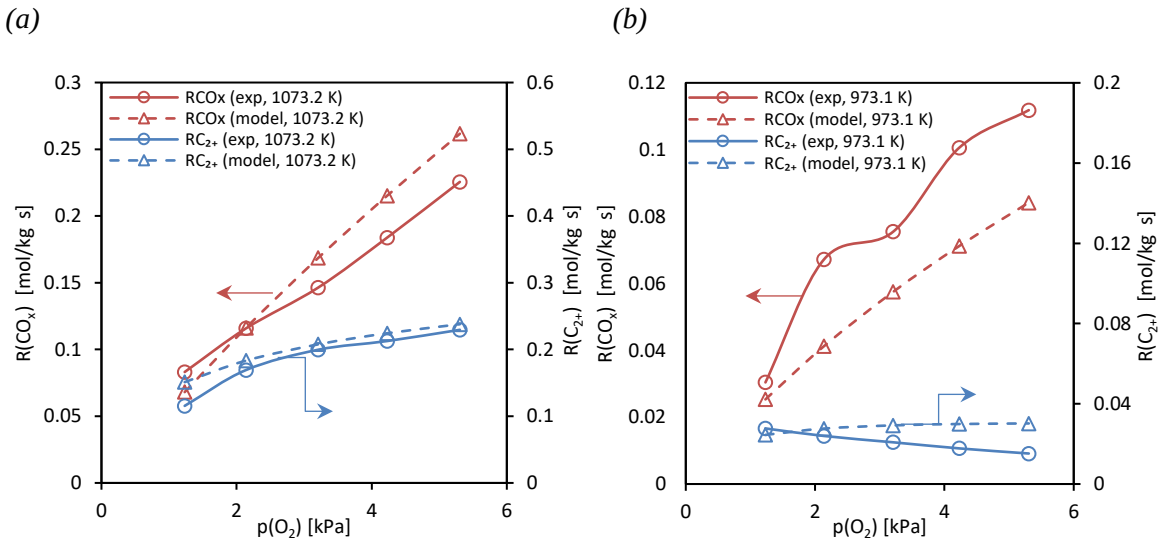

Figure 3-7: Influence of $p(O_2)_{inlet}$ on the formation rate of C_{2+} hydrocarbons and the formation rate of CO_x reaction conditions at (a) 1073. K and (b) 973.1 K

3.4.2 Influence of space time and temperature on methane and oxygen conversion, the yield of C_{2+} hydrocarbons, and CO_x

The influence of space-time and reactor temperature on reactor performance parameters has been investigated in this section to validate the process of the developed membrane reactor model. These parameters include methane and oxygen conversion, calculated using *Eqn.* (3-40) and *Eqn.* (3-41), respectively.

$$X_{CH_4} = \frac{(\dot{n}_{C_2H_4,(outlet)} \times 2) + (\dot{n}_{C_2H_6,(outlet)} \times 2) + (\dot{n}_{CO_2,(outlet)}) + (\dot{n}_{CO,(outlet)})}{(\dot{n}_{C_2H_4,(inlet)})} \times 100 \quad (3\text{-}40)$$

$$X_{O_2} = (\frac{\dot{n}_{O_2,(inlet)} - \dot{n}_{O_2,(outlet)}}{\dot{n}_{O_2,(inlet)}}) \times 100 \quad (3\text{-}41)$$

Where,

- X_{CH_4} : methane conversion, [%]
- X_{O_2}: oxygen conversion, [%]
- $\dot{n}_{i,inlet}$: inlet species ‘i' molar flow rates, [mol/s]
- $\dot{n}_{i,outlet}$: outlet species ‘i' molar flow rates, [mol/s]

The yield of the reactor output is also investigated. The selectivity and yield of the higher hydrocarbons (C_2H_6 and C_2H_4) are shown in *Eqn.* (3-42) and *Eqn. (3-43)*, respectively. Also, the CO_2 (CO and CO_2) selectivity and yield are shown in *Eqn.* (3-44) and *Eqn.* (3-45).

$$S_{C_{2+}} = 2 \times \frac{\dot{n}_{C_2H_4,(outlet)} + \dot{n}_{C_2H_6,(outlet)} - \dot{n}_{C_2H_4,(inlet)} - \dot{n}_{C_2H6,(inlet)}}{\dot{n}_{CH_4,(inlet)} - \dot{n}_{CH_4,(outlet)}} \quad (3\text{-}42)$$

$$Y_{C_{2+}} = X_{CH_4} \times S_{C_{2+}} \quad (3\text{-}43)$$

$$S_{CO_x} = \frac{\dot{n}_{CO_2(outlet)} + \dot{n}_{CO(outlet)} - \dot{n}_{CO_2(inlet)} - \dot{n}_{CO(inlet)}}{\dot{n}_{CH_4(inlet)} - \dot{n}_{CH_4(outlet)}} \quad (3\text{-}44)$$

$$Y_{CO_x} = X_{CH_4} \times S_{CO_x} \quad (3\text{-}45)$$

Where,

- S_{CO_x}: CO_x selectivity, [%]
- $S_{C_{2+}}$: C_{2+} hydrocarbons selectivity, [%]
- $Y_{C_{2+}}$: C_{2+} hydrocarbons yield, [%]
- Y_{CO_x}: CO_x yield, [%]

For all the figures, the space-time was varied from 1.87 to 25 kg s/m^3. At the same time, the isothermal reactor temperature was alternated between 1103.2 and 973.1 K. The solid lines show the experimental results obtained from Stansch et al. [90]. At the same time, the dotted lines show the developed membrane reactor results. It is noticeable that there is an almost asymmetrical distribution of the data points for all variables. This shows that the developed membrane model can predict the effect of altering the reactor operating conditions on conversions of methane and oxygen and yields to C_{2+} hydrocarbons and carbon oxides with a high degree of accuracy.

Figure 3-8 shows the influence of altering the space, time, and temperature on methane and oxygen conversion. At 1103.2 K, almost complete conversion of oxygen (X_{O_2} > 95%) was already achieved for the contact time of 25 kg s/m^3. At 973.1 K, the conversion of oxygen increased slowly with space-time compared to the dependences measured at 1103.2 K. For both temperatures, the course of the conversion of methane corresponded to that of oxygen. No further methane conversion with space-time was measured when oxygen conversion was complete.

Figure 3-9 shows the influence of altering the space, time, and temperature on the C_{2+} yield of ethane and ethylene. For ethane yield, at longer contact times, the characteristics of the ethane yield depended on temperature. At high temperatures (1103.2 K), the yield of ethane leveled off, although oxygen was still available. At the same temperature, the ethane yield characteristics show its maximum yield. For

ethylene yield, the dependence of ethylene yield on the space-time at low values of this parameter confirms the generally accepted thesis that ethylene is formed in a consecutive reaction of ethane. However, the leveling off observed at long contact times indicates that ethylene also is an intermediate product of the OCM reaction. The leveling off observed at long space-time indicates that ethylene also is an intermediate product of the OCM reaction [91].

Figure 3-10 shows the influence of altering the space-time and temperature on carbon oxides (CO and CO_2). For CO yield, at high temperatures (1103.2 K) and low space-time (space-time < 3.69 kg s/m^3), the yield of carbon monoxide passed through a maximum value. The yield drop occurred at high temperatures, mainly in the range of space times for which oxygen was still available. However, when oxygen was converted entirely, the yield decreased further with the contact time. For CO_2 yield, there is a noticeable increase for all temperatures with space-time. Rapid growth at short contact times indicates that carbon dioxide is also the primary product [91].

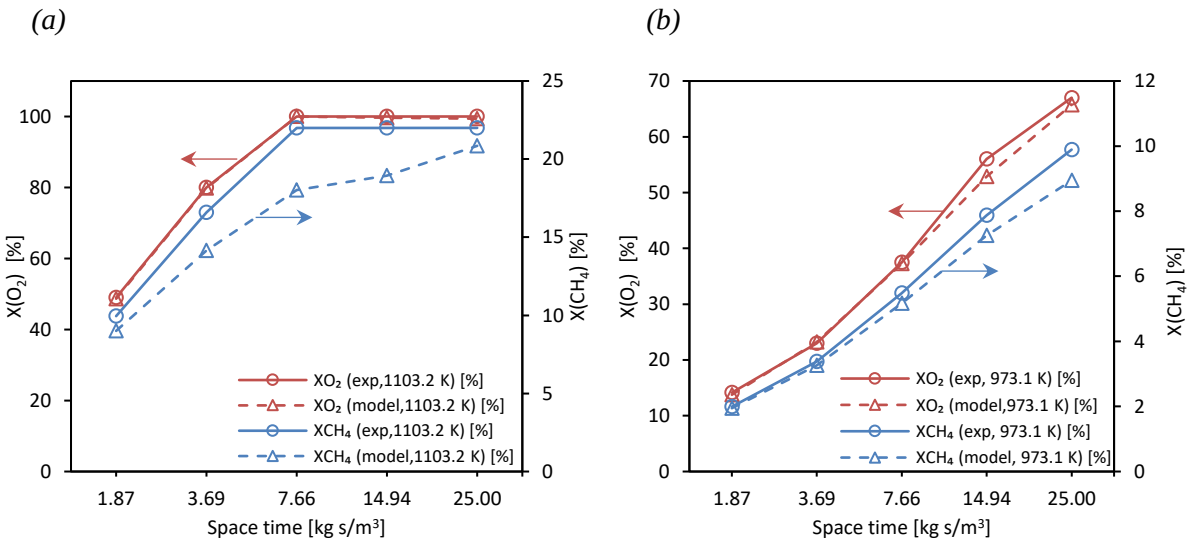

Figure 3-8: Influence of space time and temperature on methane and oxygen conversion at (a)1103.3 K and (b) 973.1 K

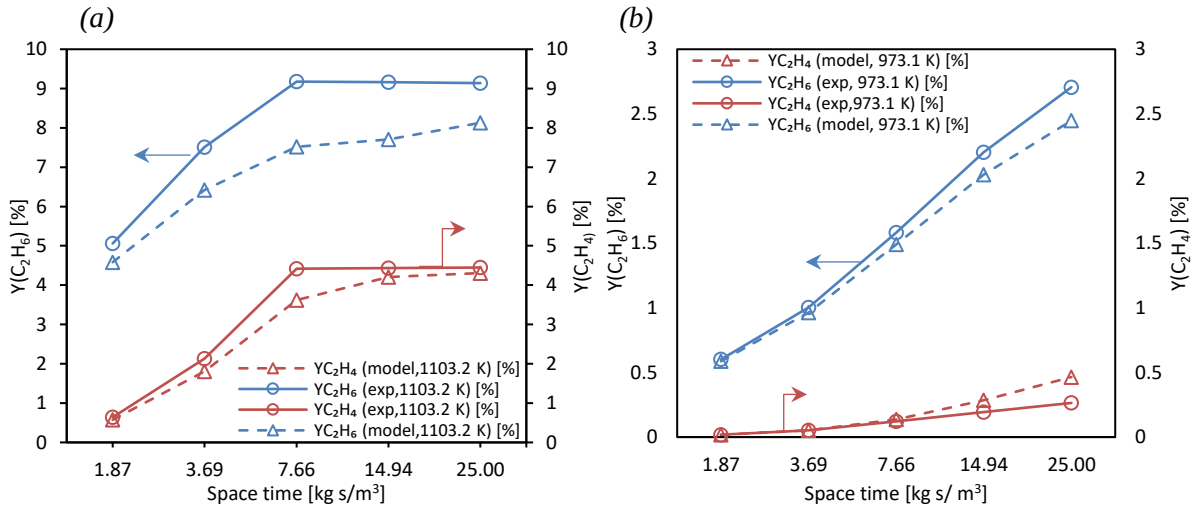

Figure 3-9:Influence of space time and temperature on yield of C_{2+} hydrocarbons (a) 1103.3 K and (b) 973.1 K

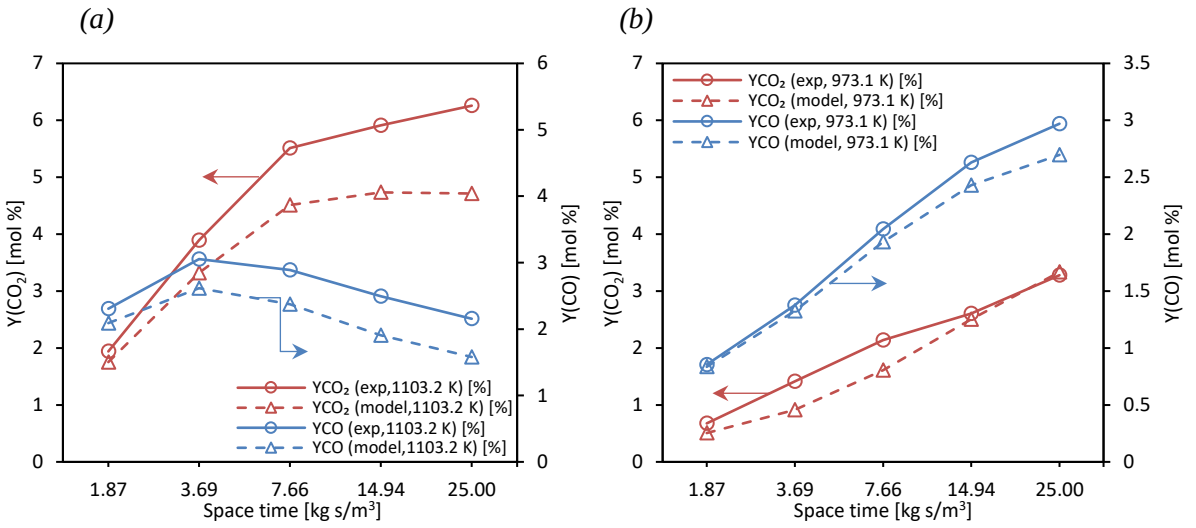

Figure 3-10: Influence of space time and temperature on yield of carbon oxides (a)1103.3 K and (b) 973.1 K

3.4.3 Average parity plots (± 20 % relative prediction error)

A parity plot is a scatterplot that compares experimental data against model data. Each point has coordinates, where x is the experimental value and y is the corresponding model value. A dotted line of the equation y = x is added as a reference. The limits of the parity plots are set for ± 20 %, shown by the two solid black lines.

Figure 3-11 shows the experimental vs. model results for the oxygen and methane conversion at 973.1 and 1103.2 K. The prediction of the methane and oxygen conversions at 1103.2 and 973.1 K are well within the ± 20% limit compared to experimental results.

Figure 3-12 shows experimental vs. model results for C_{2+} hydrocarbons yield at 973.1 and 1103.2 K. The average relative prediction for the rate of formation of higher hydrocarbons and rate of formation of carbon oxides at 1103.2 and 973.1 K are well within the 20 % limit compared to experimental results.

Figure 3-13 shows experimental vs. model results for CO_x yield at 973.1 and 1103.2 K. The majority of the model predicted data points are at 1103.2 and 973.1 K are well within the 20% limit compared to experimental results. In contrast, some data points were predicted with lower accuracy, which might be because of several sources of errors that may have resulted in some of the differences between the published experimental results reported by Stansch et al. [91] and the generated results using the membrane reactor model :

(1) Fitting error (standard error of estimate): is due to estimating the actual values when plotting them; it accompanies the estimated activation energies values ($E_{a,j}$) and pre-exponential values ($k_{0,j}$).

(2) Numerical error: This type of error is due to the Δt (time step). In order to reduce the numerical error, the time step must be changed to a point where the results' difference is not differential.

It is noticeable that an almost asymmetrical distribution of the data points on both diagonal sides was obtained for all variables. This observation can be used to conclude that the membrane reactor mode developed can predict the reactor's performance parameters (including conversions of methane and oxygen and yields to C_{2+} hydrocarbons and carbon oxides with an average accuracy between ± 20% average relative error limit.

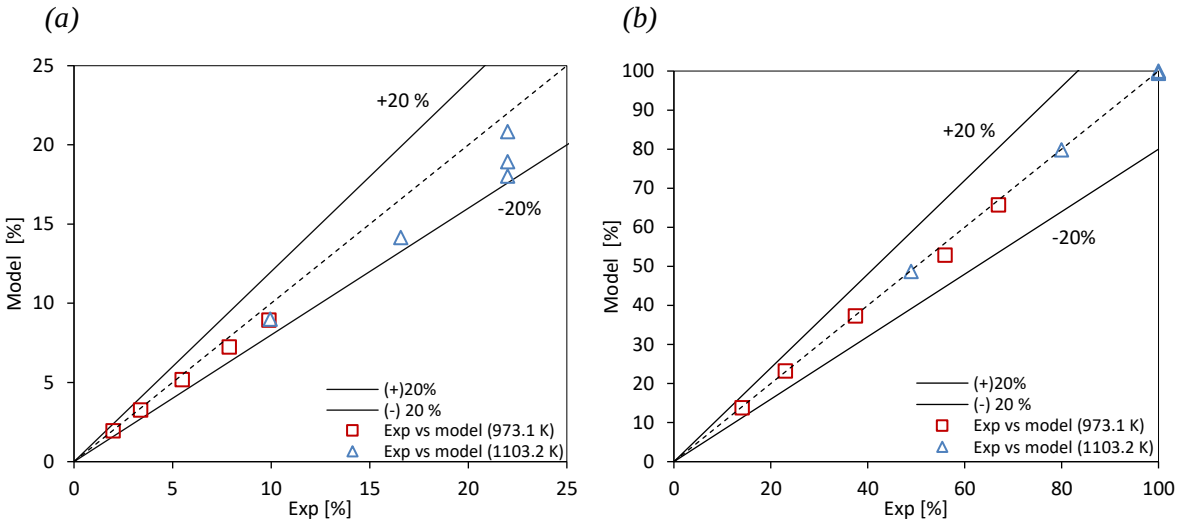

Figure 3-11: Experimental vs. model results for the oxygen (a) and methane (b) conversion at 973.1 and 1103.2 K

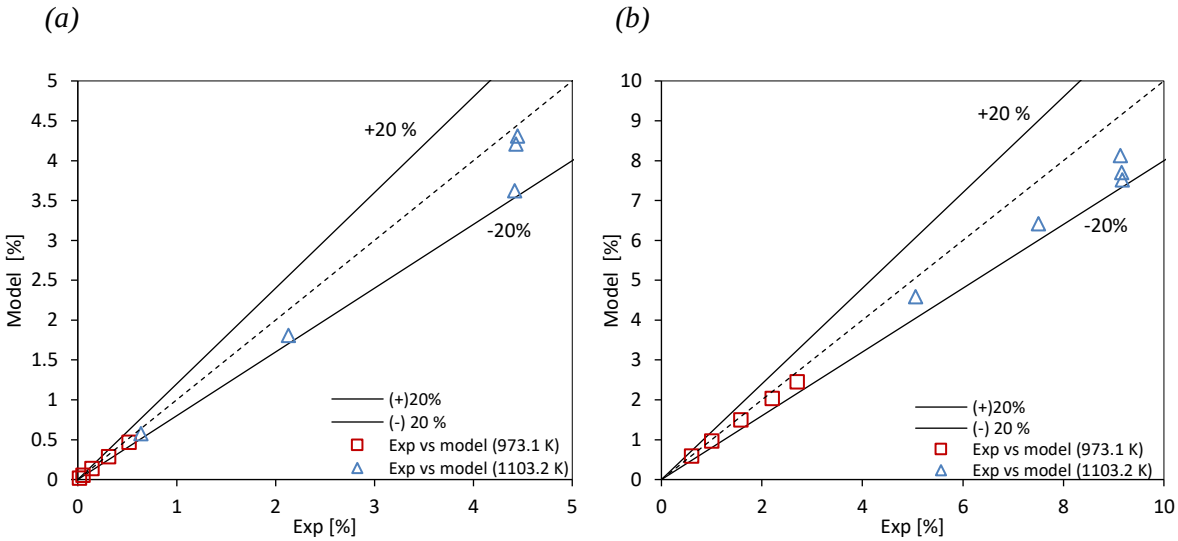

Figure 3-12: Experimental vs. model results for (a) C_2H_4 and (b) C_2H_6 yield at 973.1 and 1103.2 K

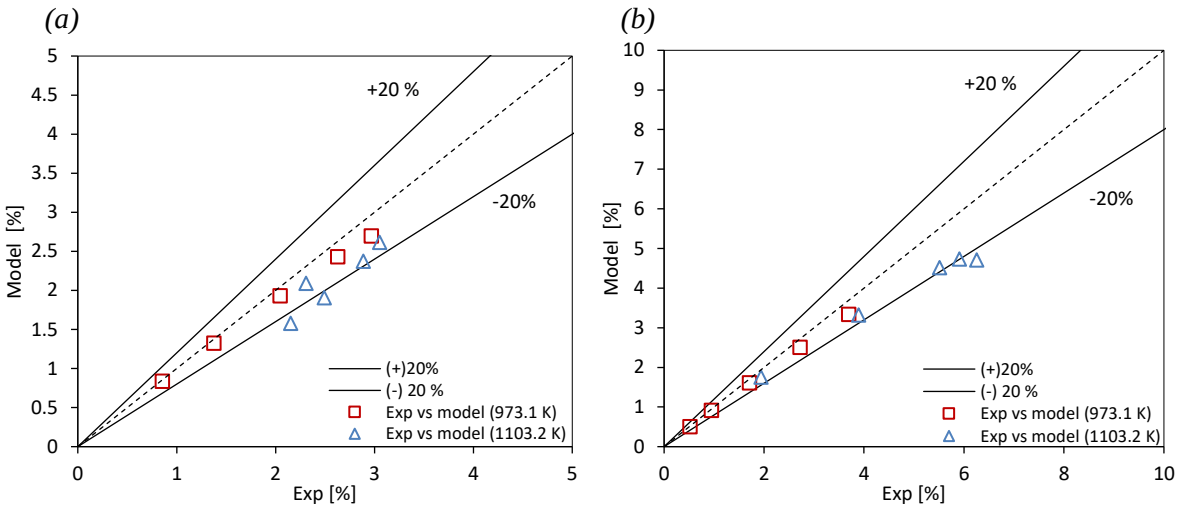

Figure 3-13: Experimental vs. model results for (a) CO and (b) CO_2 yield at 973.1 and 1103.2 K

3.4.4 Influence of altering channel width

Based on the membrane reactor model shown in *Figure 3-1*, the membrane reactor model is computed along the length of the reactor. The width of the channel does not influence the membrane reactor model or the governing equations. This is because the membrane reactor model is modeled in one-dimensional along the reactor length, which means that the direction of the width is assumed to be uniform. That is why it is essential to validate the accuracy of the model by investigating the effect of altering the channel width (membrane width) while fixing the ratio between the volumetric flow rate and the channel ($\dot{V}_{STP}$/$w_{membrane}$). Based on mass balance equation on the feed side shown in *Eqn. (3-5)*, the channel width (membrane width) is a constant parameter. The mass balance can be solved as shown in *Eqn. (3-46)*.

$$\frac{d\dot{n}_{j,feed}}{dx \times w_{membrane}}[mol/s\ m^2] = (+/-)J_v[mol/s\ m^2] \tag{3-46}$$

The channel width was altered between three different cases. The inlet volumetric flow rate was recorded in the three cases and used to find the ratio between the two parameters. $\dot{V}_{STP}$/$w_{membrane}$ is maintained constant, and the ratio between the molar flow rate and the channel width ($\Delta\dot{n}_j$/$w_{membrane}$) is obtained. The $\Delta\dot{n}_j$/$w_{membrane}$ was found to be consistent as the width was altered and the $\dot{V}_{STP}$/$w_{membrane}$

is maintained, which correlates with the hypothesis and validates that the model is working correctly based on the assumptions taken. The result of the analysis is shown in *Appendix A.*

3.5 Chapter summary

This chapter investigates the implementation of the OCM process in an inorganic catalyst membrane reactor for the co-production of hydrogen and ethylene. The chapter showcased the development of a catalytic membrane reactor. The model is based on a plug-flow reactor that mimics a monolith membrane reactor design. The membrane reactor is divided into a feed, sweep, and membrane. On the feed side, the oxygen incorporation process is through the gaseous oxygen and oxygen vacancies at the membrane surface to form lattice oxygen. Then the lattice oxygen diffuses through the membrane driven by potential chemical gradients. Once the lattice oxygen reaches the sweep side, a reaction between lattice oxygen and electron holes at the membrane surface releases gases oxygen. The final step includes the mass transfer of gases oxygen from the membrane surface (sweep side) to the gas (methane) stream, which provides the necessary oxygen molecule for OCM reactions to convert methane to higher hydrocarbons such as ethane and ethylene. The development of the model included the development of the governing equations, including mass balance and pressure drop. MATLAB ordinary differential solver (Ode45) is used to solve governing differential equations that concern mass balance and pressure drop along the length of the reactor. The chapter also discussed the development of the resistance network and the connection between vacancy flux and oxygen flux. The resistances network includes the gas species diffusion on either the feed or sweep side. In addition, mass diffusion in the gas phase is used to solve the surface concentrations for both water and oxygen.

The membrane reactor model was validated by comparing the theoretical predictions of differential kinetics with the experimental results for OCM in a micro catalytic fixed-bed reactor with La_2O_3/CaO as a catalyst, reported by Stansch et al. [91]. Parity plots are constructed with average error limits of ± 20 %. It is noticeable that an almost asymmetrical distribution of the data points on both diagonal sides was obtained for all variables. This observation can conclude that the membrane reactor mode developed can predict reactors' performance parameters (including conversions of methane and oxygen and yields to C_{2+} hydrocarbons and carbon oxides with an average accuracy of between 20% average relative error limit. Lastly, in order to further validate the accuracy of the membrane reactor model developed the influence of altering channel width while maintaining the $\dot{V}_{STP}/w_{membrane}$ constant. The $\Delta\dot{n}_j/w_{membrane}$ was found to be consistent as the width was altered and the$\dot{V}_{STP}/w_{membrane}$ is maintained

which correlates with the hypothesis and validates that the model is working correctly based on the assumptions taken.

In *Chapter 4*, the one-dimensional membrane reactor model developed will be analyzed further by developing a base case that establishes the correct relationships between these parameters and the membrane reactor performance. A systematic analysis and parametric study will be presented to analyze the base case scenario thoroughly. Base case analysis remarks will be used to develop a target case that demonstrates if the technology is industrially applicable through investigating the membrane reactor's output C_{2+} yield.

Chapter 4

Membrane reactor model results analysis

4.1 Chapter introduction

This chapter builds on the one-dimensional oxygen permeable catalytic membrane reactor model developed in *Chapter 3*. A base case is developed and analyzed by establishing the correct relationships between several parameters and the membrane reactor performance. A systematic and sensitivity analysis will be presented to identify the critical parameters that affect the co-production performances in a membrane reactor. In addition, the economic feasibility of the OCM technology for the co-production of ethylene and hydrogen is investigated by estimating the required ethylene yield and selectivity needed to obtain an economically favorable ethylene price. Base case analysis remarks will be used to develop a target case that demonstrates if the technology is industrially applicable through investigating the membrane reactor's output C_{2+} yield.

The target case developed will also be analyzed to understand the effect of improving the membrane reactor's operating condition. Lastly, this chapter also investigates the benefits of implementing the membrane in an OCM catalytic reactor to produce higher hydrocarbons versus using a pre-mixed reactor for the same purpose. The two scenarios will be compared to draw several conclusions about the impacts of an oxygen-permeable membrane and its influence on the OCM reactor performance and, more importantly, on the environment.

4.2 Base case

4.2.1 Reactor geometry and operating conditions

The reactor dimensions and the initial operating conditions for the developed base case are summarized in *Table 4-1*. The reactor dimensions were consistent with similar membrane reactors' literature values. The operating conditions were based on a comprehensive 10-step kinetic model of the oxidative coupling of methane to C_{2+} hydrocarbons over a La_2O_3/CaO catalyst based on kinetic measurements in a micro catalytic fixed-bed reactor.

Table 4-1: Dimensions and operating conditions (base case)

Parameter	Feed side	Sweep side	Membrane
Membrane thickness (t) [m]	-	-	9E-4
Full Channel height (H) [m]	2E-3	2E-3	-
¼ Channel height ($H_{channel}$) [m]	1E-3	1E-3	-
Channel length ($L_{channel}$) [m]	1.50	1.50	-
Channel width ($w_{channel}$) [m]*	5E-2	5E-2	-
Temperature (T) [K]	1103.3	1103.3	1103.3
Total inlet pressure ($p_{total,inlet}$) [Pa]	100000	100000	-
Inlet water mole fraction	0.8	-	-
Inlet nitrogen mole fraction (feed)	0.2	-	-
Inlet methane mole fraction	-	0.7	-
Inlet nitrogen mole fraction (sweep)	-	0.3	-
Volumetric flow rate (STP) [m^3/s]	7.23E-5	7.23E-5	-
Space time [kg s/m^3]	-	1.86	-
Catalyst density [kg/m^3]	-	3600	-
Catalyst porosity	-	0.9995	-
Total catalyst mass [kg]	-	1.35E-4	-
Total membrane surface area [m^2]	-	-	7.5E-2
Catalyst per membrane surface area [kg/m^2]	-	1.8E-3	-

* Channel width is equal to the membrane width based on the reactor schematic

The membrane thickness was kept at 9E-4 m, consistent with the membrane thickness reported by Wu et al. [74]. The channel height was maintained at 1 mm for a quarter of the channel, consistent with the membrane reactor model developed by Wu et al. [74]. The feed and sweep sides control volumes

are assumed to be 1/4 of the entire reactor channel. This estimation is possible due to symmetry, which means the boundaries of the chosen control volumes can be assumed to have no interactions with the other channels that share the same wall with the considered channels. The feed and sweep sides control volumes assumption mentioned will allow us to study the heat and mass transfers between the membrane and the two feed and sweep sides. The channel length and width magnitude for both feed and sweep channels was consistent with the literature's oxygen transport membrane models [119,120]. Mastropasqua et al. [119] reported a channel width of 2.15E-2 m for their developed one-dimensional model for a planar oxygen transport membrane module. Rodriguez et al. [120] reported a channel length of 4 m for their proposed reactor design for ethylene production.

Water is fed to the membrane feed surface, and it reacts with the oxygen vacancies to produce hydrogen. In contrast, the oxygen atom from water incorporates the lattice oxygen and diffuses through the membrane due to the potential chemical gradient. On the other side, methane reacts with the lattice oxygen ions to produce higher hydrocarbon. The sweep side operating conditions are based on the micro catalytic fixed-bed reactor developed by Stansch et al. [91]. The catalyst porosity reported by Stansch et al. [91] for their micro catalytic fixed-bed reactor was altered on the sweep side because there is a direct relationship between the porosity and the total catalyst mass (as shown in *Eqn. (4-3)).* Adjusting the porosity and reducing the total catalyst mass reduces the catalyst mass per step, directly affecting the formation/destruction rates, as explained in *section 3.3.3.1.1.*

$$V_{channel,sweep} = L_{channel,sweep} \times H_{channel,sweep} \times w_{channel,sweep} \tag{4-1}$$

$$V_{catalyst} = V_{channel,sweep} \times (1-\phi) \tag{4-2}$$

$$M_{total,catalyst} = V_{catalyst} \times \rho_{catalyst} \tag{4-3}$$

Where,

- $V_{channel,sweep}$: total volume of the sweep side channel, [m^3]
- $L_{channel}$: length of the sweep side channel, [m]

- $H_{channel,sweep}$: height of sweep side channel, [m]
- $w_{channel,sweep}$: width of the sweep side channel, [m]
- $V_{catalyst}$: total volume of catalyst in sweep side, [m^3]
- ϕ : catalyst porosity
- $M_{total,catalyst}$: total catalyst mass, [kg]
- $\rho_{catalyst}$: catalyst density, [kg/m^3]

In addition, the space-time was adjusted to match the lowest reported value by Stansch et al. [91] to maintain a suitable volumetric flow rate, seeing as the space-time directly affects the volumetric flow rate (on the sweep side) according to *Eqn. (4-4).*

$$\dot{V}_{STP,(sweep)} = \frac{M_{total,catalyst}}{\text{space time}} \tag{4-4}$$

Where,

- $\dot{V}_{STP,(sweep)}$: volumetric flow rate at STP conditions on sweep side, [m^3/s]

4.2.2 Model outputs (base case)

It is important to note that most of the research in this field has been focused on improving the C_{2+}'s yield and making this process feasible on larger scales. Many authors have suggested C_{2+} reactor yields, which are necessary to make the process competitive with the conventional technologies; that is why one of the focuses of the cases presented - including the base case - would be to highlight the ability of the membrane reactor to obtain a relatively higher C_{2+} yield. The selectivity and yield of C_{2+} are calculated using *Eqn. (3-42) and Eqn. (3-43),* respectively. The CO_x selectivity is calculated using *Eq(3-44).* The methane conversion needed to be calculated to obtain the selectivity and yield values, as shown in *Eq(3-40)*. Finally, the oxygen conversion was also essential to keep an eye on methane oxidation to ensure the optimum methane conversion level for the specific case is achieved. The oxygen conversion is calculated based on *Eq(3-41).*

Table 4-2: Species concentration in the feed and sweep channels (base case)

Concentration [mol/m^3]	**Inlet**	**Outlet**
$\dot{n}\ (H_2O)_{feed}$	32.07	31.39
$\dot{n}\ (H_2)_{feed}$	0	0.68
$\dot{n}\ (O_2)_{sweep}$	0	0.11
$\dot{n}\ (CH_4)_{sweep}$	28.06	27.50
$\dot{n}\ (C_2H_4)_{sweep}$	0	0.06
$\dot{n}\ (H_2O)_{sweep}$	0	0.37
$\dot{n}\ (C_2H_6)_{sweep}$	0	0.19
$\dot{n}\ (H_2)_{sweep}$	0	0.09
$\dot{n}\ (CO_2)_{sweep}$	0	0.02
$\dot{n}\ (CO)_{sweep}$	0	0.06

Table 4-3: Sweep side species conversion, selectivity, and yield values (base case)

Species	X_{O_2} **[%]**	X_{CH_4} **[%]**	**Selectivity [%]**	**Yield [%]**
O_2	66.96	-	-	-
CH_4	-	2.02	-	-
C_2H_4	-	-	20.72	0.42
C_2H_6	-	-	66.29	1.34
C_{2+}	-	-	87.01	1.76
CO_2	-	-	3.15	0.06
CO	-	-	9.85	0.20
CO_x	-	-	12.99	0.26

As shown in *Table* 4-2, The base case oxygen conversion is around 67 % due to increased porosity and the decrease in the catalyst mass per step, which directly reduces the oxygen consumption rate at every step and results in unconverted oxygen at a certain percent. The methane conversion shown in the same table relates to how much methane is converted to either C_{2+} or CO_x. Therefore, it is essential to achieve a higher methane conversion to achieve a higher C_{2+} yield, which will be investigated in a target case in *Section 4.4.*

Several aspects of the base case can be improved to achieve better C_{2+} yield, which depicts better membrane reactor performance. Systematic analysis and parametric study are used to analyze the base case in *Sections 4.3 and 4.4* to establish the correct relationships between the membrane reactor's parameters and performance. The molar flow rate of hydrogen on the feed and the sweep sides is shown in *Table 4-2.* Hydrogen is one of the two main outputs of this research due to its potential importance, as explained in *Chapter 1*. The rate at which hydrogen is produced on the sweep side can be related to the rate at which water is consumed; this shows the role of the oxygen permeable membrane in this catalytic membrane reactor. The mass flow rate lost on the feed side corresponds to oxygen permeating the membrane per second. On the other hand, the mass gained on the sweep side corresponds to the mass of oxygen that permeated through the membrane per second.

The mass balance is achieved by comparing the differences between the inlet and outlet mass flow rates in the feed and sweep sides, as shown in *Table 4-4*.

Table 4-4: Mass flow rates balance (base case**)**

Mass flow rate [g/s]	**Inlet**	**Outlet**	**Difference**
Total feed mass flow rate	5.80E-2	5.72E-2	7.90E-4
Total sweep inlet mass flow rate	5.69E-2	5.77E-2	7.90E-4

4.3 Systematic analysis

This section examines the design and operating parameters used to develop the base case scenario and establish the correct relationships between these parameters and the membrane reactor performance. It also attempts to attribute causes of specific noticeable trends in methane conversion, C_{2+} yield, selectivity, and CO_x selectivity. Systematic analysis is established to understand the effect of

altering several designs and operating parameters on achieving the best possible methane conversion and C_{2+} yield, which directly enhances the membrane reactor performance. In addition, a parametric study (sensitivity analysis) is established to know how target variables are affected based on changes in design, operating, and kinetics parameters. Lastly, applying the pressure drop on the membrane reactor is analyzed. Conclusions are drawn about the impact of the pressure drop on the membrane reactor performance. The conclusion drawn from this section is used to develop the target case scenario in *Section 4.6.*

4.3.1 Effect of reactor geometries on C_{2+} selectivity, yield, and methane conversion

4.3.1.1 Altering channel length

Channel length for both the feed and sweep channel were also altered to examine its effect on the C_{2+} selectivity, yield, and methane conversion. The systematic analysis included the base case scenario and four other cases where the channel length ranges between 1.1 to 1.9 m. It is essential to point out that the space-time was adjusted across the 5 cases to have a consistent volumetric flow rate for the 5 cases of around 7.23E-5 m^3/s.

Figure 4-1 (a) shows a relative percentage increase of 31.68 % in methane conversion between the base case and case 4 increased as the channel length manually increased to 1.9 m. The increase in channel length allows the species more volume to react. Specifically, the methane, which will have more volume to convert to C_{2+}, also explains the increase in the C_{2+} yield as the channel length increases. Increasing methane conversion is accompanied by a relative percentage increase in C_{2+} yield of around 27 % between the base case and case 4 and a relative percentage decrease in C_{2+} selectivity of around 3.26 % between the base case and case 4.

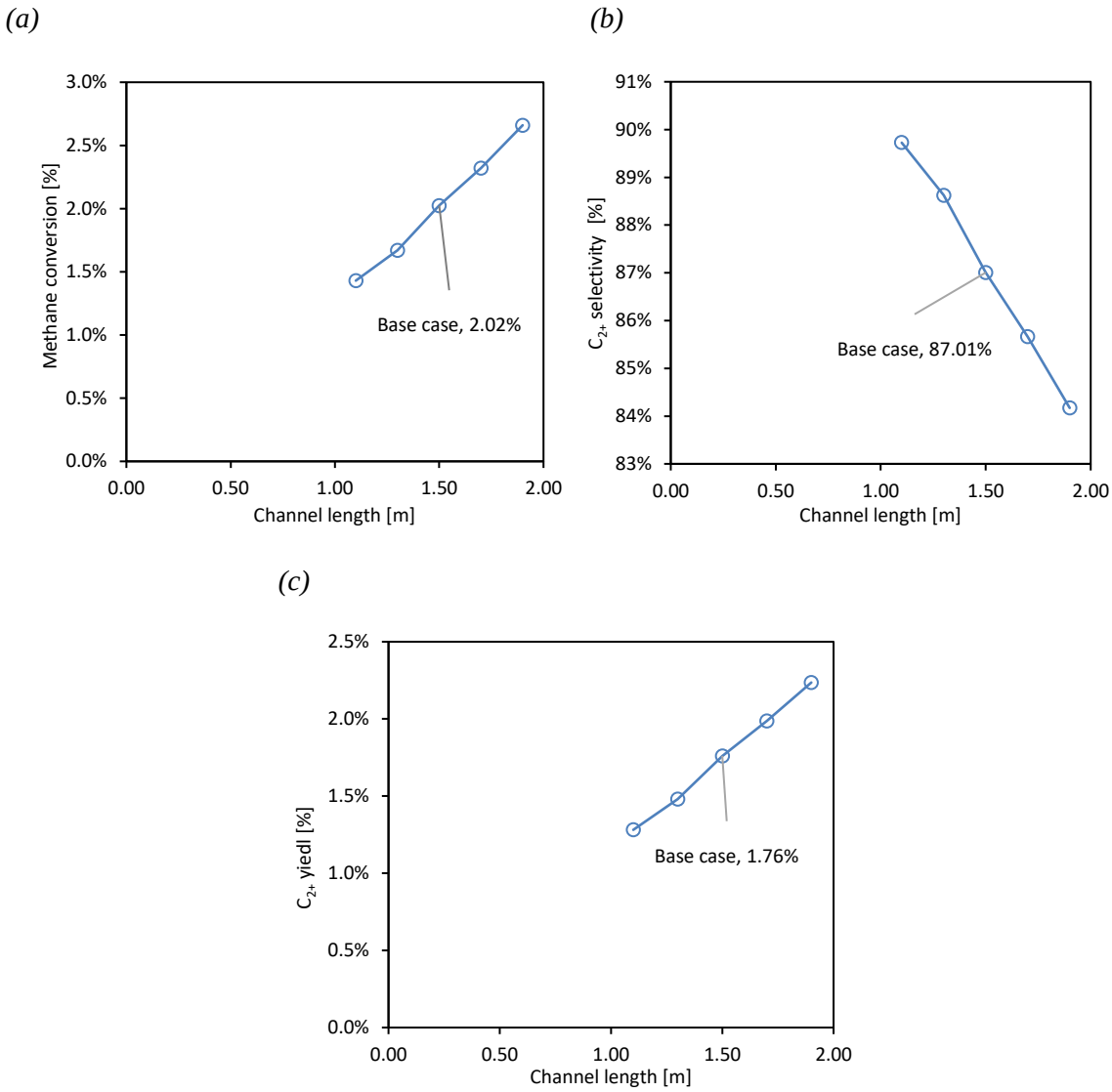

Figure 4-1: Effect of altering channel length on (a) methane conversion, (b) C_{2+} selectivity, and (c) yield (isothermal condition (T = 1103.3 K), pressure drop applied, base case reactor dimensions, Abs tolerance = 1E-14 and Rel tolerance = 1E-7)

4.3.1.2 Altering channel height

Channel height for both the feed and sweep channels was also altered to examine its effect on the C_{2+} selectivity, yield, and methane conversion. Similar to altering the other reactor dimensions, the systematic analysis included the base case scenario and four other cases where the channel height ranges

between 1E-4 to 1E-2 m. It is essential to point out that the space-time was adjusted across the 5 cases to have a consistent volumetric flow rate from the 5 cases of around 7.23E-5 m^3/s.

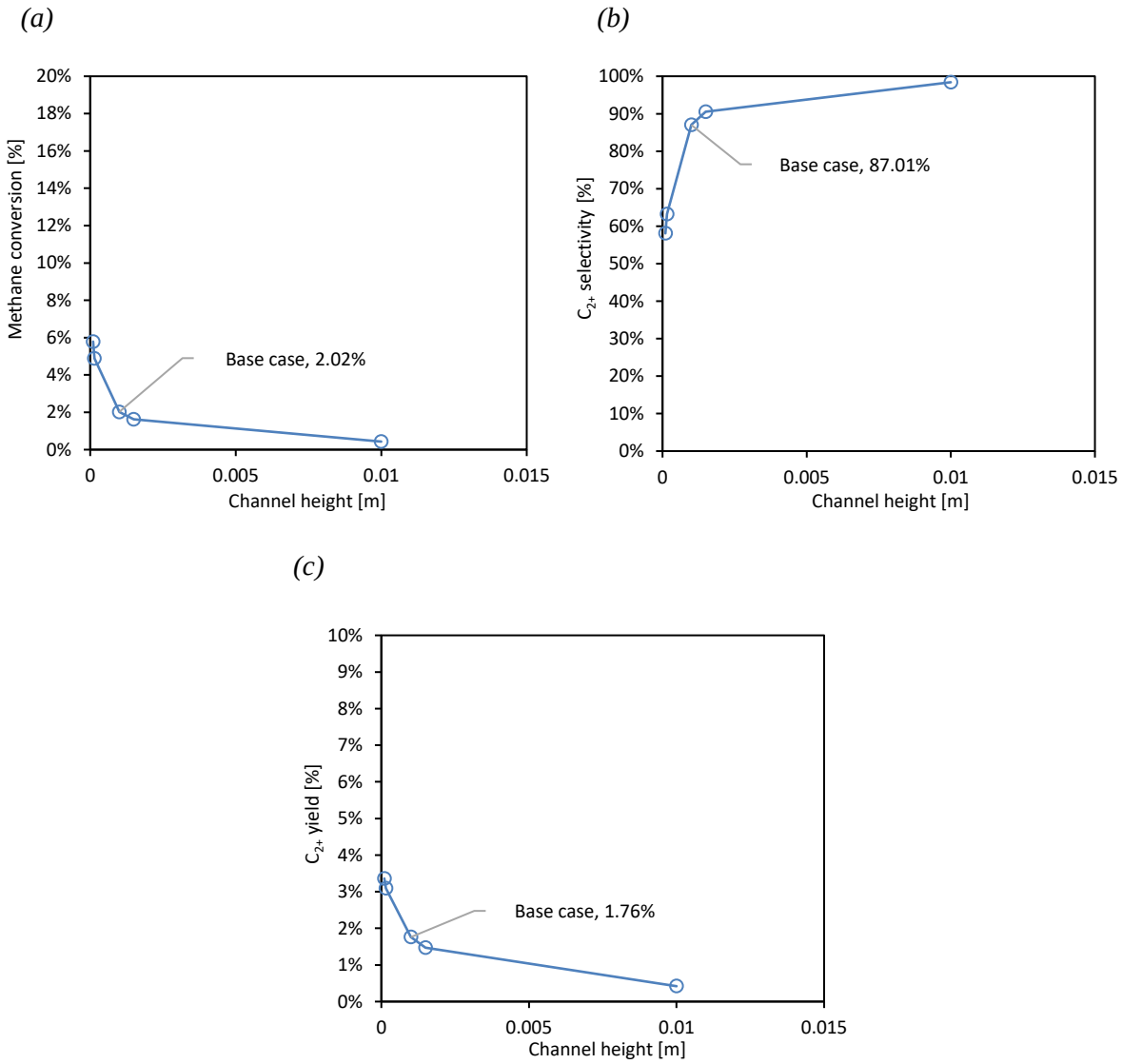

Figure 4-2: Effect of altering channel height on methane conversion, C_{2+} selectivity, and yield (isothermal condition (T = 1103.3 K), pressure drop applied, base case reactor dimensions, Abs tolerance = 1E-14 and Rel tolerance = 1E-7)

Figure 4-2 shows the positive impact of decreasing the channel height from 1E-3 to 1E-4 m on the methane conversion as it shows an absolute percentage increase of 3.76 % between the base case and

case 1. As expected, the increase in methane conversion is accompanied by an absolute percentage increase of 1.60 % in the C_{2+} yield between the base case and case 1 and an absolute percentage decrease of 28.92 % in the C_{2+} selectivity between the base case and case 1. Increasing the channel height leads to a drop in the mass transfer coefficient ($h_{m(j,i)}$). As a result, the difference between gas species in bulk and on the surface increases, which leads to a drop in oxygen flux. The decrease in the vacancy and oxygen fluxes can explain the decrease in methane conversion as the channel height increases. As the oxygen flux decreases, the amount of oxygen being permeated across the membrane also decreases, which means the methane oxidation rate decrease and allows less methane to convert into higher hydrocarbons.

4.3.2 Effect of operating parameters on C_{2+} selectivity, yield, and methane conversion

4.3.2.1 Altering Space-time

The space-time was varied between 5 different cases, including the base case. The order of magnitude for the space-time altered between the different cases. The lowest space-time investigated is 0.0186 kg s/m^3, and the highest space-time investigated is 186.79 kg s/m^3.

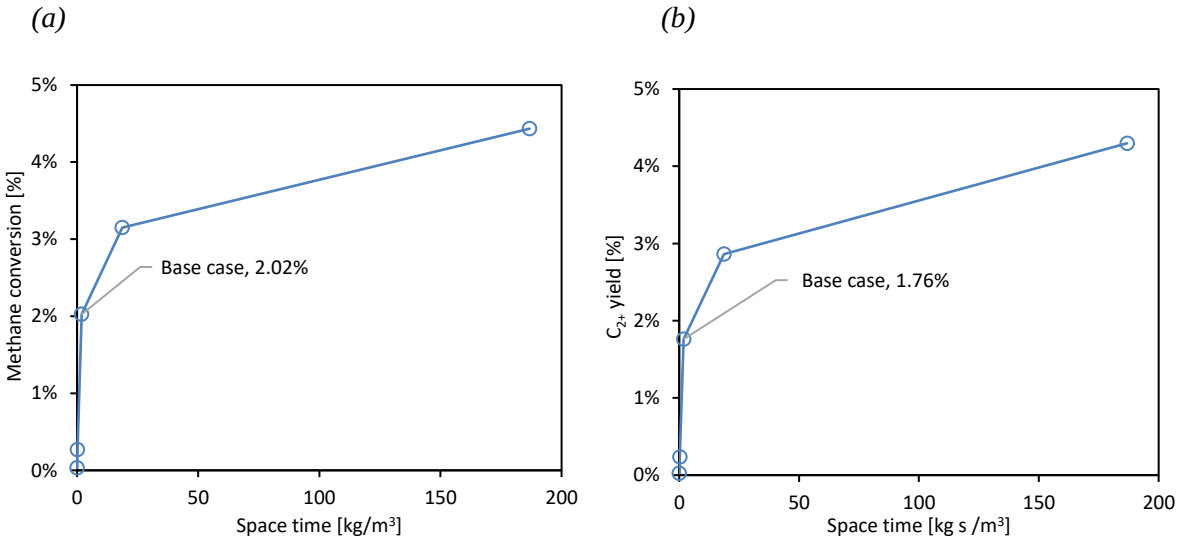

Figure 4-3: Effect of altering space-time on (a) methane conversion and (b) C_{2+} yield (isothermal condition (T = 1103.3 K), pressure drop applied, base case reactor dimensions, Abs tolerance = 1E-14 and Rel tolerance = 1E-7)

Figure 4-3 (a) and *(b)* show the methane conversion and C_{2+} yield trends as the space-time is increased between the cases. There is a clear increasing trend for methane conversion as space-time increases. The methane achieves its highest conversion of 4.43% in case 4, which correlates with the highest investigated space-time of 186.79 kg s/m^3 in the same case. The C_{2+} achieves its optimum yield of 4.30 % in case 4, which correlates with the highest investigated space-time of 186.79 kg s/m^3 in the same case. The positive trend showcased can be explained by the increase in space-time, representing the increase in the mean residence time. Increasing the mean residence time means increasing the time it takes for the number of species that takes up the control volume specified to either ultimately enter or completely exit the reactor. In other words, the species, primarily methane and oxygen, have more time to react and convert into C_{2+}, which is why an increase in the C_{2+} is noticeable.

4.3.2.2 Altering isothermal temperature

In this study, isothermal operating is assumed. However, it is critical to have adequate heat supply and thermal management in industrial applications to achieve the best performances. As shown in *Figure 4-4 (a)*, the methane conversion shows an absolute percentage increase of 3.19% between the base case and case 4 as the isothermal temperature increases from 1103.3 to 1203.3 K. Increasing the temperature affects the rate equations positively impacts the rate of methane consumption. At high temperatures, the C_{2+} selectivity drops, which may be attributed to the complete oxidation of ethane and ethylene to CO_2 and CO. Therefore, oxidative and non-oxidative dehydrogenation as well as deep oxidation of C_{2+} product to CO_x play an essential role in the OCM reaction network and should be considered in the kinetic modeling. The increase in the C_{2+} yield with temperature is also linked to the higher activation energies for the primary selective step, i.e., the formation of ethane from methane, compared to the one(s) of the nonselective primary step(s). This aspect is a common feature of the OCM reaction observed for various OCM catalysts.

As shown in *Figure 4-4 (c)*, it is also noticeable that the highest temperature examined of 1203.3 K correlates to the highest C_{2+} yield of 3.47 % for case 4. The increase in C_{2+} yield is expected due to increased methane conversion between the specified cases, following the already established direct relationship.

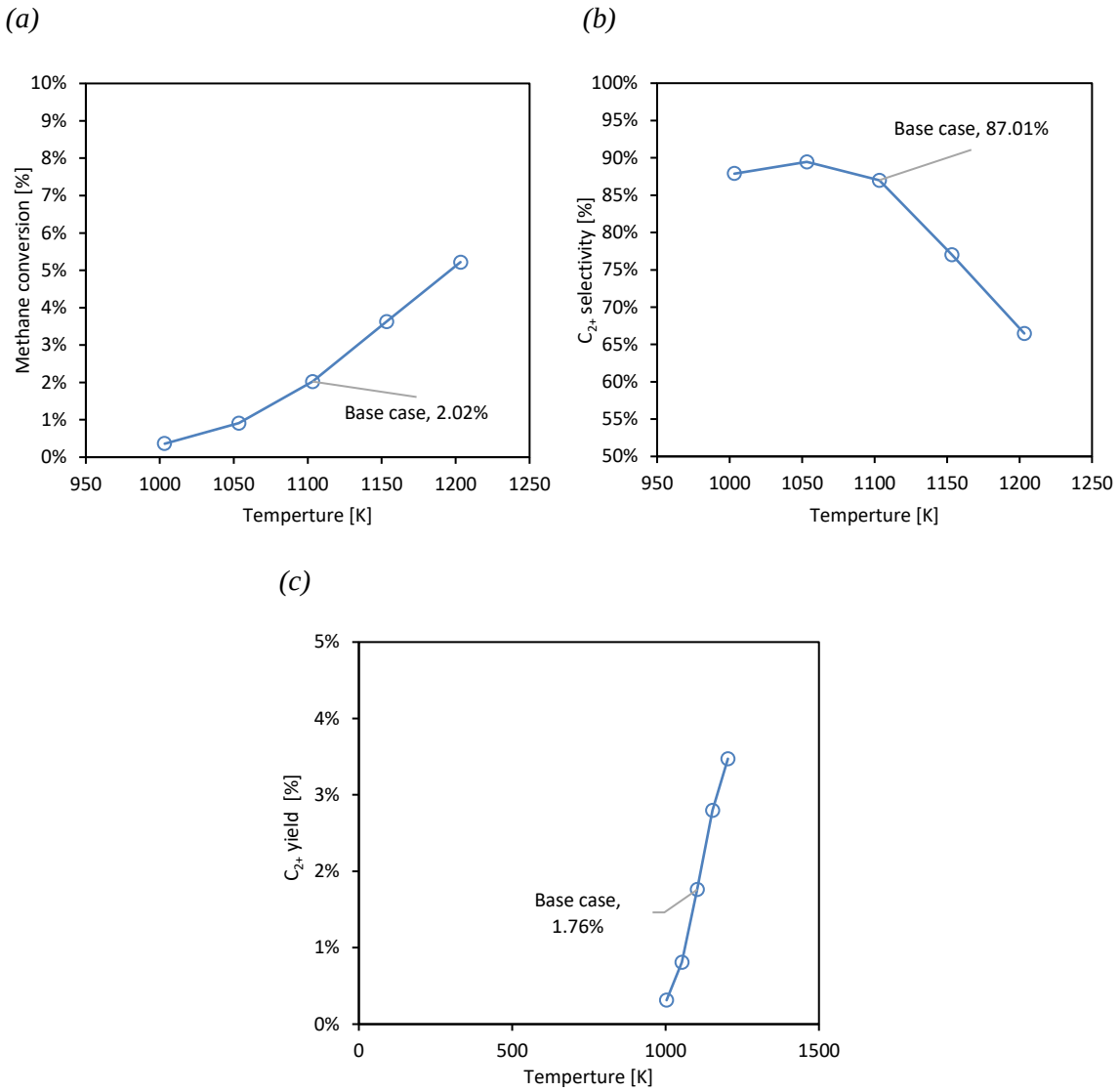

Figure 4-4: Effect of altering isothermal temperature on (a) methane conversion, (b) C_{2+} selectivity, and (c) yield (isothermal condition (T = 1103.3 K), pressure drop applied, base case reactor dimensions, Abs tolerance = 1E-14 and Rel tolerance = 1E-7)

4.3.2.3 Altering total catalyst mass per membrane surface area

Implementing an appropriate OCM catalyst with adequate intrinsic catalytic properties improves the surface kinetics and oxygen flux. The catalyst porosity directly impacts the total catalyst used in the sweep side, specifically the total catalyst mass per membrane surface area. Examining the total catalyst

mass per membrane surface area's effect on methane conversion, C_{2+} selectivity, and yield is essential. The total catalyst mass per membrane surface area was adjusted throughout five cases, including the base case. The total catalyst mass per membrane surface area was ranged between 3.2E-3 and 3.6E-4 [kg/m^2] between the 5 cases. The space-time was also adjusted across the five cases to have consistent volumetric flow rate and molar flow rates of methane and nitrogen at the channel inlet.

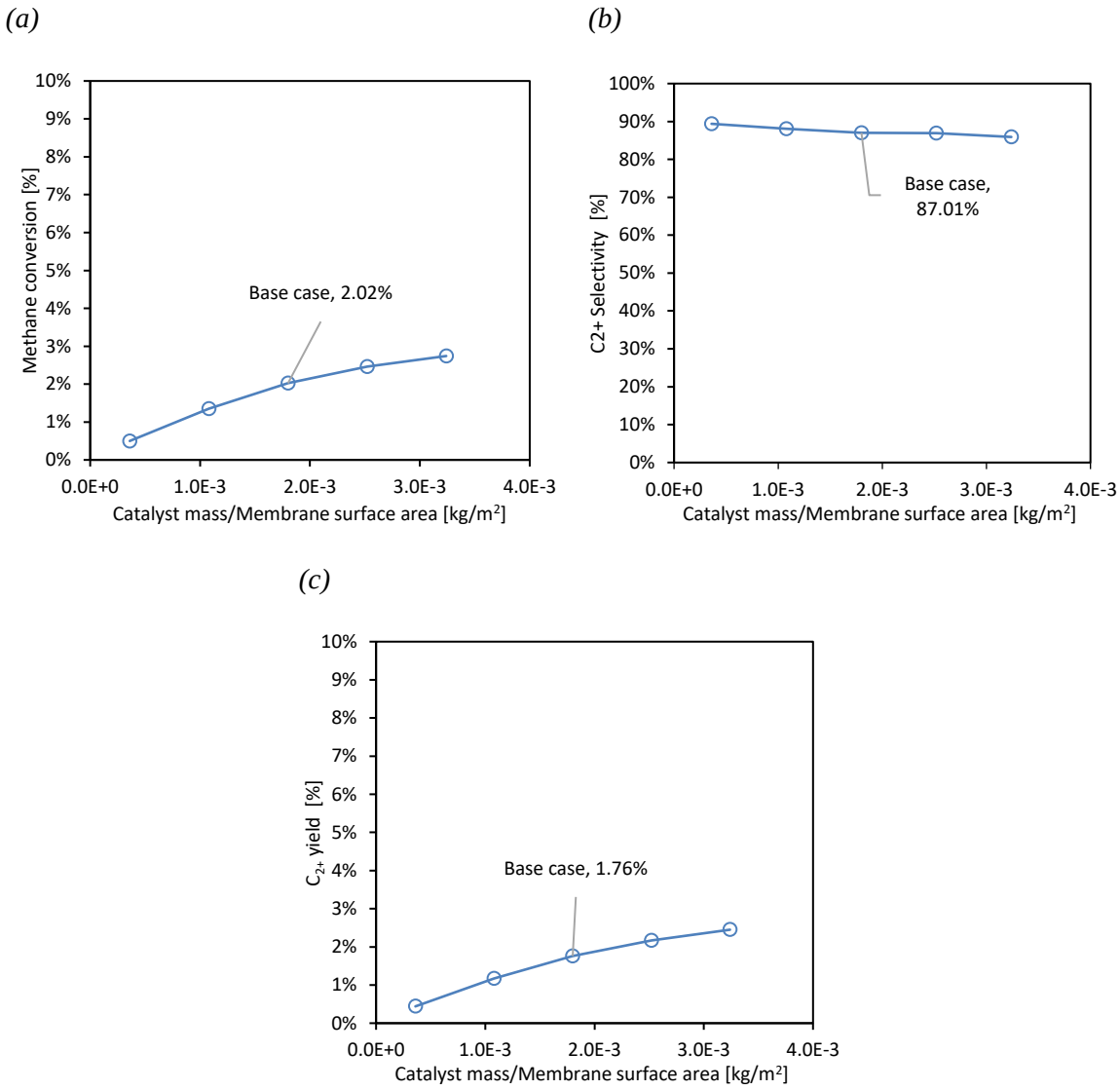

Figure 4-5: Effect of altering catalyst total mass per membrane surface area on (a) methane conversion, (b) C_{2+} selectivity, and (c) yield (isothermal condition (T = 1103.3 K), pressure drop applied, base case reactor dimensions, Abs tolerance = 1E-14 and Rel tolerance = 1E-7)

As shown in *Figure 4-5 (a)* and *(b)*, the increase in total catalyst mass per membrane surface area is accompanied by a decrease in methane conversion, reaching 0.50 % for case 4, followed by a decrease in C_{2+} yield due to the direct relationship between the two quantities reaching 0.44 % for case 4. The results also showed that the change in catalyst mass per Δx increases as the total catalyst mass per membrane surface area decreases, which means more catalyst is available at every iteration. Catalysts are used to decrease the activation energy and facilitate the reactions. Therefore, more catalyst mass per Δx can enhance fuel oxidation rates and increase methane conversion. This information can clarify the inverse relationship between methane conversion and total catalyst mass per membrane surface area.

4.3.3 Effect of pressure drop on reactor performance

The pressured drop in the axial direction is investigated by applying the Darcy friction factor equation as explained in *Chapter 3, Section 3.3.3.2*. Applying the pressure drop makes the one-dimensional membrane reactor model realistic and closer to reality. Usually, the pressure drop significantly impacts a plug flow reactor. The pressure drop can result in an expansion of the gas and increased volumetric flow rate with position down the reactor, leading to lower conversion rates. In order to examine the effect of pressure drop on the reactor performance, two scenarios for the base case were compared in which the pressure drop is enabled in one scenario. At the same time, the other has a negligible pressure drop in the axial direction.

Table 4-5 : Comparison between scenario 1 (pressure drop neglected) vs. scenario 2 (pressure drop considered)

Scenario	**Scenario 1 (pressure drop neglected)**	**Scenario 2 (pressure drop considered)**
Conversion	**Value [%]**	**Value [%]**
O_2	67.02	66.96
CH_4	2.02	2.02
Selectivity	**Value [%]**	**Value [%]**
C_{2+}	87.06	87.01
CO_x	12.99	12.99

Yield	Value [%]	Value [%]
C_{2+}	1.76	1.76
CO_x	0.26	0.26

Table 4-5 shows that implementing the pressure drop in scenario 2 resulted in a slight decrease in the oxygen conversion of around 5.99E-2 % and a slight decrease in methane conversion and C_{2+} yield of around 1.6E-3 and 1.3E-3 %, respectively.

The pressure drop tends to affect small diameter reactors like the reactor modeled in this research, which increases the volumetric flow rate, reduces residence time, and lowers conversion. The percentage difference between the two scenarios can be used to presume that the pressure drop does not impact the reactor performance; this can be explained due to the high catalyst porosity used, which resembles a low total catalyst mass of around 1.34E-3 kg. Porosity irrefutably has excellent importance in pressure drop calculations. The higher the porosity is, the more accessible the fluid to penetrate the bed, and as a result, the less impactful the pressure drop will be on the reactor performance, which is the case presented in this section.

4.4 Sensitivity analysis

A sensitivity analysis is performed to evaluate the dependence of the design metrics on different parameters. The sensitivity of the C_{2+} yield and CH_4 conversion were examined concerning several parameters, seeing as these two metrics are the main criteria that are used to evaluate the performance of the current membrane reactor model. The parameters are grouped into the design, operation, and kinetics parameters. The sensitivity is calculated over an extensive range of percent changes and averaged relative to the base case scenario.

$$S_{a-b} = \frac{\text{Relative change of a}}{\text{Relative change of b}} = \frac{a}{b}\frac{\Delta b}{\Delta a} = \frac{\Delta b / b}{\Delta a / a} \tag{4-5}$$

Where,

- a: parameter for which the sensitivity is calculated
- b: the metric for which the sensitivity is calculated

4.4.1 Design parameters

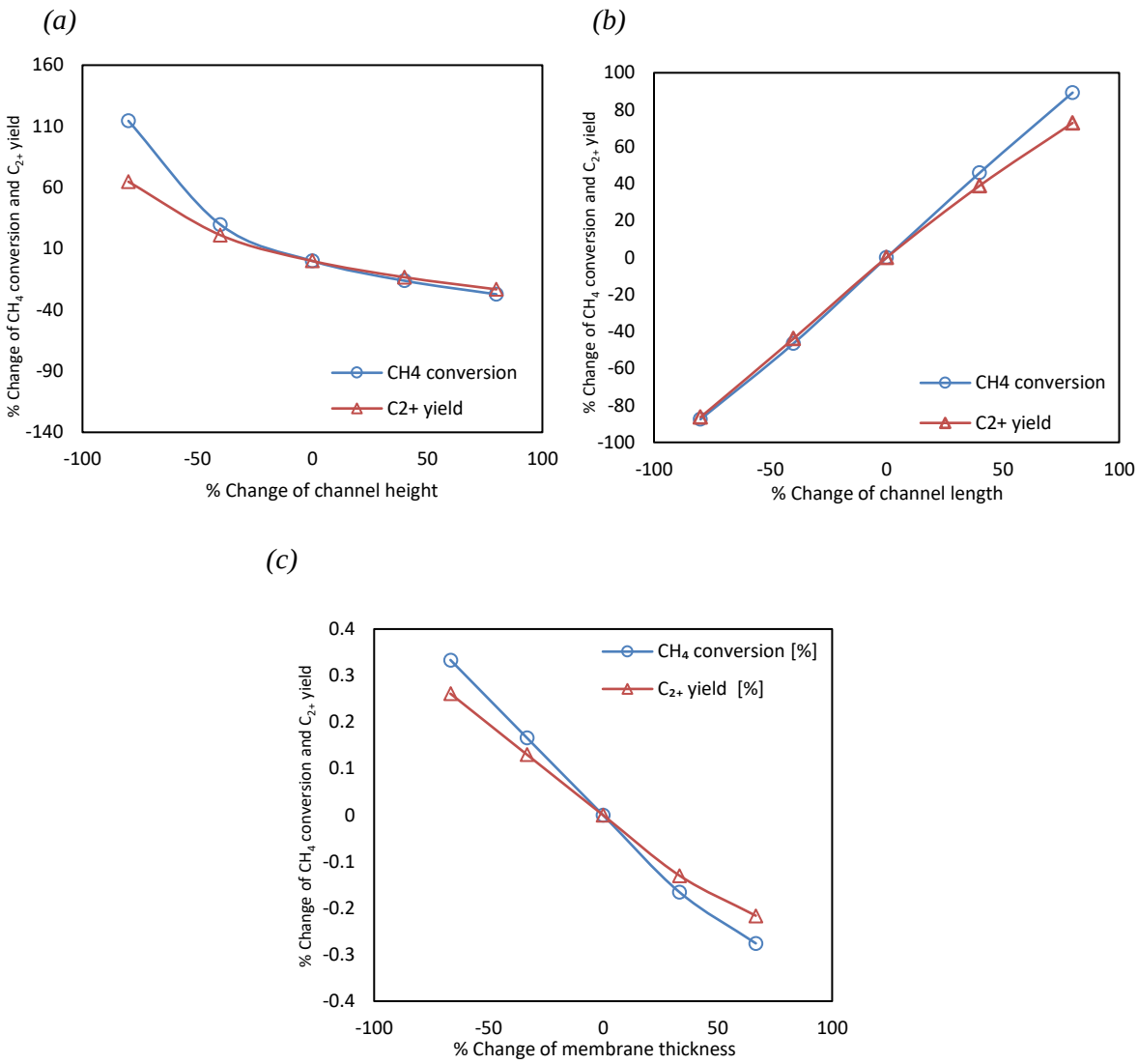

Figure 4-6: Percentage change of (a) channel height, (b) channel length, and (c) membrane thickness vs percentage change of CH_4 conversion and C_{2+} yield

Table 4-6 shows the sensitivity analysis results concerning the design parameters. The averaged sensitivity results show that the membrane reactor is sensitive to channel length. The increase in channel length leads to methane having more volume to convert to C_{2+}, and this also explains the increase in the C_{2+} yield as the channel length increases.

Figure 4-6 (a) shows that increasing the channel height leads to a drop in the mass transfer coefficient ($h_{m(j,i)}$). As a result, the difference between the gas species in bulk and on the surface increases, which leads to a drop in the oxygen flux and ultimately the methane conversion and the C_{2+} yield.

Figure 4-6 (c) shows an inverse relationship between the membrane thickness and the C_{2+} yield and methane conversion. Decreasing the thickness of the membrane leads to an increase in the vacancy and oxygen flux; this means that thinner membranes are required to enhance the C_{2+} yield and the overall membrane reactor performance. *Table* 4-6 shows low sensitivity when varying the membrane thickness. The low sensitivity might be related to the fact that the bulk diffusion across the membrane is not the limiting step, which makes the effect of varying membrane thickness not obvious.

Table 4-6: Sensitivity analysis results for design parameters

Parameter	**Base value**	$S_{X(CH_4)}$	$S_{C_{2+}yield}$
Channel height [m]	1E-3	-0.729	-0.49
Channel length [m]	1.5	1.13	1.01
Membrane thickness [m]	9E-4	-0.0047	-0.0043

4.4.2 Operation parameters

(a)

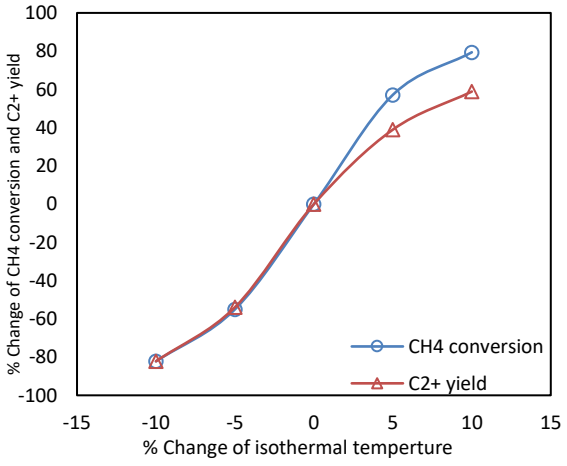

(b)

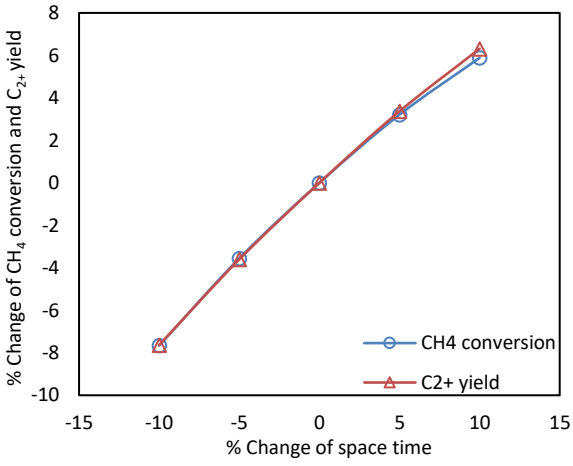

(c)

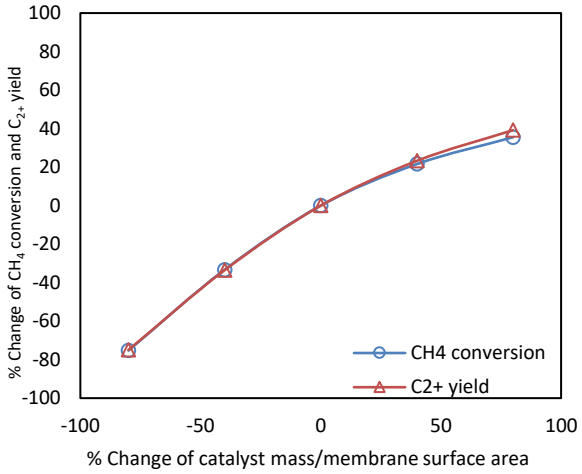

Figure 4-7 : Percentage change of operation parameters vs percentage change of CH_4 conversion and C_{2+} yield

Table 4-7 summarizes the sensitivity analysis results for the operation parameters, namely isothermal temperature, space-time, and catalyst mass per membrane surface area. The averaged sensitivity results show that the membrane reactor is most sensitive to the operating temperature.

As shown in *Figure 4-7 (a)*, the averaged sensitivity results show that the isothermal temperature is the second most impactful operation parameter on the membrane performance. This study assumes the isothermal condition along the feed channel, sweep channel, and membrane. Nevertheless, the overall reaction in the membrane reactor is endothermic. It is critical to have adequate heat supply and thermal management in industrial applications to achieve the best performances. Higher operating temperature leads to faster surface kinetics, and therefore, methane is consumed faster with the increase of oxygen flux. A 10 % increase in the isothermal temperature led to a 79 % increase in the methane conversion and a 58 % increase in the C_{2+} yield.

As shown in *Figure 4-7 (b)*, altering the space-time is not as impactful to the membrane reactor performance as the isothermal temperature. Increasing the space-time means increasing the time for the number of species that take up the specified control volume to enter or completely exit the reactor. In other words, the species, primarily methane and oxygen, have more time to react and convert into C_{2+},

which is why an increase in the methane conversion and C_{2+} yield is noticeable. A 10 % increase in space time leads to only a 5.88 % increase in methane conversion and a 6.31 % increase in the C_{2+} yield.

Figure 4-7 (c) depicts the direct relationship between the total catalyst mass per membrane surface area and the membrane reactor performance parameters (methane conversion and the C_{2+} yield). A 40 % increase in the total catalyst mass per membrane surface area results in a 35.50 % increase in the methane conversion and a 39.20 % increase in the C_{2+} yield. The increase in the total catalyst mass per membrane surface area increases the catalyst mass at every iteration (established in *Section 4.3.2.3*), which enhances the surface kinetics and increases the methane conversion and C_{2+} yield.

Table 4-7: Sensitivity analysis results for operating parameters

Parameter	Base value	$S_{X(CH_4)}$	$S_{C_{2+}yield}$
Space time [kg s/m^3]	1.87	0.68	0.7
Isothermal temperature [K]	1103.3	9.65	8.17
Catalyst mass per membrane surface area [kg/m^2]	1.8E-3	6.89E-1	7.12E-1

4.4.3 Kinetics parameters

(a)

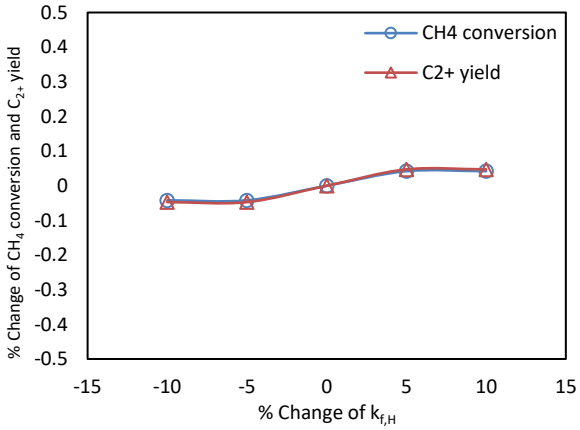

(b)

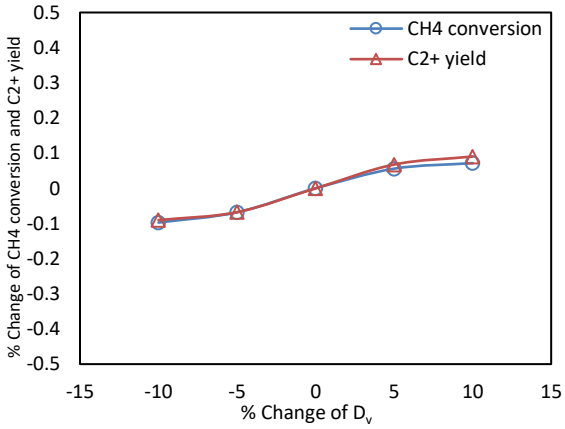

(c)

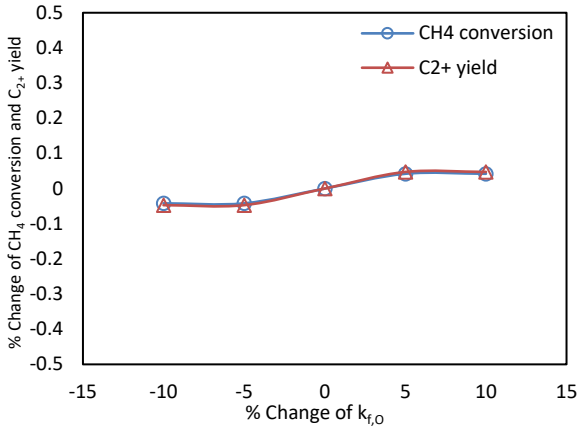

Figure 4-8: Percentage change of (a) forward water splitting rate (b) oxygen vacancy diffusivity (D_v) (c) forward oxygen incorporation rate vs percentage change of CH_4 conversion and C_{2+} yield

Table 4-8 shows the sensitivity of the membrane reactor to the kinetic parameters. The kinetics parameters were varied between ± 10 % by altering the pre-exponential factor. The averaged sensitivity results show presented kinetic parameters have a minor impact on that membrane reactor performance compared to the other parameters showcased in the sections above. Improving these two kinetic parameters will result in a minimal increase in the C_{2+} yield and methane conversion.

Figure 4-8 *(a)* shows that increasing the rate of vacancy diffusivity increases the methane conversion and C_{2+} yield. Increasing the rate of vacancy diffusivity leads to a decrease in bulk resistance (R_b). The decrease in bulk resistance (R_b) increases the oxygen flux and the vacancy flux (based on *Eqn. (3-14)*), which increases the methane conversion and C_{2+} yield because of the rate at which oxygen is being permeated to the sweep side increases.

Figure 4-8 (b) shows that increasing the forward water splitting rate increases the methane conversion and C_{2+} yield. Increasing the water splitting rate leads to a decreased surface reaction resistance on the feed side (R_f). The decrease in the surface reaction resistance on the feed side increases the oxygen flux and the vacancy flux based on the inverse relationship between them (*Eqn. (3-14)*). The methane conversion and C_{2+} yield increase because oxygen permeating the sweep side increases.

Figure 4-8 (c) shows that increasing the forward oxygen incorporation rate increases the methane conversion and C_{2+} yield. Increasing the forward rate of oxygen incorporation will increase the rate at which the oxygen lattice can react with the electron-hole to leave the surface of the membrane and

transform to gas-phase oxygen, as shown in *Eq. (2-11)*. The aforementioned means that more oxygen will be available on the sweep side, enhancing the methane conversion and the C_{2+} yield. The membrane reactor seems to be equally sensitive to the forward water splitting rate and the forward rate of oxygen incorporation, as shown in *Table* 4-8. The aforementioned suggests that the water-splitting rate is equal to the rate of formation of the oxygen molecule, as established in *Section 3.3.1*.

Table 4-8: Sensitivity analysis results for kinetic parameters

Parameter	**Base value**	$S_{X(CH_4)}$	$S_{C_{2+}yield}$
D_v [m^2 / s]	7.51E-10	1.04E-2	1.13E-2
$k_{f,H}$ [m^4/mol s]	8.18E-7	6.31E-3	7.08E-3
$k_{f,O}$ [$m^{2.5}$/$mol^{0.5}$ s]	1.78E-5	6.31E-3	7.08E-3

4.5 Economic feasibility of the OCM technology for the co-production of ethylene and hydrogen

This section attempts to estimate the profitability of integrating the OCM process in a membrane reactor based on the total operating and utility costs of C_2H_4 production. The estimation of the total operating expenses of C_2H_4 production can help set a criterion for the target case developed later in this chapter. Although the section does not cover all financial matters, it is a good indicator for choosing among alternatives and finding out which part of the process should be improved. The focus is on the utility and operating costs of significant steps in simplifying the OCM process. Some costs and technical requirements were excluded, such as initial capital costs and energy requirements. That is why this is not a full techno-economic assessment of the OCM process, as it is out of the scope of this thesis. Cruellas et al. [59] provided a more comprehensive economic evaluation.

Cruellas et al. [59] have quantified the performance of the OCM reactor from a techno-economic point of view. To do so, the group developed a one-dimensional membrane reactor model. The catalyst used is La_2O_3/CaO catalyst, and its kinetics are based on the data provided by Stansch et al. [91]. Several assumptions were implemented in which the system is assumed to be kinetic limited; that is, it has been assumed that there are no mass and heat transfer limitations. Also, an isothermal temperature condition was assumed in the membrane reactor. It is also important to note that in the model developed, the

reaction rates of the primary OCM reactions (according to the kinetics provided by Stansch et al. [91] have been manually modified to increase the CH_4 conversion and the C_{2+} selectivity as a way to stimulate improvements in the reaction path. The best C_{2+} yield obtained is 15.5 %, corresponding to a CH_4 conversion of 51.1 % and a C_{2+} selectivity of 30.3 %. This maximum yield is reached at 860 °C with a CH_4 /O_2 ratio of 1.5.

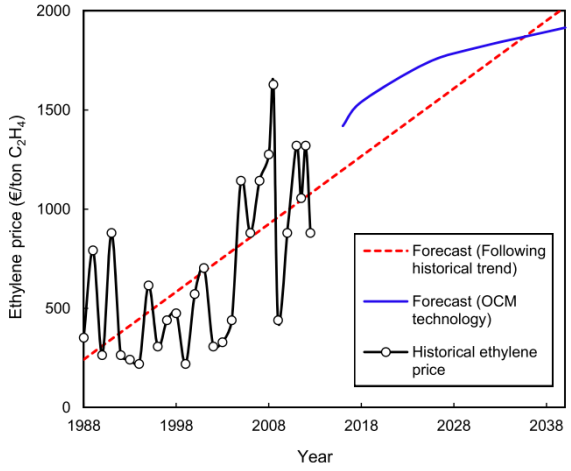

Figure 4-9: Historical ethylene price (black), ethylene price forecast based on historical data (red), and ethylene price forecast using OCM (blue) for the coming period. [59]

Figure 4-9 shows the forecast of natural gas and naphtha costs presented. The gap between the ethylene price obtained with conventional technologies and the one obtained with the current OCM achievable yield (C_{2+} yield = 14 %) is expected to progressively become smaller, forecasting OCM to be competitive with traditional technologies in around 20 years. On the other hand, the study concluded that a C_{2+} reactor yield of at least 25–30 % is the target needed to obtain an ethylene cost lower than 1000 €/ton C_2H_4 (1187.84 US $/ton C_2H_4).

4.5.1 Ethylene price estimation

The estimation of the ethylene price is based on the economic model developed by Nghiem [15]. Several assumptions were made by the model, which affect the cost estimation directly:

- OCM process (occurring on the sweep side) is summarised in 4 steps, reaction, compression, carbon dioxide removal, and ethylene separation, as shown in *Figure 4-10.*

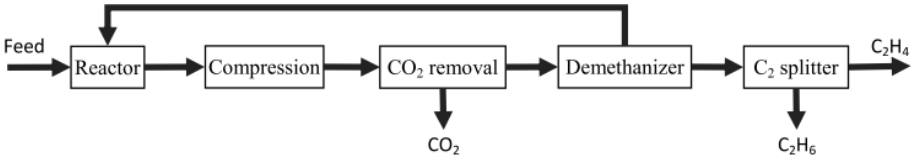

Figure 4-10: Summarized OCM process stages in the sweep side

- Carbon dioxide removal and ethylene separation utilize typical absorption and cryogenic distillation technology.
- Assuming that only two reactions occur, a direct OCM reaction from methane to ethylene is assumed, and the combustion of methane to carbon dioxide methane, as shown in *Eqn. (4-6)* and *Eqn.* (4-7), respectively.

$$2CH_4 + O_2 \rightarrow C_2H_4 + 2H_2O \tag{4-6}$$

$$CH_4 + 2O_2 \rightarrow CO_2 + 2H_2O \tag{4-7}$$

- In most reported experiments, oxygen conversion reacts completely: oxygen conversion is between 90% and 100%. This assumption, therefore, makes calculation simpler without losing much accuracy.
- Water is entirely condensed after the reactor: desiccation before cryogenic distillation is required, but its cost is not accounted for here.
- No heat integration between sections: This is certainly untrue in commercial plans. However, it separates sections and gives a clearer view of the cost structure.
- For this current research, integrating OCM into membrane-supported water-splitting technology can utilize the oxygen from water splitting to co-produce higher value products (e.g., ethylene). This initiation can help eliminate the Air Separation Unit (ASU) and avoid paying for inlet oxygen.
- The hydrogen price was not accounted for in the final ethylene price for this price estimation. Hydrogen is also one of the essential products considered for industrial use. Selling pure hydrogen

as a by-product can reduce the target price/ton needed to make the OCM produced ethylene industrially applicably. According to market sources [121], green hydrogen produced with renewable resources costs between about $3/kg ($3000/ton) and $6.55/kg ($6550/ton). Fossil-based hydrogen costs about $1.80/kg ($1800/ton).

4.5.2 Utility costs estimation

Utility costs are calculated according to *Eqn. (4-8)*, developed by Ulrich et al. [122]. Natural gas is chosen as fuel with an estimated price of $160.29/ton [15]. The water prices are estimated based on water rates in Toronto, Canada [123]. The catalyst and membrane costing have been taken from e-commerce websites, i.e., Alibaba [124–127].

$$C_{utility} = a(\text{CE PCI}) + b(C_{fuel}) \tag{4-8}$$

Where,

- $C_{utility}$: the price of the utility, [$]
- C_{fuel}: the price of fuel, [$/GJ]
- CE PCI: plant cost dimensionless index [128]
- a and b: coefficients whose units depend on utility type.

4.5.2.1 Feed side utility costs

Table 4-9: Feed side utility costs

Utility	Total cost
Inlet water	$51.65/ton
Electricity	$0.104/kWh

(1) Inlet water

Assuming 1 ton of water (1018.32 liters) is used as an inlet, the inlet water is the only oxygen source in the membrane reactor model. It is injected into the reactor by an inert gas carrier. Therefore, the oxygen incorporation/dissociation reaction or the forward/reverse water thermolysis reaction occurs.

(2) Electricity

For electricity, a = 1.3E-4 and b = 0.01. Electricity price calculated by *Eqn.(4-8)* is $0.104/kWh.

4.5.2.2 Sweep side utility costs

Table 4-10: Sweep side utility costs

Utility	Total price
Catalyst	$2.01/kg
Membrane	$0.46/kg
Electricity	$0.104/kWh
Methane	$160.29/ton
Refrigerant	$43.51/GJ

(1) Catalyst

La_2O_3/CaO catalyst pricing was estimated by collecting data from online vendors. La_2O_3 powder was found on Alibaba [129]. The cost of purified CaO is taken from the same source [129]. *Table B - 1* shows the estimated total cost of the catalyst.

(2) Membrane

In order to estimate the total cost of the membrane (shown in *Table B - 2)*, the average cost of all the salts needed to synthesize 1 kg of the membrane in $/kg is collected from online vendors. The amount to synthesize per kg of perovskite and the total weight of membrane needed are based on the membrane designed by Wu et al. [37]. The actual cost of salt is calculated as the product of the average cost and the amount required to synthesize 1 kg of perovskite. Lastly, the total cost is calculated using *Eqn.* (4-9).

$$C_{membrane} = C_{salts} \times W_{membrane} \times A_{s,membrane} \quad (4\text{-}9)$$

Where,

- $C_{membrane}$: total cost of the membrane, [$]
- C_{salts} : actual cost of salts, [$]
- $W_{membrane}$: total weight of membrane needed, [kg/m^2]
- $A_{s,membrane}$: total surface area of the membrane, [m^2]

(3) Electricity

Similar to estimation on the feed side.

(4) Methane

Natural gas is chosen as fuel with an estimated price of $160.29/ton [15].

(5) Refrigerant

The total price is estimated using *Eqn.* (4-8). $A = 0.6Q^{-0.9} T^3$ and $b = 1.1x10^6T^5$ with Q is cooling capacity in kJ/s (maximum 1000), and T is the absolute temperature. Q is chosen as 1000 concerning the scale of the OCM plant based on the Nghiem [15] model.

4.5.3 Operating costs estimation

Based on the simplified OCM process shown in *Figure 4-10* and the assumption that only two reactions occur, a direct OCM reaction from methane to ethylene is assumed, and methane to carbon dioxide is the combustion, as shown in *Eqn. (4-6)* and *Eqn.* (4-7). The operating costs include reactions, compression, carbon dioxide removal, ethylene separation, and ethane production. *Table 4-11* shows the summary of the operating costs calculations. The amount needed for every item is calculated based on the inlet and outlet composition shown in *Table B - 3.*

Table 4-11: Operating costs summary

Item	Price	Amount	Total cost in terms of ethylene [$]
Reactions			
Methane	$160.29/t [15]	$\frac{8}{7S_{C_2H_4}}$	$\frac{183}{S_{C_2H_4}}$
Compression	$0.009/Nm^3 [15]	$22.4\frac{2-Y_{C_2H_4}}{Y_{C_2H_4}}$	$\frac{14.4}{Y_{C_2H_4}}-7.2$
Carbon dioxide removal			
Pump	$1.3/t [15]	$\frac{22-22S_{C_2H_4}}{7S_{C_2H_4}}$	$\frac{4.09}{S_{C_2H_4}}-4.09$
Caustic wash	$6.49/t [15]	$\frac{0.16-0.16X_{C_2H_4}+0.08Y_{C_2H_4}}{Y_{C_2H_4}}$	$\frac{1.04}{Y_{C_2H_4}}-\frac{1.04}{S_{C_2H_4}}+0.52$
Ethylene separation			
Refrigerant	$43.5/GJ [15]	$\frac{4.8-4.8X_{C_2H_4}}{7Y_{C_2H_4}}$	$\frac{30}{Y_{C_2H_4}}-\frac{30}{S_{C_2H_4}}$

(1) Reaction costs

According to estimation by Nghiem [15], assuming that only two reactions take place in the reactor and oxygen reacts fully, 1 mol of methane fed in the reactor will produce $\frac{Y_{C_2H_4}}{2}$ mol of ethylene and $X_{CH_4} - Y_{C_2H_4}$ mol of carbon dioxide, while 1-X_{CH_4} mol of methane remains unconverted. 1 mol of oxygen is consumed to produce 1 mol of ethylene. 2 mol of oxygen is consumed to produce 1 mol of carbon dioxide. Assuming total oxygen conversion, $2X_{CH_4}$-$1.5Y_{C_2H_4}$ mol of oxygen must be available along with 1 mol of methane to produce $\frac{Y_{C_2H_4}}{2}$ mol of ethylene and $X_{CH_4} - Y_{C_2H_4}$ mol of carbon dioxide.

As shown in *Table B - 3*, on a weight basis $\frac{8}{7S_{C_2H_4}}$ tonnes of methane is consumed to produce 1 tonne of ethylene; therefore, the operating costs for methane are shown in *Eqn.* (4-10), assuming complete water removal, inlet and outlet compositions, and excluding the reactants' heating and cooling process.

$$C_{methane} = \frac{183}{S_{C_2H_4}} \tag{4-10}$$

Where,

- $C_{reaction}$: operating costs of reactions, [$]

Most OCM experiments were conducted at atmospheric pressure. Cryogenic demethanizer operate between 10 and 30 bar [130], with higher pressure means more compressing cost. The total cost for compression needed to produce 1 tonne of C_2H_4 is estimated using *Eqn.* (4-11). According to estimation by Nghiem [15] and as shown in *Table B - 3,* the total flow rate per ethylene flow rate is $\frac{2-Y_{C_2H_4}}{Y_{C_2H_4}}$mol/mol at reactor outlet. This means production of 1 kmol of ethylene requires compression of $\frac{2-Y_{C_2H_4}}{Y_{C_2H_4}}$ kmol gases, which is equivalent to $22.4\frac{2-Y_{C_2H_4}}{Y_{C_2H_4}}$ Nm^3.

$$C_{compression} = \frac{14.4}{Y_{C_2H_4}} - 7.2 \tag{4-11}$$

Where,

- $C_{compression}$: operating costs of the compression process, [$]

(2) Carbon dioxide removal

According to estimation by Nghiem (shown in *Table B - 3)* [15], $\frac{22-22S_{C_2H_4}}{7S_{C_2H_4}}$ tonnes of carbon dioxide are coproduced along with 1 tonne of ethylene. carbon dioxide is removed from the reaction product by regenerative solvent (alkanolamines) and once-through (caustic wash) scrubbing. Operating alkanolamines absorption system requires steam, make-up water and electricity, which is not accounted for in this estimation. It is impossible with alkanolamines alone to lower the concentration of carbon dioxide to ppm level, which is required for the cryogenic process. A fine purification consisting of a caustic wash unit is needed to reach the required carbon dioxide specification. Based on Nghiem estimation [15], in the feed stream of caustic wash, one kmol of ethylene is accompanied by $\frac{2-2X}{Y}$ kmol of methane The standard volume is then $\frac{44.8-44.8X_{C_2H_4}+22.4Y_{C_2H_4}}{Y_{C_2H_4}}$ Nm^3 per kmol ethylene, which is equivalent to $\frac{1.6-1.6X_{C_2H_4}+0.8Y_{C_2H_4}}{Y_{C_2H_4}}$ Nm^3 per tonne ethylene. Since each 1 Nm^3 needs about 0.1 g caustic soda, caustic soda consumption is $\frac{0.16-0.16X_{C_2H_4}+0.08Y_{C_2H_4}}{Y_{C_2H_4}}$ kg/tonnes ethylene production. The operating cost estimation for CO_2 removal (shown in *Eqn. (4-12))* considers the pumping cost per tonne of carbon dioxide and the caustic wash unit.

$$C_{CO_2,removal} = \frac{1.04}{Y_{C_2H_4}} + \frac{3.05}{S_{C_2H_4}} - 3.57 \tag{4-12}$$

Where,

- $C_{CO_2,removal}$: operating costs of the CO_2 removal process, [$]

(3) Ethylene separation

Cryogenic distillation for ethylene separation requires refrigerant for the condenser, while a reboiler is usually coupled with a gas cooler. A distillation design can estimate utility requirements based on desired ethylene purity and recovery. The total refrigerant price in terms of ethylene is estimated using *Eqn. (4-13)*, based on the estimation by Nghiem [15] that 1 tonne of ethylene must be separated from $\frac{8-X_{CH_4}}{7Y_{C_2H_4}}$ tonnes of methane (as shown in *Table B - 3).*

$$C_{C_2H_4,seperation} = \frac{30}{Y_{C_2H_4}} - \frac{30}{S_{C_2H_4}} \quad (4\text{-}13)$$

Where,

- $C_{C_2H_4,seperation}$: operating costs of ethylene separation, [$]

(4) Ethane production

The formation of ethane reduces compression and carbon dioxide removal costs because volumetric flow rate and carbon dioxide are reduced, but the cost of C_{2+} fractionation is added (estimated to be $80\frac{S_{C_2H_6}}{S_{C_2H_4}}$ by Nghiem [15]). Ethane and ethylene have similar properties and can be considered the same in carbon dioxide absorption and demethanizer sections. Therefore, operating cost per unit C_{2+} can be obtained by replacing $S_{C_2H_4}$ and $Y_{C_2H_4}$ by $S_{C_{2+}}$ and $Y_{C_{2+}}$.As operating pressure and temperature are fixed, a simple equation for estimating the total ethylene price based on the above can be drawn (shown in *Eqn. (4-14)*). The equation also considers the formation of ethane, as discussed in the previous section.

$$C_{ethylene} = \frac{45.44}{Y_{C_{2+}}} + \frac{156.05}{S_{C_{2+}}} - 10.77\frac{S_{C_{2+}}}{S_{C_2H_4}} + 80\frac{S_{C_2H_6}}{S_{C_2H_4}} \quad (4\text{-}14)$$

Where,

- $C_{ethylene}$: total ethylene price, [$]

4.5.4 Total ethylene price estimation and the required C_{2+} yield

The total C_2H_4 price is estimated based on the utilities and operating costs. Based on the cost estimation, the operating cost depends primarily on yield and selectivity. Based on the *Eqn.* (4-14) and using the base case results of 87.01 % of C_{2+} selectivity, 1.76 % of C_{2+} yield, 20.72 % of C_2H_4 selectivity, and 66.29 % of C_2H_6 selectivity, the total estimated price of C_2H_4 is 2971.88 US $/ton C_2H_4. An increase in both the C_2H_4 yield and selectivity is required in order to achieve a more industrially favorable C_2H_4 price.

Based on the *Eqn.* (4-14), around 25 % of C_{2+} yield and 22 % of C_{2+} selectivity are needed to maintain the overall ethylene price of around 1128.99 US $/ton of C_2H_4, which is below the industrial limit set by Cruellas et al. [59] techno-economics model.

4.6 Target case

4.6.1 Reactor geometry and operating conditions

Most of the research in this field focused on improving the C_{2+} yield and making this process feasible on larger scales. Based on the estimation of required the C_{2+} yield needed to achieve an economically feasible ethylene price (shown in *Section 4.5.4*), 25 % of C_{2+} yield and 22 % of C_{2+} selectivity are needed to maintain the overall ethylene price of around 1128.99 US $/ton C_2H_4, which is below the industrial limit set by Cruellas et al. [59] techno-economics model.

The aim is to obtain a target case that satisfies an increase in hydrogen molar flow rate on the feed side and a C_{2+} yield between the applicable industrial range on the sweep side. Remarks drawn from the model analysis developed in *Sections 4.3, 4.4,* and *4.5* will adjust the reactor conditions and enhance the membrane reactor performance. The adjusted reactor conditions are displayed in *Table* 4-12, and the improved C_{2+} yield, selectivity, and methane conversion are shown in *Table* 4-13.

Table 4-12: Dimensions and operating conditions (target case)

Parameter	Feed side	Sweep side	Membrane
Membrane thickness (t) [m]	-	-	1E-4
Full channel height (H) [m]	1E-3	1E-3	-
¼ Channel height ($H_{channel}$) [m]	5E-4	5E-4	-
Channel length ($L_{channel}$) [m]	2.5	2.5	-
Channel width ($w_{channel}$) [m]*	10E-2	10E-2	-
Temperature [K]	1133.15	1133.15	1133.15
Inlet pressure [Pa]	100000	100000	-
Inlet water mole fraction (feed)	0.8	-	-
Inlet nitrogen mole fraction (feed)	0.2	-	-
Inlet methane mole fraction (sweep)	-	0.7	-
Inlet nitrogen mole fraction (sweep)	-	0.3	-

Volumetric flow rate [STP][m^3/s]	7.5E-6	7.5E-6	-
Space time [kg s/m^3]	-	60	-
Catalyst density	-	3600	-
Porosity	-	0.999	-
Total catalyst mass [kg]	-	4.5E-4	-
Total membrane surface area [m^2]	-	-	2.5E-1
Catalyst per membrane surface area [kg/m^2]	-	1.8E-3	-

* Channel width is equal to the membrane width based on the reactor schematic

4.6.2 Model outputs (target case)

As shown in *Table 4-12*, the membrane thickness is decreased to 1E-4 m (100 microns) compared to 9E-4 m for the base case. It was found that decreasing the membrane thickness positively impacts the J_v due to the inverse relationship between the two parameters, as shown in *Eqn. (3-14*). The channel height is decreased to 5E-4 m compared to 1E-3 m for the base case; this corresponds to an entire channel height of 1 mm, which is engineerable. It also complies with the conclusion drawn in the systematic analysis about altering the channel height on the C_{2+} yield, presented in *Section 4.3.1.2*. The channel length increases to 2.50 m compared to 1.50 m for the base case; the increase in channel length complies with the systemic analysis conclusion. The increasing channel length positively impacts the C_{2+} yield and the overall membrane reactor performance, as presented in *Section 4.3.1.1*. The channel length chosen for the target case also lies in the length range reported in the literature [120].

The isothermal temperature applied to the target case is 1133.15 K, slightly higher than 1103.3 K, which is the temperature applied for the base case. Even though the increase is slight, the alternation aligns with the systematic analysis conclusion about the effect of the isothermal temperature on the C_{2+} yield. It was found that the reactor starts to favor the formation of the CO_x yield rather than the higher hydrocarbons at higher temperatures for the altered reactor conditions and dimensions, which is investigated further in *Section 4.6.3*. The pressure chosen is 1E+5 Pa (or 1 bar), which is equivalent to the absolute pressure at the STP condition, and it is consistent with the base case model and the

La_2O_3/CaO catalyst model developed in *Chapter 3*. The concentration of the inlet species in both the feed and sweep sides are based on the micro catalytic model developed by Stansch et al. [91].

Space-time increases from 1.86 to 60 kg s/m^3, aligning with the systematic analysis conclusion shown in *Section 4.3.2* while being the range specified in the model developed by Stansch et al. [91]. Increasing the space-time means increasing the time for the number of species that take up the specified control volume to enter or completely exit the reactor. In other words, the species, primarily methane and oxygen, have more time to react and convert into C_{2+}, which is why an increase in the C_{2+} is noticeable.

Catalyst porosity is decreased compared to the base case. The catalyst porosity directly impacts the total catalyst mass per membrane surface are used on the sweep side. As concluded from the systematic analysis, decreasing the porosity increased the catalyst mass, which increased the methane conversion and the C_{2+} yield.

Table 4-13 and *Table 4-14* show species concentration and membrane reactor performance criteria. The increase in channel length, isothermal temperature, space-time, and decreased membrane thickness lead to a 50 % increase in methane conversion between the base and target cases. These observations can be related to the concluded effects drawn from the systematic analysis presented in *Section 4.3.* The increase in methane conversion directly impacts the C_{2+} yield due to the direct relationship between the two quantities. This enhanced methane conversion increase led to a 23.73 % absolute percentage increase in the yield value between the two cases, allowing the targe case to achieve the economic yield limit specified of 25-30 % by Cruellas et al. [59] and also surpasses the economic C_{2+} yield and selectivity (estimated in *Section 4.5.4)* of 25 % yield and 22 %, respectively. The increase in methane conversion led to increased CO_x yield, which is expected due to their mathematical relationship.

Table 4-13: Species concentration in the feed and sweep channels (target case)

Concentration [mol/m^3]	**Inlet**	**Outlet**
$\dot{n}\ (H_2O)_{feed}$	32.07	1.63
$\dot{n}\ (H_2)_{feed}$	0	30.44
$\dot{n}\ (O_2)_{sweep}$	0	0.41
$\dot{n}\ (CH_4)_{sweep}$	28.06	13.24
$\dot{n}\ (C_2H_4)_{sweep}$	0	3.36
$\dot{n}\ (H_2O)_{sweep}$	0	16.09
$\dot{n}\ (C_2H_6)_{sweep}$	0	0.22
$\dot{n}\ (H_2)_{sweep}$	0	5.88
$\dot{n}\ (CO_2)_{sweep}$	0	6.18
$\dot{n}\ (CO)_{sweep}$	0	1.79

*Nitrogen concentration [mol/m^3] is 30.44 for feed and 12.03 for sweep

Table 4-14: Sweep side species conversion, selectivity, and yield values (target case)

Species	X_{O_2} **[%]**	X_{CH_4} **[%]**	**Selectivity [%]**	**Yield [%]**
O_2	97.34	-	-	-
CH_4	-	52.78	-	-
C_2H_4	-	-	45.32	23.92
C_2H_6	-	-	2.98	1.57
C_{2+}	-	-	48.30	25.49
CO_2	-	-	39.65	20.93
CO	-	-	12.05	6.36
CO_x	-	-	51.70	27.29

Table 4-13 shows the hydrogen molar flow rate on the feed side-channel outlet produced as a result of the water-splitting process in the feed side channel and also on the sweep side-channel outlet produced as a result of nonselective oxidation of methane to carbon monoxide (reaction 3), thermal gas-phase dehydrogenation of ethane (reaction 7) and the water-gas-shift reaction (reaction 9). There is an increase in the produced hydrogen for the target case compared to the base case. The increase can be related to various altered factors between the two scenarios. Altering the reactor dimension between the two cases can explain the noticeable increase in hydrogen production, significantly increasing channel length and space-time, allowing the water more time and volume to split into oxygen and hydrogen. On the sweep side, the concentration of hydrogen exhibited a dependence on the space-time that was very similar to the one observed for carbon monoxide. In addition, the increase in isothermal temperature led to an overall increase in the reaction rates for the target case, which led to increasing the concentration of hydrogen.

Table 4-15: Mass balance (target case**)**

Mass flow rate [g/s]	**Inlet**	**Outlet**	**Difference**
Total feed mass flow rate	6.02E-3	2.37E-3	3.65E-3
Total sweep inlet mass flow rate	5.90E-3	9.55E-3	3.65E-3

Tolerances applied to the target case are similar to tolerances applied to the base case, which are 1E-14 for the absolute tolerance and 1E-7 for the relative tolerances. Lastly, similar to the base case scenario, a mass flow rate balance is conducted to validate the mass balance of the model, as shown in *Table* 4-15.

4.6.2.1 Species concentration along the feed and sweep channels

In order to have a better understanding of the target case, species concentration along the feed and sweep channels is illustrated in this section. The feed channel species concentrations are shown in *Figure 4-11*, while the sweep channel species concentrations are shown in *Figure 4-12*. The concentration of all the species is calculated based on the molar flow rate and the total volumetric flow rate, as shown in *Eq. (4-15)*.

$$C_i = \frac{n_i}{\dot{V}} \tag{4-15}$$

Where,

- C_i: concentration of species 'i', [mol/m^3]
- n_i: molar flow rate of species 'i', [mol/s]
- $\dot{V}$: volumetric flow rate, [m^3/s]

As shown in *Figure 4-11 (a)*, water serves as the oxygen source, and a water thermolysis reaction takes place on the feed side channel (high $P(O_2)$), specifically on the membrane surface. The heterogeneous water thermolysis on the LCF-91 membrane results in hydrogen and lattice oxygen production, as shown in *Eq.(2-6)*. The decreasing water concentration trend along the reactor length correlates with the hypothesis and corresponds with the water-splitting process mechanism.

Figure 4-11(b) shows an increasing concentration trend of hydrogen along the feed side channel length. The hydrogen-oxygen bonds break either on the membrane surface (heterogeneously) or in the gas phase (homogeneously). Next, the hydrogen radicals recombine into hydrogen molecules carried away by the feed gas.

Figure 4-11 (c) shows that nitrogen is an inert carrier gas to carry the desired amount of water into the feed side chamber. Nitrogen is an inert gas that does not get involved in the reaction; its concentration does not change along the reactor length.

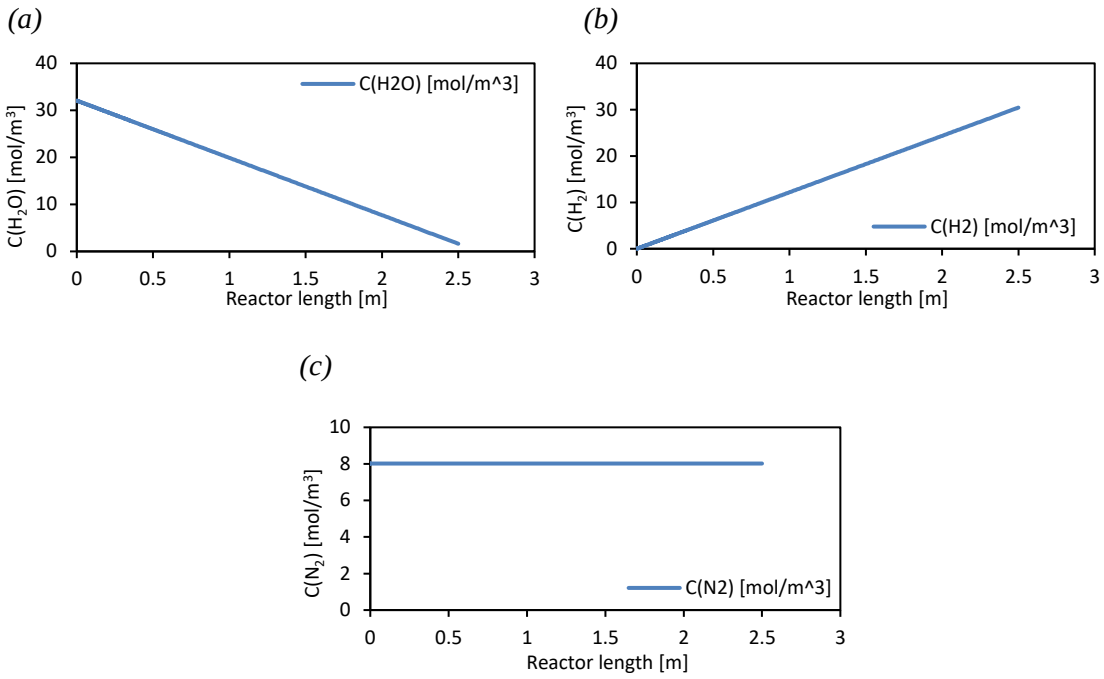

Figure 4-11: Feed channel species concentrations along reactor length (a) H_2O concentration (b) H_2 concentration (c) N_2 concentration (target case reactor geometry and operating conditions)

Figure 4-12 (a) and *(b)* show the oxygen and methane concentration along the sweep side channel length. The oxygen concertation shows a gradual increase at the channel's beginning, which corresponds to the oxygen permeation process through the membrane. The oxygen starts to be consumed afterward during the OCM process. The gradual increase in oxygen concentration seen between 0.5 to 2.5 m can be linked to the decrease in the destruction rate of oxygen, which is caused by the decrease in reaction rates 1,2,3,4, and 5. The entire oxygen trend on the sweep side channel will be investigated in *Section 4.6.4.* Methane and nitrogen are fed into the sweep side channel. The methane concentration shows a gradually decreasing trend that indicates its consumption and shows the influence of methane on the rate of consecutive selective reactions.

Figure 4-12 (c) and *(e)* show the C_{2+} concentrations along the sweep side channel length. The course of ethane concentration indicates that this component is formed as a primary product of the OCM reaction. It also shows how consecutive reactions strongly influence ethane. The dependence of the ethylene concentration on the ethane yield confirms the generally accepted thesis that ethylene is formed in a consecutive reaction of ethane as a result of heterogeneous catalytic oxidative

dehydrogenation of ethane (reaction 5) and indicates that ethylene also is an intermediate product of the OCM reaction.

Figure 4-12 (d) shows an increasing trend of H_2O on the sweep side channel. H_2O is considered one of the primary products due to the OCM reaction. The increase of water concentration in the channel can dilute the system, increasing the conversion of reactant and C_{2+} yield.

Figure 4-12 (f) and *(h)* show the increasing CO_x concentration along the sweep side channel length. The steep gradient of the CO_x concentrations indicates that these components are formed as a primary product of the OCM reaction. The presence of CO_2 in the mixture inhibits the overall catalytic reaction rate and may cause a drop in conversion, selectivity, and yield.

Figure 4-12 (g) shows an increasing hydrogen concentration along the sweep side channel length. Hydrogen is produced on the sweep side as a result of nonselective oxidation of methane to carbon monoxide (reaction 3), thermal gas-phase dehydrogenation of ethane (reaction 7), and the water-gas-shift reaction (reaction 9). The yield of hydrogen exhibited was very similar to the one observed for carbon monoxide, which was also reported by Stansch et al. [91].

Figure 4-12 (i) shows the nitrogen concentration along the sweep side channel length. Nitrogen carries the task of controlling the temperature in the reactor and overcoming the challenge of hot spot formation since OCM is a highly exothermic reaction. Similar to the feed side channel, Nitrogen does not get involved in the reaction; that is why its concentration does not change along the reactor length.

(a) *(b)*

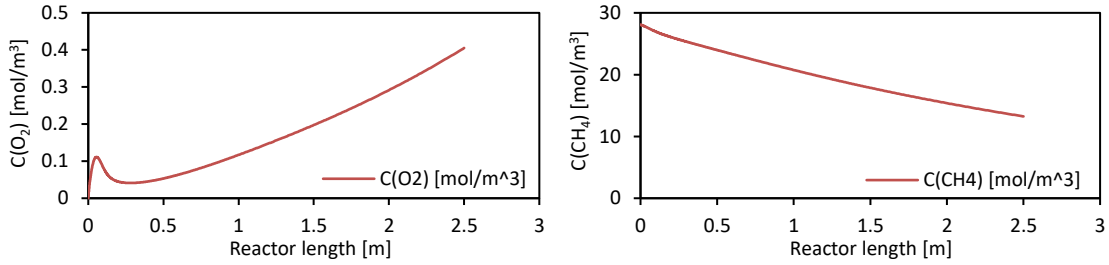

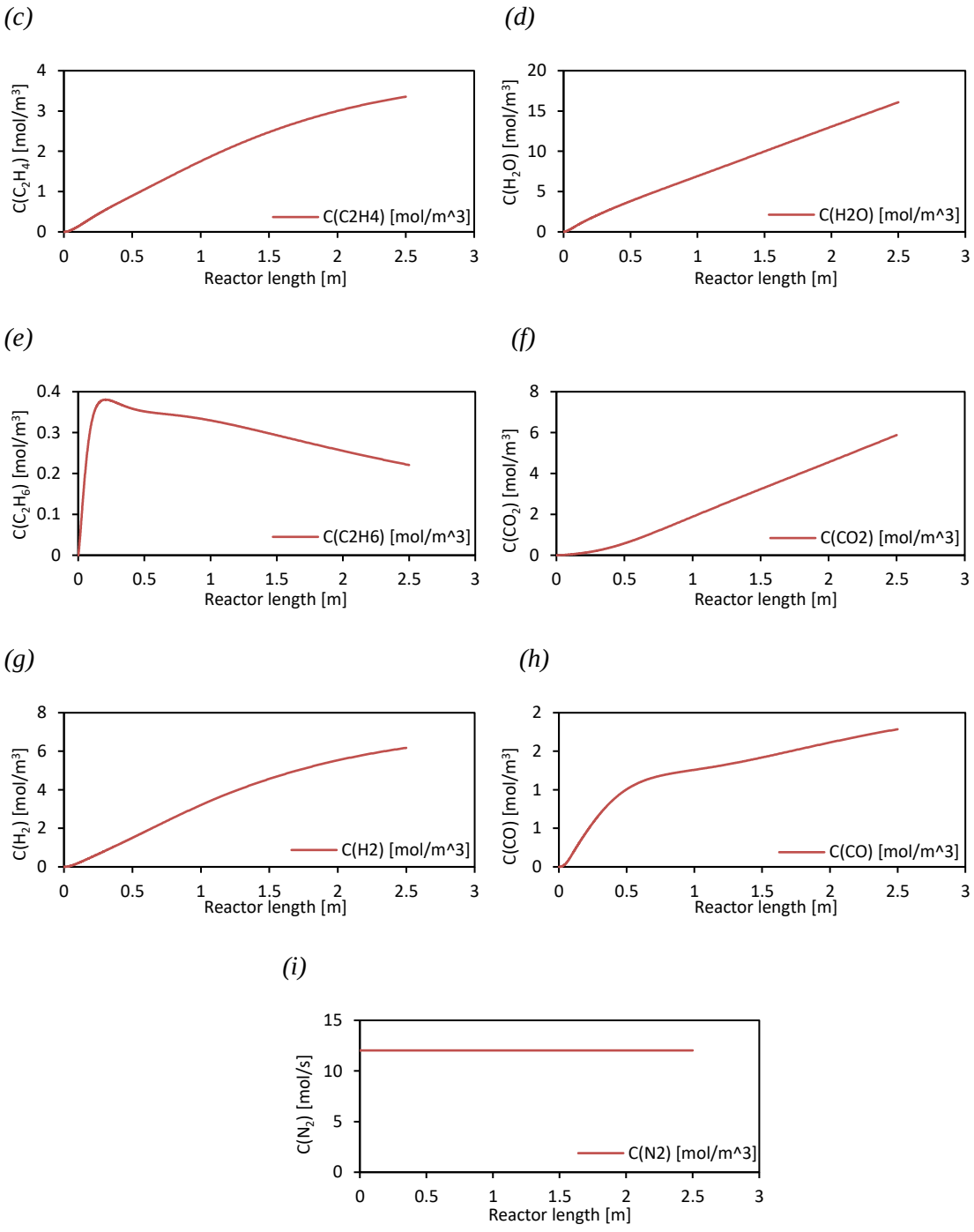

Figure 4-12 : Sweep channel species concentrations along reactor length (a) O_2 concentration (b) CH_4 concentration (c) C_2H_4 concentration (d) H_2O concentration (e) C_2H_6 concentration (f) CO_2 concentration (g) H_2 concentration (h) CO concentration (i) N_2 concentration (target case reactor geometry and operating conditions)

4.6.3 Effect of isothermal temperature on C_{2+} yield, methane conversion, and CO_x yield (target case)

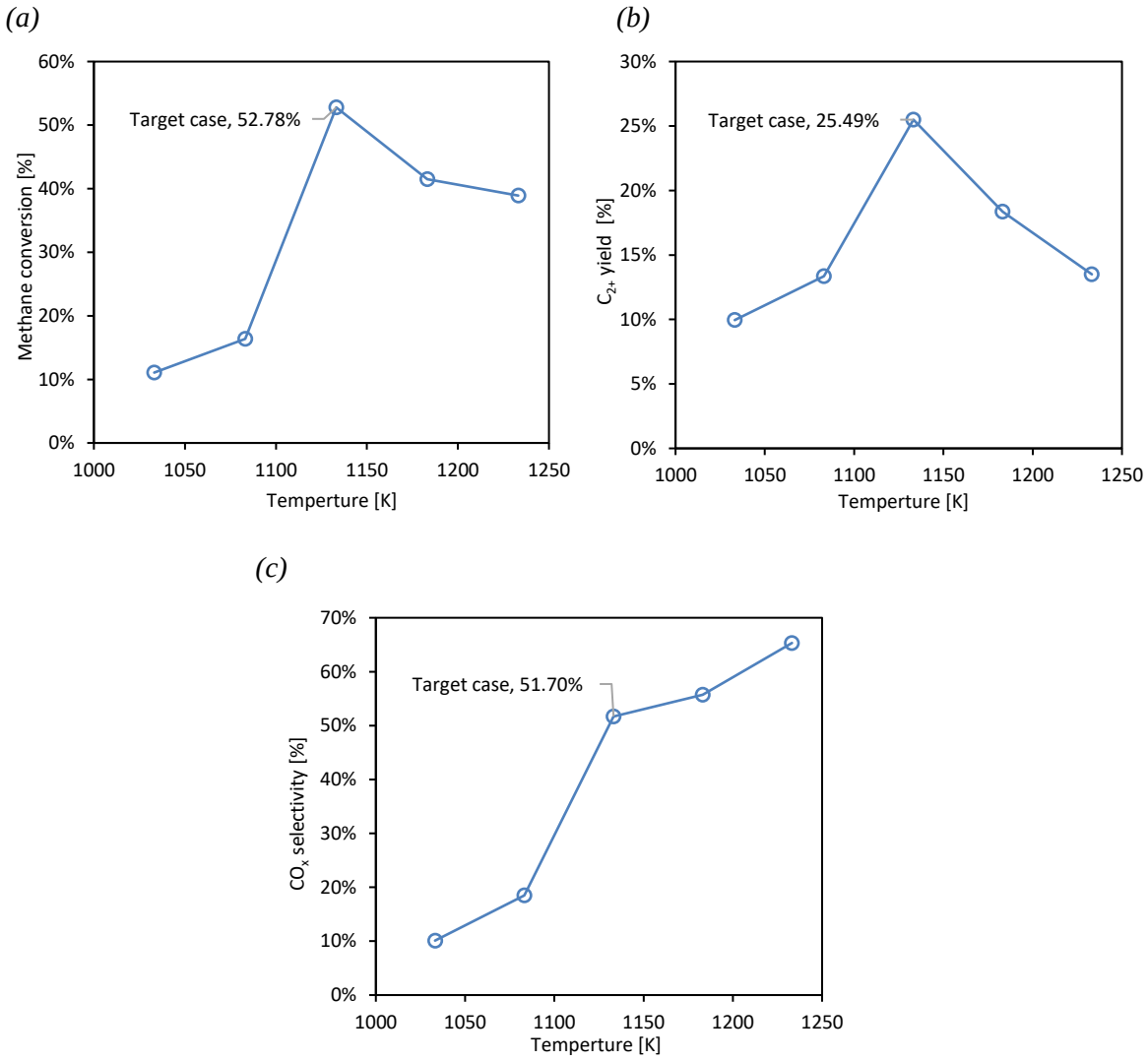

Figure 4-13 : Effect of altering isothermal temperature on (a) methane conversion, (b) C_{2+} yield (c) CO_x selectivity (target case) (isothermal condition, pressure drop applied, target case reactor dimensions, space time : 60 kg s/m^3 and $\dot{V}_{STP(feed\ \&\ sweep)}$: 7.50E-6 m^3/s)

The effect of isothermal temperature on the C_{2+} yield, methane conversion, and CO_x was examined for the target case reactor dimensions and conditions. *Figure 4-13 (a)* shows that methane conversion increases with the isothermal temperature from 11.07 % in case 1 to 52.78 % in the target case.

However, there is a noticeable drop in methane conversion from 52.78 % in the target case to 38.92 % in case 4.

Figure 4-13(b) shows a similar trend of altering isothermal temperature on C_{2+} yield. The temperature increase from 1003.15 to 1133.15 K shows an increase in C_{2+} yield from 9.95 % to 25.49 % (target case C_{2+} yield), which is expected due to the increase in methane conversion at the specified temperatures. The increase in methane conversion is caused by the increase in the reaction rates due to elevated temperatures, which increases the formation rates and eventually increases the conversion rate of methane. The direct relationship between C_{2+} yield and methane conversion explains the increase in C_{2+} yield at specified temperatures. There is a significant drop in the methane conversion and the C_{2+} yield at temperatures above 1133.15 K. The drop is due to the prevailing CH4 combustions at higher temperatures, thus hampering the achievement of high selectivity towards the desired result products. The drop is also accompanied by an increase in the CO_x selectivity shown in *Figure 4-13 (c)*. At the specified temperatures, oxidation of C_{2+} started to predominate, and the reactor started to favor the formation of CO_x rather than higher hydrocarbons. Higher reactor temperatures were not applied to the target case to increase the methane conversion.

4.6.4 Oxygen concentration along the membrane on the sweep side

In this section, the oxygen trend along the reactor length is investigated. It is essential to investigate how oxygen is consumed along the sweep side channel. It would clarify how functional the membrane permeates the oxygen from the feed side to the sweep side.

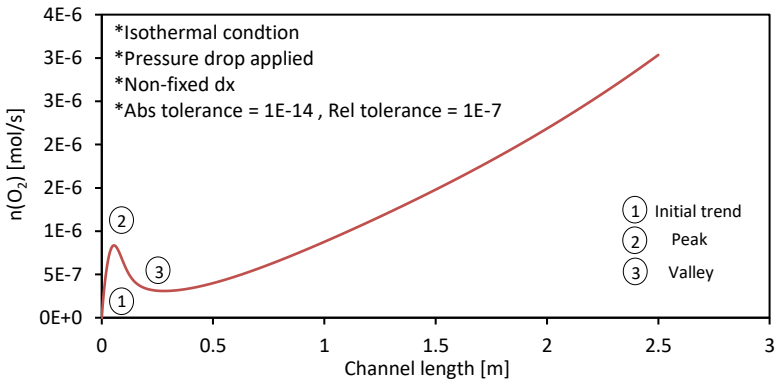

Figure 4-14: Oxygen molar flow rate trend vs. channel length

Figure 4-14 shows the oxygen molar flow rate trend along the reactor length. This section will investigate the initial increasing trend, the formation of the peak trend, and the valley. The three highlighted sections in *Figure* 4-14 correspond to the investigated iterations.

4.6.4.1 Initial trend

The increase in the oxygen molar flow rate trend (starting from 0 to 1.22E-5 m) is annotated in *Figure* 4-14 as (1). In order to understand why the peak trend starts formulating around the highlighted reactor length, it is crucial to study the change in variables such as the change in oxygen molar flow rate ($\Delta\dot{n}_{O_2}$), the destruction rate ($\dot{W}_{O_2}$), and oxygen flux (J_{O_2}) which affects the oxygen trend directly. The $\Delta\dot{n}_{O_2}$ is directly affected by the $\dot{W}_{O_2}$ and J_{O_2} Along the reactor length as shown in *Section 3.3.3.1*. The variation of these parameters at the specified reactor length is presented in *Table C - 1*.

As shown in *Table C - 1*, the $\dot{W}_{O_2}$ is lower than the J_{O_2} before the peak position, which results in a positive $\Delta\dot{n}_{O_2}$ which affects the oxygen trend positively and results in an increasing trend. In order to investigate the trend that the $\dot{W}_{O_2}$ follows it is important to look at the reaction rates which directly impact the $\dot{W}_{O_2}$as shown in *Section 3.3.3.1*. The reaction rates for the specified iterations are shown in *Table C - 2*. $\dot{W}_{O_2}$ shows an increasing trend because all the reaction rates increase along with the specified iterations. The increase in the reaction rates is due to the species' partial pressures, shown in *Table C - 3*.

Table 4-16: Reaction order for methane oxidation reactions (1, 2 and 3)

Reaction	m_u	n_u
Step 1 : $CH_4 + 2O_2 \rightarrow CO_2 + 2H_2O$	0.24	0.76
Step 2 : $2CH_4 + 0.5O_2 \rightarrow C_2H_6 + H_2O$	1	0.4
Step 3 : $CH_4 + O_2 \rightarrow CO + H_2O + H_2$	0.57	0.85

The partial pressure of methane (P_{CH_4}) is the only partial pressure showing a decreasing trend along with the specified iterations, which is expected. The methane is being consumed gradually as a primary reactant for the OCM process. The decrease in the P_{CH_4} affects reactions 1, 2, and 3 according to the Hougen-Watson rate and Power-Law rate equations shown in *Section 3.3.3.1*. However, reactions 1 and 3 still show an increasing trend because of the increase in the partial pressure of oxygen (P_{O_2})

which has a higher reaction order, as shown in *Table* 4-16. For reaction 2, the rate at which the P_{O_2} increases is 24.76 % which is significantly higher than the rate at which P_{CH_4}decreases which is around 3.84E-5%, and that is why the overall reaction two trends still increase.

To conclude this section, the initial increasing trend occurs due to the increase in most species' formation rates along with the specified iteration, showcased by the increase in the partial pressures of the sweep side species.

4.6.4.2 Peak

The peak trend *(*4.95E-2 and 5.96E-2 m) is annotated in *Figure 4-14* as (2) oxygen molar flow rates that form the peak trend along the reactor length. Similar to the previous section, it is crucial to study the change in variables such as the change in oxygen molar flow rate (closely $\Delta\dot{n}_{O_2}$), the destruction rate ($\dot{W}_{O_2}$), and oxygen flux (J_{O_2}) which affects the oxygen trend directly. The variation of these parameters at the specified reactor length is presented in *Table C - 4*. Similar to the initial trend section the $\dot{W}_{O_2}$ is lower than the J_{O_2} before the peak position, which results in a positive $\Delta\dot{n}_{O_2}$ which affects the oxygen trend positively and results in an increasing trend. After the peak, the $\dot{W}_{O_2}$ is higher than the J_{O_2}.This trend results in a negative $\Delta\dot{n}_{O_2}$which affects the oxygen trend negatively and results in a decreasing trend. The methane oxidation reactions (1, 2, and 3) and CO, C_2H_6, and C_2H_4 oxidation reactions (4, 5, and 6) are examined because they affect the $\dot{W}_{O_2}$ directly, as shown in *Section 3.5.2.1.* As shown in *Table C - 5*, $\dot{W}_{O_2}$ increases before the peak because all the reaction rates increase. However, some reaction rates increase after the peak, and some do not.

- Methane oxidation reactions (1, 2, and 3) have an increasing trend before the peak and a decreasing trend after the peak
- CO, C_2H_6, and C_2H_4 oxidation reactions (4, 5, and 6) have an increasing trend before the peak and also an increasing trend after the peak

The increase in CO, C_2H_6, and C_2H_4 oxidation reactions (4, 5, and 6) rates has a more significant impact on the $\dot{W}_{O_2}$seeing as the overall value increases after the peak. The partial pressures values of the sweep side species are investigated to understand why some of the reaction rates fluctuate around the peak point,

After the peak, the drop in the oxygen and methane partial pressures slowed down methane oxidation reactions (1, 2, and 3). At the same time, the increase in CO, C_2H_6, and C_2H_4 oxidation reactions (4, 5, and 6) is due to the increase in the partial pressures of CO, C_2H_6, and C_2H_4, respectively. Even with the drop in the oxygen partial pressure along the reactor length (especially after the peak), the increase of the species mentioned is higher due to their higher reaction order, as shown in *Table* 4-17.

Table 4-17 : Reaction order for CO, C_2H_6, and C_2H_4 oxidation reactions

Reaction	$\mathbf{m_u}$	$\mathbf{n_u}$
Step 4 : $CO + 0.5O_2 \rightarrow CO_2$	1.00	0.55
Step 5: $C_2H_6 + 0.5O_2 \rightarrow C_2H_4 + H_2O$	0.95	0.37
Step 6 : $C_2H_4 + 2O_2 \rightarrow 2CO + 2H_2O$	1.00	0.96

Lastly, the gradual decrease of the J_{O_2} Along the reactor, length is investigated to determine why this occurs along the specified reactor length. According to *Eqn. (3-18)*, the oxygen flux is directly affected by the total concentration of sweep-side oxygen, and the feed-side consumed water.

As shown in *Table C - 7*, the oxygen concentration increases before the peak due to the increase in the molar flow rate of oxygen due to the positive $\Delta\dot{n}_{O_2}$. This increase reduces the potential chemical term due to the inverse relationship between the two parameters, which lowers the vacancy and oxygen flux, as shown in the presented data. After the peak, the oxygen concentration decreases due to the decrease in the molar flow rate of oxygen due to the negative $\Delta\dot{n}_{O_2}$. This decrease boosts the potential chemical term; however, the vacancy flux and the oxygen flux terms still decrease due to the surface reaction resistance on the feed side (R_f) and surface reaction resistance on the sweep side (R_s).

The decrease of the surface reaction resistances in the feed and sweep sides are due to the constant decrease in the molar flow rate of water on the feed side and the decrease in oxygen molar flow rate on the sweep side. In conclusion, the formation of the peak is due to two main reasons:

(1) The gradual decrease of the J_{O_2} along the reactor length

a. The increase in the oxygen concentration on the sweep side-channel and the decrease in the concertation of water on the feed side-channel

b. The oxygen flux drops along the channel, and as both water and methane concentrations decrease along the membrane, the potential chemical difference for the oxygen permeation becomes smaller. As a result, the oxygen flux at the channel outlet is lower than the values at the inlet.

(2) The increase in the destruction rate of oxygen $\dot{W}_{O_2}$

a. The increase in CO, C_2H_6, and C_2H_4 oxidation reactions (4, 5, and 6), respectively, after the peak, is caused due to the increase of CO, C_2H_6, and C_2H_4 partial pressures, in addition to a higher impact on the WO_2 due to higher reaction order

4.6.4.3 Valley

The gradual increasing trend annotated in *Figure* 4-14 as (3) is investigated in this section. As shown in *Table C - 8*, the $\Delta\dot{n}_{O_2}$ turns positive after the iteration indicated. The reason behind the $\Delta\dot{n}_{O_2}$ from negative to positive is that the J_{O_2} at this position starts to be greater than the $\dot{W}_{O_2}$, even though the two parameters are decreasing. This observation means that the rate at which oxygen is added to the sweep side is more than the rate the OCM process consumes it.

Similar to the previous section, the reaction rates 1, 2, 3, 4, 5, and 6 are examined because of their direct effect on the $\dot{W}_{O_2}$. In order to explain the reason behind the drop-in $\dot{W}_{O_2}$ reaction rates were examined and presented in *Table C - 9.*

The partial pressures for the sweep side species along the specified iterations are examined and presented in *Table C - 10.* Similar to the previous sections, the partial pressures will clarify the reaction rates trends obtained. As shown in *Table C - 9*, the drop-in reaction rates 1, 2, 3, and 5 after the indicated iteration indicate why there is a drop in the $\dot{W}_{O_2}$.

- Reaction 1 rate: decreases due to the decrease in P_{O_2} and P_{CH_4}.
- Reaction 2 rate: decreases due to the decrease in P_{O_2} and P_{CH_4}.
- Reaction 3 rate: decreases due to a decrease in P_{O_2} and P_{CH_4}.
- Reaction 4 rate: increases due to the increase of the P_{CO} while having a higher reaction order than P_{O_2} which decreases along the reaction length.
- Reaction 5 rate: decreases due to the decrease of both $P_{C_2H_6}$ and P_{O_2}.
- Reaction 6 rate: increases due to the increase of the $P_{C_2H_4}$ while having a higher reaction order than P_{O_2} which decreases along the reaction length.

It is noticeable that P_{O_2} is decreasing before and after the highlighted position. At iteration 339, even with the increase in the oxygen molar flow rate, the sum of the sweep side molar flow rates increases, which decreases the molar ratio of the partial pressure of oxygen. In conclusion, the gradual increase in oxygen molar flow rate is because of the decrease in the destruction rate of oxygen, which is caused by the decrease in reaction rates 1,2,3,4, and 5 before and after the highlighted iterations. The decrease in the reaction rates is because of the increase in the summation of molar flow rates, which decreases the molar ratio of oxygen and the partial pressure of oxygen.

4.6.5 Carbon oxides (CO_x) concentration along the sweep side-channel

This section investigates the carbon oxides concentration trend along the reactor length. Investigating the stoichiometric reaction rates along the sweep side channel is essential to establish which reaction rates contribute to carbon oxides production. Several stoichiometric reactions are responsible for the production of carbon oxides. According to Stansch et al. [91], reaction 1 involves the nonselective methane oxidation to carbon dioxide. Reaction 3 involves the nonselective oxidation of methane to carbon monoxide (two fast steps were lumped, i.e., formation and consecutive decomposition of formaldehyde). Reaction 4 involves the oxidizing of carbon monoxide to carbon dioxide. Reaction 6 involves the further reaction of ethylene with oxygen to carbon monoxide. While reaction 8 involves the further reaction of ethylene with water via steam reformation of ethylene to carbon monoxide. Finally, reactions 9 and 10 involve the water-gas-shift reaction in both directions.

In order to examine the CO_x concentration along the sweep side channel, the stoichiometric rates were examined between 0.496 to 0.505 m at the target case reactor conditions. This reactor length corresponds to a noticeable change in the CO_x concentrations along the reactor length, as shown in *Figure 4-12 (f)* and *(h).*

4.6.5.1 Carbon dioxide (CO_2)

Reactions 1,4,9, and 10 directly affect the formation rate of carbon dioxide, as shown in *Eq.* (4-16*).* Reactions 1 and 4 are solved using the Hougen-Watson type equation, while reactions 9 and 10 are solved using the power-law rate equation, as explained in *Section 2.5.*

$$\dot{W}_{CO_2} = \left[r_1 \times dm_{catalyst} \right] + \left[r_4 \times dm_{catalyst} \right] + \left[r_9 \times dm_{catalyst} \right] + \left[-r_{10} \times dm_{catalyst} \right] \quad (4\text{-}16)$$

As shown in *Figure 4-15 (f)*, the increase in the concentration of carbon dioxide is due to reaction four which involves the oxidizing of carbon monoxide to carbon dioxide and exhibits the highest reaction rate. In addition, the increase in the concentration of carbon dioxide can also be linked to the increase in reaction 9 rate, which involves the forward water-gas-shift reaction. In addition, the activation energies for the formation of carbon monoxide and carbon dioxide, which amounted to 48 and 68 kJ/mol, respectively, are significantly lower than the activation energy of the formation of ethane which may contribute to the noticeable increase in their formation.

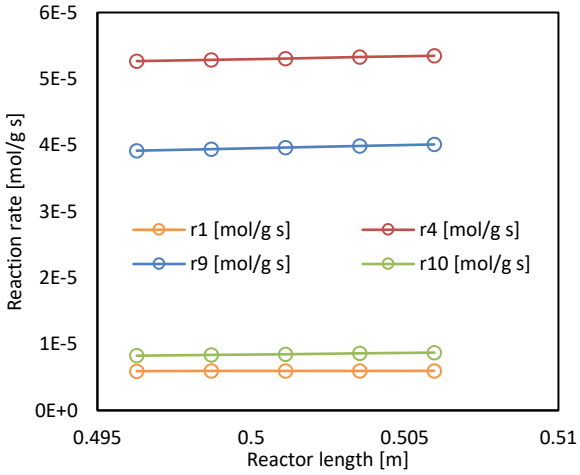

Figure 4-15: Reaction rates (1,4,9 and 10) along reactor length (target case conditions)

4.6.5.2 Carbon monoxide (CO)

Reactions 3,4,6,8,9 and 10 directly affect the formation rate of carbon monoxide, as shown in *Eq.*(4-17*)*. Reactions 3,4 and 6 are solved using the Hougen-Watson type equation, while reactions 8,9, and 10 are solved using the power-law rate equation as explained in *Section 2.5.*

$$\dot{W}_{CO} = \left[r_3 \times dm_{catalyst}\right] + \left[-r_4 \times dm_{catalyst}\right] + \left[(2 \times r_6) \times dm_{catalyst}\right] + \left[(2 \times r_8) \times dm_{catalyst}\right] + \left[-r_9 \times dm_{catalyst}\right] + \left[r_{10} \times dm_{catalyst}\right] \quad (4\text{-}17)$$

Figure 4-15(h) shows an overall increase in the concentration of carbon monoxide due to the increase in its partial pressure due to the catalytic oxidation of ethylene and catalytic conversion of methane to carbon monoxide. However, there is a decrease in the rate of formation of carbon monoxide at the specified reactor iterations, which corresponds to the same iterations at which there is a noticeable

increase in the formation rate of carbon dioxide. The decrease in carbon monoxide formation rate is due to the decrease in reaction 6 rate. Even though reaction 8 has the same stoichiometric coefficient as reaction 6, its rate is two magnitudes lower than reaction 6.

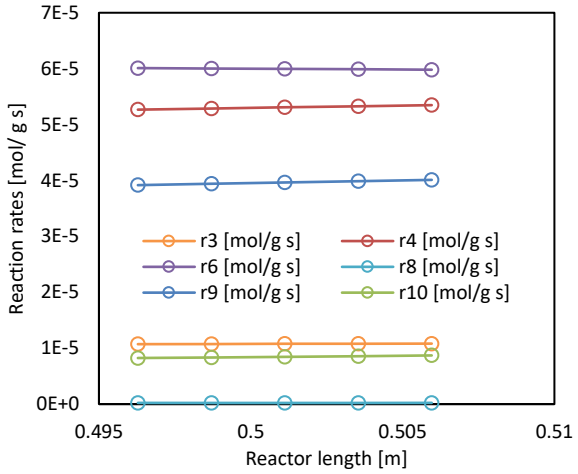

Figure 4-16: Reaction rates (3,4,6,8,9 and 10) along reactor length (target case conditions)

The decrease in reaction 6 rate is due to the increase in the P_{CO_2} and the adsorption enthalpy of CO_2. According to the kinetics parameters from Stanch et al. [91] shown in *Table 2-2*, reaction 6 has the highest adsorption enthalpy of CO_2 (-211 kJ/mol) compared to reactions 1 to 5 are solved using the Hougen-Watson type equation. The significantly higher inhibition of this reaction by CO_2 could not be clarified yet, according to Stanch et al. [91]. In addition, reaction 4 and 9, which involves oxidizing carbon monoxide to carbon dioxide and the water-gas-shift forward reaction, affect the rate of formation of the carbon monoxide due to the negative sign that correlates with the stoichiometric coefficient of the carbon monoxide in these reactions. Lastly, reaction 10 involves the reverse water-gas-shift reaction and shows the highest increase in rate compared to the other displayed reactions. The rapid increase in reaction 10 rate correlates with the hypothesis stated in the model developed by Stanch et al. [91] that a fast water gas shift reaction follows catalytic steam reforming of ethylene.

4.6.6 Membrane vs. pre-mixed reactor

It is crucial to investigate the implications of using a membrane OCM reactor versus a pre-mixed reactor to understand the importance of implementing the membrane technology in the OCM process for the co-production of hydrogen and ethylene.

4.6.6.1 Membrane reactor scenario

This scenario includes a catalytic membrane reactor with both feed and sweep sides. Due to the water-splitting process, the oxygen-permeable membrane permeates oxygen from the feed side. The oxygen permeated is used to oxidize the methane injected in the sweep side in the oxidative coupling of the methane process to produce higher hydrocarbons. This scenario's reactor conditions and results are based on the target case conditions shown in *Table* 4-12.

4.6.6.2 Pre-mixed reactor

For this scenario, membrane function is disabled, which means that oxygen needed for the OCM process is directly injected into the reactor. The inlet oxygen molar flow rate and mole fractions are calculated based on the difference between the inlet and outlet water molar flow rates on the feed side from the membrane reactor scenario, as shown in *Eq. (4-18).*

$$\dot{n}_{O_2,sweep,inlet} = \frac{\left(\dot{n}_{H_2O,feed,inlet} - \dot{n}_{H_2O,feed,outlet}\right)_{membrane\ \text{scenario}}}{2} \tag{4-18}$$

Where,

- $\dot{n}_{O_2,sweep,inlet}$: inlet oxygen molar flow rate on sweep side, [mol/s]
- $\dot{n}_{H_2O,feed,inlet}$: inlet water molar flow rate on the feed side, [mol/s]
- $\dot{n}_{H_2O,feed,outlet}$: outlet water molar flow rate on the feed side, [mol/s]

Furthermore, the inlet methane and nitrogen mole fractions are calculated based on the updated mole fraction of oxygen calculated. The isothermal temperature condition is still maintained and assumes

that the pressure drop is negligible. Finally, the volumetric flow rate was adjusted to maintain consistent methane and nitrogen inlet molar rates similar to the membrane reactor scenario.

4.6.6.3 Results & discussion

The conversion of reactants selectivity evaluates the performance of the reactor and yield of products which are calculated using *Eq(3-40), Eq(3-41), Eqn. (3-42),* and *Eqn. (3-43),* respectively. In addition, the CO_x selectivity is calculated using *Eq(3-44)*. The CO_x selectivity is an important parameter to investigate since it determines how clean the technology is. Low CO_x selectivity will ensure that the membrane reactor is more selective towards higher hydrocarbons which is favorable.

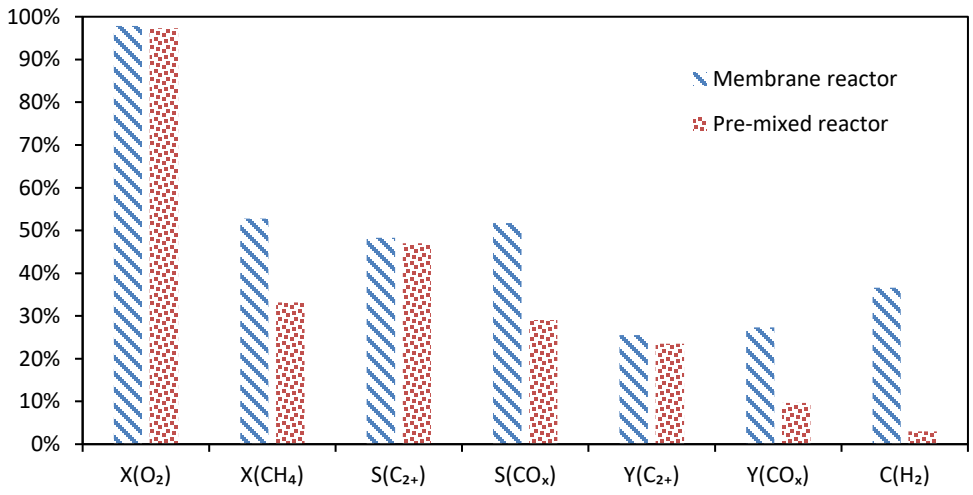

Figure 4-17: Comparison between membrane reactor (target case) and pre-mixed reactor under the same initial conditions

Based on the results shown in *Figure* 4-17, the implementation of the membrane resulted in various improvements compared to the pre-mixed reactor. Firstly, a 19 % absolute percentage increase in methane conversion is accompanied by a 2 % increase in the C_{2+} yield and a 1.30 % absolute percentage increase in C_{2+} selectivity. The membrane reactor also showed a 33.57 % absolute percentage increase in the hydrogen concentration compared to the pre-mixed reactor. It is important to note that the hydrogen concentration for the membrane reactor also considered the hydrogen produced as a result of the water-splitting process on the feed side channel, in addition to the hydrogen produced on the sweep

side as a result of nonselective oxidation of methane to carbon monoxide (reaction 3), thermal gas-phase dehydrogenation of ethane (reaction 7) and the water-gas-shift reaction (reaction 9).

However, the membrane reactor shows a higher selectivity towards CO_x with a 22.62 % absolute percentage increase in CO_x selectivity, which is also reflected in the higher CO_x yield for the membrane reactor case. The higher CO_x selectivity and yield obtained can be explained due to the significant increase in the methane conversion that is noticeable in the membrane reactor compared to the pre-mixed reactor. This increase in CO_x output can hinder the adaption of this technology on a larger scale due to its environmental effects.

4.7 Chapter summary

This chapter showcased the development of a base case scenario for the one-dimensional catalyst membrane reactor model developed in *Chapter 3*. Several assumptions are applied to the current base case, including isothermal operating and the correlation between reaction rates on the feed and sweep side and the membrane's oxygen flux. The chapter also showcased the required geometry and reactor condition needed to develop the base case and the remarks drawn from the base case scenario results. The base case showed a relatively lower C_{2+} yield of 1.86 %, which was expected due to the low methane conversion of around 1.76 %.

The chapter also tried to estimate the C_{2+} yield and selectivity required to achieve an industrially favorable price, concluding that this research's OCM membrane reactor technology is economically feasible. Although the estimation does not cover all financial matters, it is a good indicator for choosing among alternatives and finding out which part of the process should be improved. It was concluded that around 25 % of C_{2+} yield and 22 % of C_{2+} selectivity were needed to maintain the overall ethylene price of around 1128.99 US $/ton C_2H_4, which is below the industrial limit indicated by Cruellas et al. [59] techno-economic model.

This chapter developed a model analysis section to investigate altering the reactor dimensions and conditions on the membrane reactor performance. The systematic analysis showed that increasing channel length, isothermal temperature, space-time, and catalyst mass per membrane surface area and decreasing the membrane thickness and channel height could positively impact the methane conversion and the C_{2+} yield. Sensitivity analysis is used to evaluate the dependence of the design metrics on different parameters. The sensitivity of the C_{2+} yield and CH_4 conversion were examined concerning design, operation, and kinetics parameters. The averaged sensitivity results show that the membrane

reactor is most sensitive to the operating temperature. Higher operating temperature leads to faster surface kinetics, and therefore, methane is consumed faster with the increase of oxygen flux. A 10 % increase in the isothermal temperature led to a 79 % increase in the methane conversion and a 58 % increase in the C_{2+} yield. The systematic and sensitivity analysis remarks were used to develop a target case in which the methane conversion reached 52.78 % along with a C_{2+} yield of 25.49 %. These optimum case results demonstrated how this technology could compete with the current ethylene prices, as it can achieve the economic yield limit specified of 25-30 % by Cruellas et al. [59] and also surpasses the economic C_{2+} yield and selectivity (estimated in *Section 4.5.4)* of 25 % yield and 22 %, respectively.

Lastly, the chapter showcased the importance of implementing a membrane in a reactor to produce higher hydrocarbon using the OCM process. A comparison was drawn between a membrane reactor and a premixed reactor (the membrane function is disabled). The reactor conditions were matched between the two cases. The amount of oxygen permeated in the membrane reactor case was used as an inlet oxygen concentration for the premixed reactor. A comparison between the target case and a pre-mixed reactor case showed that the implementation of the membrane resulted in various improvements compared to the pre-mixed reactor, including an enhanced methane conversion, which is accompanied by an increase in the C_{2+} yield and the C_{2+} selectivity. The improvements also included increasing the percentage concentration of hydrogen produced as a by-product. The increase in the methane conversion is accompanied by increased CO_x selectivity and yield. The increase in CO_x output can hinder the adaption of this technology on a larger scale due to its environmental effects.

Chapter 5

Conclusions and future work

5.1 Conclusions

In this research, hydrogen and ethylene co-production in an oxygen permeable membrane reactor is studied. The membrane has two functions; firstly, they are used as product separators in which H_2O provided in the reactor is separated into H_2 and O_2 that diffuses through the membrane. Meanwhile, the membrane acts as a reactant provider to ultimately provide oxygen molecules through the permeation process to the sweep side, where the OCM process occurs for ethylene production.

The one-dimensional model is developed based on a plug flow reactor (PFR). The PFR is usually used to model reactions involving changing temperatures, pressures, and flow densities. A typical PFR could be a tube packed with solid material (frequently a catalyst). Which are called packed bed reactors or PBRs; The geometry of the membrane reactor modeled is based on a monolith reactor to account for the simultaneous feeding of water and methane in a feed and sweep channel, respectively. In addition, the monolith reactors have a high surface-area-to-volume ratio and can be readily produced and modularized on an industrial scale. Ordinary differential equation solver from MATLAB is used to solve the governing differential equations that concern mass balance and pressure drop along the length of the reactor.

The use of catalysts on the membrane surface is essential as it improves the catalytic surface activation reaction while the oxygen permeation rate increases. In addition, incorporating the catalyst microkinetics into the membrane reactor model can help solve the rate of formation parameters of the species in the sweep side of the membrane reactor, which involves the OCM mechanism for higher hydrocarbons production.

Sensitivity and systematic analysis in *Chapter 4* showed that increasing channel length, isothermal temperature, space-time, and catalyst mass per membrane surface area while decreasing the membrane thickness and channel height can raise the methane conversion and the C_{2+} yield. The averaged sensitivity results show that the membrane reactor is most sensitive to the operating temperature. Higher operating temperature leads to faster surface kinetics, and therefore, methane is consumed faster with

the increase of oxygen flux. A 10 % increase in the isothermal temperature led to a 79 % increase in the methane conversion and a 58 % increase in the C_{2+} yield.

Finally, it was concluded that incorporating membrane in an OCM reactor could help improve the methane conversion, accompanied by a 2 % absolute percentage increase in the C_{2+} yield and a 1.30 % absolute percentage increase in C_{2+} selectivity. However, the membrane reactor shows a higher selectivity towards CO_x with a 22.62 % absolute percentage increase in CO_x selectivity. This increase in CO_x output can hinder the adaption of this technology on a larger scale due to its environmental effects.

Estimating the C_{2+} yield and selectivity required to achieve an industrially favorable price will conclude that this research's OCM membrane reactor technology is economically feasible. Although the estimation does not cover all financial matters, it is a good indicator for choosing among alternatives and finding out which part of the process should be improved. It was concluded that around 25 % of C_{2+} yield and 22 % of C_{2+} selectivity were needed to maintain the overall ethylene price of around 1128.99 US $/ton of C_2H_4, which is below the industrial limit indicated by Cruellas et al. [59] techno economics model.

5.2 Recommendations for future work

Several implementations can further improve the obtained membrane reactors' performance criteria and help further examine the feasibility of the technology presented in this research:

(1) Examining further OCM catalysts can be part of future work concerning the implementation of OCM in catalytic membrane reactors. As explained in *Chapter 2*, using an appropriate catalyst in OCM reaction is crucial to the overall process. It can ease breaking a C-H bond in a methane molecule (CH_4) and dimerizing methyl radicals (CH_3). These are susceptible to the coupling reaction toward higher hydrocarbons such as ethane and ethylene while minimizing the carbon monoxide bond (C-O) formation at high conversion levels. Applying the reaction network for a more selective OCM catalyst in a one-dimensional model can positively impact the results by improving the surface kinetics. Several catalyst show good selectivity towards C_{2+} and a relatively higher methane conversion [131] [98] [132] [133] [134]. For instance, The $Mn/Na_2WO_4/SiO_2$ catalyst is one of the most effective catalysts for the OCM reaction. Selectivity of 66.9 % C_{2+} at 37.7 % CH_4 conversion, 80 % C_{2+} selectivity at 20 % CH_4 conversion, and 80 % C_{2+} selectivity at 33 % CH_4 conversion with excellent catalyst stability can nominate this catalyst to be an excellent

candidate. In addition, the usage of barium-based perovskite (BSCF) membrane can help increase hydrogen production on the feed side. As explained in *Chapter 1*, BSCF exhibits a high oxygen permeation rate. According to studies [79], the continuous removal of oxygen from water dissociation will lead to continuously shifting the equilibrium to the product side; in other words, increasing hydrogen production.

(2) Developing a 3D catalytic oxygen-permeable membrane reactor model that builds on the 1D model investigated in this research can help investigate this technology further. Enabling factors like adiabatic temperature along the sweep and feed sides will make the model more realistic and closer to reality.

(3) In order to examine the feasibility of the technology presented in this research, a techno-economic analysis should be developed to build on the ethylene price estimation shown in this research. The techno-economic model will allow the development of a cost-effective membrane reactor system and plant, which will justify implementing this co-production process versus other conventional production processes, such as steam methane reforming and ethane cracking. The complete techno-economic analysis should include initial capital costs and energy requirements for each stage of the OCM process.

Bibliography

[1] IEA, Technology Roadmap Hydrogen and Fuel Cells, (2015). https://www.iea.org/reports/technology-roadmap-hydrogen-and-fuel-cells.

[2] S. Koumi Ngoh, D. Njomo, An overview of hydrogen gas production from solar energy, Renew. Sustain. Energy Rev. 16 (2012) 6782–6792. https://doi.org/https://doi.org/10.1016/j.rser.2012.07.027.

[3] I.E. Agency, World Energy Outlook-2017, (2017).

[4] A. Alshammari, V.N. Kalevaru, A. Bagabas, A. Martin, Production of ethylene and its commercial importance in the global market, 2016. https://doi.org/10.4018/978-1-4666-9975-5.ch004.

[5] METI, Forecast of Global Supply and Demand Trends for Petrochemical Products (from 2010 to 2023), (2019). https://www.meti.go.jp/english/press/2019/1017_001.html.

[6] Siluria, Ethylene Industry, (2020). https://siluria.com/Commercial_Applications/Ethylene_Industry.

[7] T. Ren, M.K. Patel, K. Blok, Steam cracking and methane to olefins: Energy use, CO2 emissions and production costs, Energy. 33 (2008) 817–833. https://doi.org/10.1016/j.energy.2008.01.002.

[8] G. Radaelli, Low-Energy , Low-Cost Production of Ethylene by Low- Temperature Oxidative Coupling of Methane Final Technical Report, (2017).

[9] H. Schmalz, T. Wirth, Ullmann's Encyclopedia of Industrial Chemistry, (2003) 335521.

[10] A. Greenwood, ICIS, Fears of US ethane price spike overblown, (2016). https://www.icis.com/explore/resources/news/2016/09/06/10031804/fears-of-us-ethane-price-spike-overblown-analyst/.

[11] C.A. Gärtner, A.C. vanVeen, J.A. Lercher, Oxidative dehydrogenation of ethane: Common principles and mechanistic aspects, ChemCatChem. 5 (2013) 3196–3217. https://doi.org/10.1002/cctc.201200966.

[12] N. Wo, M. Neumann, Oxidative coupling of methane : Resolution of the surface and gas phase contributions to the mechanism of the oxidative coupling of methane at, (2016).

[13] S. Parishan, P. Littlewood, A. Arinchtein, V. Fleischer, R. Schomäcker, Chemical looping as a reactor concept for the oxidative coupling of methane over the MnxOy-Na2WO4/SiO2 catalyst, benefits and limitation, Catal. Today. 311 (2018) 40–47. https://doi.org/10.1016/j.cattod.2017.08.019.

[14] A.S. Bodke, D.A. Olschki, L.D. Schmidt, E. Ranzi, High selectivities to ethylene by partial oxidation of ethane, Science (80-.). 285 (1999) 712–715. https://doi.org/10.1126/science.285.5428.712.

[15] X.S. Nghiem, Ethylene Production by Oxidative Coupling of Methane : New Process Flow Diagram Based on Adsorptive Separation, Dr. Thesis, Tech. Univ. Berlin, Fak. III - Prozesswissenschaften. (2014).

[16] V. Spallina, I.C. Velarde, J.A.M. Jimenez, H.R. Godini, F. Gallucci, M. Van Sint Annaland, Techno-economic assessment of different routes for olefins production through the oxidative coupling of methane (OCM): Advances in benchmark technologies, Energy Convers. Manag. 154 (2017) 244–261. https://doi.org/10.1016/j.enconman.2017.10.061.

[17] N. Sönnichsen, Natural gas consumption worldwide from 1998 to 2019 (in billion cubic meters), (2021). https://www.statista.com/statistics/282717/global-natural-gas-consumption/.

[18] A.F. Ghoniem, Needs, resources and climate change: Clean and efficient conversion technologies, Prog. Energy Combust. Sci. 37 (2011) 15–51. https://doi.org/10.1016/j.pecs.2010.02.006.

[19] M. Ewing, B. Israel, T. Jutt, H. Talebian, L. Stepanik, Hydrogen on the path to net-zero emissions Costs and climate benefits, Pembin. Inst. (2020). https://www.pembina.org/pub/hydrogen-primer.

[20] X. Zhang, R. You, Z. Wei, X. Jiang, J. Yang, Y. Pan, P. Wu, Q. Jia, Z. Bao, L. Bai, M. Jin, B. Sumpter, V. Fung, W. Huang, Z. Wu, Radical Chemistry and Reaction Mechanisms of Propane Oxidative Dehydrogenation over Hexagonal Boron Nitride Catalysts, Angew. Chemie - Int. Ed. 59 (2020) 8042–8046. https://doi.org/10.1002/anie.202002440.

[21] Natural Resources Canada, 2019 Hydrogen Pathways, Enabling a clean growth future for Canadians, (2019) 103. https://www.nrcan.gc.ca/energy-efficiency/transportation-alternative-fuels/resource-library/2019-hydrogen-pathways-enabling-clean-growth-future-for-

canadians/21961.

[22] CCC, UK regulations: the Climate Change Act, Comm. Clim. Chang. (2018). https://www.theccc.org.uk/the-need-to-act/a-legal-duty-to-act/.

[23] M. Jensterle, J. Narita, R. Piria, S. Samadi, M. Prantner, K. Crone, S. Siegemund, S. Kan, T. Matsumoto, Y. Shibata, The role of clean hydrogen in the future energy systems of Japan and Germany, Berlin: Adelphi. (2019).

[24] M. Ghazvini, M. Sadeghzadeh, M.H. Ahmadi, S. Moosavi, F. Pourfayaz, Geothermal energy use in hydrogen production: A review, Int. J. Energy Res. 43 (2019) 7823–7851. https://doi.org/10.1002/er.4778.

[25] Office of Energy Efficiency and Renewable Energy, Hydrogen Production: Natural Gas Reforming, United States Dep. Energy. (n.d.). https://www.energy.gov/eere/fuelcells/hydrogen-production-natural-gas-reforming.

[26] D.G. Rethwisch, J.A. Dumesic, The effects of metal-oxygen bond strength on properties of oxides: II. Water-gas shift over bulk oxides, Appl. Catal. 21 (1986) 97–109. https://doi.org/10.1016/S0166-9834(00)81331-7.

[27] D.C. Grenoble, M.M. Estadt, D.F. Ollis, The chemistry and catalysis of the water gas shift reaction. 1. The kinetics over supported metal catalysts, J. Catal. 67 (1981) 90–102. https://doi.org/10.1016/0021-9517(81)90263-3.

[28] A. Boudjemaa, A. Auroux, S. Boumaza, M. Trari, O. Cherifi, R. Bouarab, Hydrogen production on iron-magnesium oxide in the high-temperature water-gas shift reaction, React. Kinet. Catal. Lett. 98 (2009) 319–325. https://doi.org/10.1007/s11144-009-0084-3.

[29] N.E. Amadeo, M.A. Laborde, Hydrogen production from the low-temperature water-gas shift reaction: Kinetics and simulation of the industrial reactor, Int. J. Hydrogen Energy. 20 (1995) 949–956. https://doi.org/10.1016/0360-3199(94)00130-R.

[30] R. Bouarab, S. Bennici, C. Mirodatos, A. Auroux, Hydrogen Production from the Water-Gas Shift Reaction on Iron Oxide Catalysts, J. Catal. 2014 (2014) 1–6. https://doi.org/10.1155/2014/612575.

[31] K. Yamashita, L. Barreto, Energyplexes for the 21st century: Coal gasification for co-producing hydrogen, electricity and liquid fuels, Energy. 30 (2005) 2453–2473.

https://doi.org/10.1016/j.energy.2004.12.002.

[32] C. Higman, S. Tam, Advances in coal gasification, hydrogenation, and gas treating for the production of chemicals and fuels, Chem. Rev. 114 (2014) 1673–1708. https://doi.org/10.1021/cr400202m.

[33] Office of Energy Efficiency and Renewable Energy, Hydrogen Production: Coal Gasification, United States Dep. Energy. (2016). https://www.energy.gov/eere/fuelcells/hydrogen-production-coal-gasification.

[34] P. Rezaee, H.R. Naeij, A new approach to separate hydrogen from carbon dioxide using graphdiyne-like membrane, Sci. Rep. 10 (2020) 1–13. https://doi.org/10.1038/s41598-020-69933-9.

[35] X.-Y. Wu, L. Cai, X. Zhu, A.F. Ghoniem, W. Yang, A high-efficiency novel IGCC-OTM carbon capture power plant design, J. Adv. Manuf. Process. 2 (2020) e10059. https://doi.org/https://doi.org/10.1002/amp2.10059.

[36] L. Cai, X.Y. Wu, X. Zhu, A.F. Ghoniem, W. Yang, High-performance oxygen transport membrane reactors integrated with IGCC for carbon capture, AIChE J. 66 (2020). https://doi.org/10.1002/aic.16247.

[37] A.F.G. Xiao-Yu Wu, Yudong Chen, Design and cost analysis of perovskite oxygen permeable membrane reactors for hydrogen and syngas co-production, Dep. Mech. Eng. Massachusetts Inst. Technol. (2012). https://doi.org/10.1017/CBO9781107415324.004.

[38] F. Elmanakhly, A. DaCosta, B. Berry, R. Stasko, M. Fowler, X.Y. Wu, Hydrogen economy transition plan: A case study on Ontario, AIMS Energy. 9 (2021) 775–811. https://doi.org/10.3934/ENERGY.2021036.

[39] P. Nikolaidis, A. Poullikkas, A comparative overview of hydrogen production processes, Renew. Sustain. Energy Rev. 67 (2017) 597–611. https://doi.org/https://doi.org/10.1016/j.rser.2016.09.044.

[40] A. Buttler, H. Spliethoff, Current status of water electrolysis for energy storage, grid balancing and sector coupling via power-to-gas and power-to-liquids: A review, Renew. Sustain. Energy Rev. 82 (2018) 2440–2454. https://doi.org/10.1016/j.rser.2017.09.003.

[41] J.R. Bartels, M.B. Pate, N.K. Olson, An economic survey of hydrogen production from

conventional and alternative energy sources, Int. J. Hydrogen Energy. 35 (2010) 8371–8384. https://doi.org/https://doi.org/10.1016/j.ijhydene.2010.04.035.

[42] E. Cetinkaya, I. Dincer, G.F. Naterer, Life cycle assessment of various hydrogen production methods, Int. J. Hydrogen Energy. 37 (2012) 2071–2080. https://doi.org/10.1016/j.ijhydene.2011.10.064.

[43] U.D. of Energy, Hydrogen & Fuel Cells Program, (n.d.). https://www.hydrogen.energy.gov/.

[44] B. Olateju, J. Monds, A. Kumar, Large scale hydrogen production from wind energy for the upgrading of bitumen from oil sands, Appl. Energy. 118 (2014) 48–56. https://doi.org/10.1016/j.apenergy.2013.12.013.

[45] BBC, Coal gasification: The clean energy of the future?, (2014). https://www.bbc.com/news/business-26921145.

[46] F. Ognissanto, T. Landen, A. Stevens, M. Emre, D. Naberezhnykh, Evaluation of the CO2 emissions pathway from hydrogen production to fuel cell car utilisation, The Institution of Engineering and Technology, 2017. https://doi.org/10.1049/iet-its.2016.0210.

[47] K. Scott, Introduction to Electrolysis, Electrolysers and Hydrogen Production, in: Royal Society of Chemistry, 2019: pp. 1–27. https://doi.org/10.1039/9781788016049-00001.

[48] D. Akal, S. Öztuna, M.K. Büyükakın, A review of hydrogen usage in internal combustion engines (gasoline-Lpg-diesel) from combustion performance aspect, Int. J. Hydrogen Energy. (2020) 1–12. https://doi.org/10.1016/j.ijhydene.2020.02.001.

[49] IEA, The clean hydrogen future has already begun, (2019). https://www.iea.org/commentaries/the-clean-hydrogen-future-has-already-begun.

[50] K. Huang, J.B. Miller, G.W. Huber, J.A. Dumesic, C.T. Maravelias, A General Framework for the Evaluation of Direct Nonoxidative Methane Conversion Strategies, Joule. 2 (2018) 349–365. https://doi.org/10.1016/j.joule.2018.01.001.

[51] American chemistry, OLEFINS, (2021). https://www.americanchemistry.com/ProductsTechnology/Olefins/#:~:text=Olefins are a class of,and 1%2C3-butadiene.

[52] P. Tian, Y. Wei, M. Ye, Z. Liu, Methanol to olefins (MTO): From fundamentals to commercialization, ACS Catal. 5 (2015) 1922–1938.

https://doi.org/10.1021/acscatal.5b00007.

[53] A. Holmen, Direct conversion of methane to fuels and chemicals, Catal. Today. 142 (2009) 2–8. https://doi.org/10.1016/j.cattod.2009.01.004.

[54] M.C. Alvarez-Galvan, N. Mota, M. Ojeda, S. Rojas, R.M. Navarro, J.L.G. Fierro, Direct methane conversion routes to chemicals and fuels, Catal. Today. 171 (2011) 15–23. https://doi.org/10.1016/j.cattod.2011.02.028.

[55] J.J. Spivey, G. Hutchings, Catalytic aromatization of methane, Chem. Soc. Rev. 43 (2014) 792–803. https://doi.org/10.1039/c3cs60259a.

[56] Z. Cao, H. Jiang, H. Luo, S. Baumann, W.A. Meulenberg, J. Assmann, L. Mleczko, Y. Liu, J. Caro, Natural gas to fuels and chemicals: Improved methane aromatization in an oxygen-permeable membrane reactor, Angew. Chemie - Int. Ed. 52 (2013) 13794–13797. https://doi.org/10.1002/anie.201307935.

[57] J. Xue, Y. Chen, Y. Wei, A. Feldhoff, H. Wang, J. Caro, Gas to Liquids: Natural Gas Conversion to Aromatic Fuels and Chemicals in a Hydrogen-Permeable Ceramic Hollow Fiber Membrane Reactor, ACS Catal. 6 (2016) 2448–2451. https://doi.org/10.1021/acscatal.6b00004.

[58] T. Jiang, J. Song, M. Huo, N.T. Yang, J. Liu, J. Zhang, Y. Sun, Y. Zhu, La2O3 catalysts with ((diverse spatial dimensionality)) for oxidative coupling of methane to produce ethylene and ethane, RSC Adv. 6 (2016) 34872–34876. https://doi.org/10.1039/c6ra01805j.

[59] A. Cruellas, J.J. Bakker, M. van Sint Annaland, J.A. Medrano, F. Gallucci, Techno-economic analysis of oxidative coupling of methane: Current state of the art and future perspectives, Energy Convers. Manag. 198 (2019) 111789. https://doi.org/10.1016/j.enconman.2019.111789.

[60] Y. Simon, F. Baronnet, P.M. Marquaire, Kinetic modeling of the oxidative coupling of methane La2O3, Ind. Eng. Chem. Res. 46 (2007) 1914–1922. https://doi.org/10.1021/ie060151w.

[61] B. Zohour, Oxidative Coupling of Methane using Nanofiber Catalysts and Discovery of Catalysts for Atmospheric Reduction of CO2 to Methanol, J. Phys. A Math. Theor. 44 (2017) 1–8. https://doi.org/10.1088/1751-8113/44/8/085201.

[62] J.H. Lunsford, The Catalytic Oxidative Coupling of Methane, Angew. Chemie Int. Ed. English. 34 (1995) 970–980. https://doi.org/10.1002/anie.199509701.

[63] L. Mleczko, U. Pannek, M. Rothaemel, M. Baerns, Oxidative Coupling of Methane over a La2O3/CaO Catalyst. Optimization of Reaction Conditions in a Bubbling Fluidized-bed Reactor, Can. J. Chem. Eng. 74 (1996) 279–287. https://doi.org/10.1002/cjce.5450740213.

[64] U. Zavyalova, M. Holena, R. Schlögl, M. Baerns, Statistical analysis of past catalytic data on oxidative methane coupling for new insights into the composition of high-performance catalysts, ChemCatChem. 3 (2011) 1935–1947. https://doi.org/10.1002/cctc.201100186.

[65] S.J. Conway, D.J. Wang, J.H. Lunsford, Selective oxidation of methane and ethane over Li+-MgO-Cl- catalysts promoted with metal oxides, Appl. Catal. A, Gen. 79 (1991) 0–4. https://doi.org/10.1016/0926-860X(91)85001-E.

[66] S. Jašo, H.R. Godini, H. Arellano-Garcia, M. Omidkhah, G. Wozny, Analysis of attainable reactor performance for the oxidative methane coupling process, Chem. Eng. Sci. 65 (2010) 6341–6352. https://doi.org/10.1016/j.ces.2010.08.019.

[67] J.C.W. Kuo, C.T. Kresge, R.E. Palermo, Evaluation of direct methane conversion to higher hydrocarbons and oxygenates, Catal. Today. 4 (1989) 463–470. https://doi.org/10.1016/0920-5861(89)85042-4.

[68] O. Czuprat, T. Schiestel, H. Voss, J. Caro, Oxidative coupling of methane in a BCFZ perovskite hollow fiber membrane reactor, Ind. Eng. Chem. Res. 49 (2010) 10230–10236. https://doi.org/10.1021/ie100282g.

[69] X. Tan, K. Li, Inorganic Membrane Reactors: Fundamentals and Applications, 2015. https://doi.org/10.1002/9781118672839.

[70] P. Zhu, I. Falls, Ceramic Membranes for Permeation, 2008.

[71] E.A. Hazbun, CERAMC MEMBRANE AND USE THEREOF FOR HYDROCARBON CONVERSION, (1989).

[72] A.A. Plazaola, A.C. Labella, Y. Liu, N.B. Porras, D.A.P. Tanaka, M.V.S. Annaland, F. Gallucci, Mixed ionic-electronic conducting membranes (MIEC) for their application in membrane reactors: A review, Processes. 7 (2019). https://doi.org/10.3390/pr7030128.

[73] J. Sunarso, S. Baumann, J.M. Serra, W.A. Meulenberg, S. Liu, Y.S. Lin, J.C. Diniz da Costa,

Mixed ionic-electronic conducting (MIEC) ceramic-based membranes for oxygen separation, J. Memb. Sci. 320 (2008) 13–41. https://doi.org/10.1016/j.memsci.2008.03.074.

[74] X.Y. Wu, L. Chang, M. Uddi, P. Kirchen, A.F. Ghoniem, Toward enhanced hydrogen generation from water using oxygen permeating LCF membranes, Phys. Chem. Chem. Phys. 17 (2015) 10093–10107. https://doi.org/10.1039/c5cp00584a.

[75] P. Bernardo, E. Drioli, Membrane engineering for a sustainable production of ethylene, Fuel Process. Technol. 212 (2021) 106624. https://doi.org/10.1016/j.fuproc.2020.106624.

[76] X.-Y. Wu, Y. Luo, F. Hess, W. Lipiński, Editorial: Sustainable Hydrogen for Energy, Fuel and Commodity Applications, Front. Energy Res. . 9 (2021) 231.

[77] N.I. Il'chenko, Y.I. Pyatnitskij, N. V. Pavlenko, Oxidative coupling of methane on metal-like catalysts, Ukr. Khimicheskij Zhurnal. 67 (2001) 40–48.

[78] W. Yao, H. Cheng, P. Wang, X. Lu, X. Zou, Q. Xu, Hydrogen Production by Catalytic Partial Oxidation of Coke Oven Gas in BaCo0.7Fe0.3-xZrxO3-δ Ceramic Membrane Reactors, MATEC Web Conf. 67 (2016) 6–11. https://doi.org/10.1051/matecconf/20166704002.

[79] H. Jiang, H. Wang, F. Liang, S. Werth, S. Schirrmeister, T. Schiestel, J. Caro, Improved water dissociation and nitrous oxide decomposition by in situ oxygen removal in perovskite catalytic membrane reactor, Catal. Today. 156 (2010) 187–190. https://doi.org/10.1016/j.cattod.2010.02.027.

[80] X.Y. Wu, L. Chang, M. Uddi, P. Kirchen, A.F. Ghoniem, Toward enhanced hydrogen generation from water using oxygen permeating LCF membranes, Phys. Chem. Chem. Phys. 17 (2015) 10093–10107. https://doi.org/10.1039/c5cp00584a.

[81] R.D. Shannon, Revised effective ionic radii in halides and chalcogenides, Acta Crystallogr. A32 (1976) 751–767.

[82] H.S. Fogler, Elements of Reaction Engineering, 4th ed., 2006. https://learning-oreilly-com.proxy.lib.uwaterloo.ca/library/view/elements-of-chemical/9780133887822/ch01.xhtml.

[83] J.N. Armor, Applications of catalytic inorganic membrane reactors to refinery products, (1998) 1999.

[84] J.A. Lane, J.A. Kilner, Oxygen surface exchange on gadolinia doped ceria, Solid State Ionics. 136–137 (2000) 927–932. https://doi.org/10.1016/S0167-2738(00)00530-0.

[85] P.J. Gellings, H.J.M. Bouwmeester, Ion and mixed conducting oxides as catalysts, Catal. Today. 12 (1992) 1–101. https://doi.org/10.1016/0920-5861(92)80046-P.

[86] R. V. Franca, A. Thursfield, I.S. Metcalfe, La 0.6Sr 0.4Co 0.2Fe 0.8O 3-δ microtubular membranes for hydrogen production from water splitting, J. Memb. Sci. 389 (2012) 173–181. https://doi.org/10.1016/j.memsci.2011.10.027.

[87] F.A. Kroger, H.J. Vink, Relations between the Concentrations of Imperfections in Crystalline Solids, in: N.Y. Academic (Ed.), Solid State Phys. Adv. Res. Appl. Vol. 3, Vol. 3, 1956: pp. 307–435. https://doi.org/10.1016/S0081-1947(08)60135-6.

[88] Y. Liu, X. Tan, K. Li, Mixed conducting ceramics for catalytic membrane processing, Catal. Rev. - Sci. Eng. 48 (2006) 145–198. https://doi.org/10.1080/01614940600631348.

[89] S.Z. Baykara, Experimental solar water thermolysis, Int. J. Hydrogen Energy. 29 (2004) 1459–1469. https://doi.org/10.1016/j.ijhydene.2004.02.011.

[90] H.H.G. Jellinek, H. Kachi, The catalytic thermal decomposition of water and the production of hydrogen, Int. J. Hydrogen Energy. 9 (1984) 677–688. https://doi.org/10.1016/0360-3199(84)90265-9.

[91] Z. Stansch, L. Mleczko M, Baerns, Comprehensive Kinetics of Oxidative Coupling of Methane over the La2O3/CaO Catalyst, Ind. Eng. Chem. Res. 36 (1997) 2568–2579. https://doi.org/10.1021/ie960562k.

[92] V.I. Lomonosov, M.Y. Sinev, Oxidative coupling of methane: Mechanism and kinetics, Kinet. Catal. 57 (2016) 647–676. https://doi.org/10.1134/S0023158416050128.

[93] V.I. Alexiadis, T. Serres, G.B. Marin, C. Mirodatos, J.W. Thybaut, Y. Schuurman, Analysis of volume-to-surface ratio effects on methane oxidative coupling using microkinetic modeling, AIChE J. 64 (2018) 2603–2611. https://doi.org/10.1002/aic.16152.

[94] T. Le Van, C. Louis, M. Kermarec, M. Che, J.M. Tatibouët, Temperature and conversion dependence of selectivities in the oxidative coupling of methane on La2O3 catalysts, Catal. Today. 13 (1992) 321–328. https://doi.org/10.1016/0920-5861(92)80156-H.

[95] B. Pascal, L. Yongdan, M. Paul-Marie, C. Guy-Marie, B. FranGois, Competition between the gas and surface reactions for the oxidative coupling of methane, Appl. Catal. 29 (1994) 190. https://doi.org/10.1016/S0166-9834(00)82623-8.

[96] G.M. Côme, Y. Li, P. Barbe, N. Gueritey, P.M. Marquaire, F. Baronnet, Competition between gas and surface reactions in the oxidative coupling of methane 2. Isothermal experiments in a catalytic jet-stirred gas phase reactor, Catal. Today. 30 (1996) 215–222. https://doi.org/10.1016/0920-5861(96)00012-0.

[97] A.H. Weiss, J. Cook, R. Holmes, N. Davidova, P. Kovacheva, M. Traikova, Low Temperature Oxidative Coupling of Methane over a La2O3 Catalyst, 2 (1990) 243–253. https://doi.org/10.1021/bk-1990-0437.ch022.

[98] M. Daneshpayeh, A. Khodadadi, N. Mostoufi, Y. Mortazavi, R. Sotudeh-Gharebagh, A. Talebizadeh, Kinetic modeling of oxidative coupling of methane over Mn/Na2WO4/SiO2 catalyst, Fuel Process. Technol. 90 (2009) 403–410. https://doi.org/10.1016/j.fuproc.2008.11.001.

[99] L. Yu, W. Li, V. Ducarme, C. Mirodatos, G.A. Martin, Inhibition of gas-phase oxidation of ethylene in the oxidative conversion of methane and ethane over CaO, La2O3/CaO and SrO-La2O3/CaO catalysts, Appl. Catal. A Gen. 175 (1998) 173–179. https://doi.org/10.1016/S0926-860X(98)00208-7.

[100] T.T. Ching, A.R. Mohamed, S. Bhatia, Modeling of catalytic reactor for oxidative coupling of methane using La2O3/CaO catalyst, Chem. Eng. J. 87 (2002) 49–59. https://doi.org/10.1016/S1385-8947(01)00191-7.

[101] T.H. Etsell, S.N. Flengas, The Electrical Properties of Lanthanum Oxide-Calcium Oxide Solid Electrolytes, J. Electrochem. Soc. 116 (1969) 771. https://doi.org/10.1149/1.2412050.

[102] H.S. Fogler, Essentials of Chemical Reaction Engineering, second edition, Pearson, 2017.

[103] Hugh Stott Taylor, A theory of the catalytic surface, R. Soc. 108 (1925). https://doi.org/https://doi.org/10.1098/rspa.1925.0061.

[104] L. Shenggang, D.A. Dixon, Mechanism of oxide-catalyzed selective oxidation: A computational perspective, in: D.A. Dixon (Ed.), Annu. Rep. Comput. Chem., Elsevier, 2019: pp. 287–333. https://doi.org/https://doi.org/10.1016/bs.arcc.2019.08.007.

[105] M.S. Palmer, M. Neurock, M.M. Olken, Periodic density functional theory study of methane activation over La2O3: Activity of O2-, O-, O22-, oxygen point defect, and Sr2+-doped surface sites, J. Am. Chem. Soc. 124 (2002) 8452–8461. https://doi.org/10.1021/ja0121235.

[106] J. Keith, Physical chemistry, 1999.

[107] J. Ross, Heterogeneous Catalysis - Fundamentals and Applications, Elsevier, 2012. https://app.knovel.com/hotlink/pdf/id:kt009GDRN2/heterogeneous-catalysis/introduction.

[108] J. Hong, P. Kirchen, A.F. Ghoniem, Analysis of heterogeneous oxygen exchange and fuel oxidation on the catalytic surface of perovskite membranes, J. Memb. Sci. 445 (2013) 96–106. https://doi.org/10.1016/j.memsci.2013.05.055.

[109] A.S. Yu, J. Kim, T.S. Oh, G. Kim, R.J. Gorte, J.M. Vohs, Decreasing interfacial losses with catalysts in La0.9Ca0.1FeO3-δ membranes for syngas production, Appl. Catal. A Gen. 486 (2014) 259–265. https://doi.org/10.1016/j.apcata.2014.08.028.

[110] Z. Zhao, C.O. Iloeje, T. Chen, A.F. Ghoniem, Design of a rotary reactor for chemical-looping combustion. Part 1: Fundamentals and design methodology, Fuel. 121 (2014) 327–343. https://doi.org/10.1016/j.fuel.2013.11.056.

[111] E.J. Sheu, A.F. Ghoniem, Receiver reactor concept and model development for a solar steam redox reformer, Sol. Energy. 125 (2016) 339–359. https://doi.org/10.1016/j.solener.2015.12.024.

[112] S. Liu, X. Tan, K. Li, R. Hughes, Methane coupling using catalytic membrane reactors, Catal. Rev. - Sci. Eng. 43 (2001) 147–198. https://doi.org/10.1081/CR-100104388.

[113] W.R. Bussman, C.E. Baukal, Ambient conditions impact CO and NOx emissions: Part II, Pet. Technol. Q. 14 (2009) 37–41.

[114] W. Betteridge, J. Hope, Separation of Hydrogen From Gas Mixtures., Platin. Met. Rev. 19 (1975) 50–59.

[115] W. Li, Z. Cao, L. Cai, L. Zhang, X. Zhu, W. Yang, H2S-tolerant oxygen-permeable ceramic membranes for hydrogen separation with a performance comparable to those of palladium-based membranes, Energy Environ. Sci. 10 (2017) 101–106. https://doi.org/10.1039/c6ee02967a.

[116] G. Pecchi, M.G. Jiliberto, A. Buljan, E.J. Delgado, Relation between defects and catalytic activity of calcium doped LaFeO 3 perovskite, Solid State Ionics. 187 (2011) 27–32. https://doi.org/10.1016/j.ssi.2011.02.014.

[117] A. Hunt, Corrigendum to Measuring the oxygen profile and permeation flux across an ion

transport (LCF) membrane and the development and validation of a multistep surface exchange model [J. Membr. Sci. 468 (2014) 62-72], J. Memb. Sci. 479 (2015) 276–276. https://doi.org/10.1016/j.memsci.2015.01.011.

[118] R.K. Herz, Chemical Reaction Engineering - Part 13 - intro to Plug Flow Reactors, i (2014) 1–15.

[119] L. Mastropasqua, F. Drago, P. Chiesa, A. Giuffrida, Oxygen transport membranes for efficient glass melting, Membranes (Basel). 10 (2020) 1–32. https://doi.org/10.3390/membranes10120442.

[120] M.L. Rodríguez, D.E. Ardissone, E. López, M.N. Pedernera, D.O. Borio, Reactor designs for ethylene production via ethane oxidative dehydrogenation: Comparison of performance, Ind. Eng. Chem. Res. 50 (2011) 2690–2697. https://doi.org/10.1021/ie100738q.

[121] T. DiChristopher, Experts explain why green hydrogen costs have fallen and will keep falling, (n.d.). https://www.spglobal.com/marketintelligence/en/news-insights/latest-news-headlines/experts-explain-why-green-hydrogen-costs-have-fallen-and-will-keep-falling-63037203.

[122] G. Ulrich, P. Vasudevan, How to estimate utility costs, (2006). https://go-gale-com.proxy.lib.uwaterloo.ca/ps/retrieve.do?tabID=T002&resultListType=RESULT_LIST&searchResultsType=SingleTab&hitCount=1&searchType=AdvancedSearchForm&currentPosition=1&docId=GALE%7CA144981499&docType=Article&sort=RELEVANCE&contentSegment=ZO.

[123] C. of Toronto, 2020 Water Rates & Fees, (2020). https://www.toronto.ca/services-payments/property-taxes-utilities/utility-bill/water-rates-and-fees-copy/2020-water-rates-fees/.

[124] ALIBABA, Lanthanum Nitrate Price, (n.d.). https://www.alibaba.com/product-detail/LaNO33-99-9999-Purity-10277-43-7-Lanthanum-Nitrate_62560728094.html?mark=google_shopping&seo=1.

[125] ALIBABA, Calcium Nitrate, (n.d.). https://www.alibaba.com/product-detail/Calcium-Nitrate-99-Ca-NO3-2_60608190917.html?spm=a2700.7724857.normal_offer.d_title.2b56171e8AoK5E.

[126] ALIBABA, Industry Grade Ferric Nitrate Catalyst, (n.d.). https://www.alibaba.com/product-

detail/Industry-Grade-Ferric-Nitrate-Catalyst-Fe_62501021090.html?spm=a2700.7724857.normal_offer.d_title.77e82b0fCUzG60.

[127] ALIBABA, calcium oxide powder, (n.d.). https://www.alibaba.com/product-detail/Calcium-Oxide-Powder-Powder-Calcium-Oxide_62209334799.html?spm=a2700.galleryofferlist.normal_offer.d_title.53bc7481IaLhjZ&s=p.

[128] chemical-process-industry (CPI) professionals, THE CHEMICAL ENGINEERING PLANT COST INDEX, (2011). https://www.chemengonline.com/pci-home.

[129] ALIBABA, lanthanum oxide la2O3 powder, (n.d.). https://www.alibaba.com/product-detail/lanthanum-oxide-la2O3-powder_62356032581.html?mark=google_shopping&seo=1.

[130] H. ZIMMERMANN, R. WALZL, Ullmann's encyclopedia of industrial chemistry, Reprod. Dev. Toxicol. (2017) 797–809. https://doi.org/10.1016/B978-0-12-804239-7.00042-1.

[131] S. Lacombe, Z. Durjanova, L. Mleczko, C. Mirodatos, Kinetic modelling of the oxidative coupling of methane over lanthanum oxide in connection with mechanistic studies, Chem. Eng. Technol. 18 (1995) 216–223. https://doi.org/10.1002/ceat.270180311.

[132] A. Vatani, E. Jabbari, M. Askarieh, M.A. Torangi, Kinetic modeling of oxidative coupling of methane over Li/MgO catalyst by genetic algorithm, J. Nat. Gas Sci. Eng. 20 (2014) 347–356. https://doi.org/10.1016/j.jngse.2014.07.005.

[133] 2 Ali Farsi1, 2∗, Sattar Ghader1, Ali Moradi1, Seyed Soheil Mansouri1, 2, Vahid Shadravan1, 2011] 1. Department ofChemical Engineering, Shahid Bahonar University ofKerman, Kerman, Iran; 2. Young Researchers Society, Shahid Bahonar University ofKerman, Kerman, Iran [Manuscript received September 7, 2010; revised January 19, Abstract, La0.6Sr0.4Co0.8Fe0.2O3−δ nanocatalyst.pdf, (n.d.).

[134] S. Cheng, X. Shuai, Simulation of a catalytic membrane reactor for oxidative coupling of Methane, AIChE J. 41 (1995) 1598–1601. https://doi.org/10.1002/aic.690410625.

Appendix A

Influence of channel width

The channel width was altered between 5E-2 m (base case), 7E-2 m, and 9E-2 m. The inlet volumetric flow rate was recorded in the three cases and used to find the ratio between the two parameters. As shown in *Table A - 1*, $\dot{V}_{STP}/w_{membrane}$ is maintained constant. In order to validate the feed side accuracy, the ratio between the molar flow rate of hydrogen on the feed side and the channel width ($\Delta\dot{n}_{H_2}/w_{membrane}$) is calculated and plotted in *Figure A - 1*. As expected, the ratio obtained is consistent given that the $\dot{V}_{STP}/w_{membrane}$ is maintained constant and the channel width (membrane width) is altered. Similarly, the sweep side accuracy is validated by plotting the ratio between the molar flow rate of methane on the sweep side and the channel width ($\Delta\dot{n}_{CH_4}/w_{membrane}$). The trend also shows consistency of the $\Delta\dot{n}_{CH_4}/w_{membrane}$ as the channel width (membrane width) is altered between the three cases.

Table A - 1 : Change in channel width as $\dot{V}_{STP}/w_{channel}$ is constant

Case	Volumetric flow rate(inlet) [m^3/s]	$w_{channel}$ [m]	$\dot{V}_{STP}/w_{channel}$
Base case	7.23E-5	5E-2	1.4E-3
Case 1	1.01E-4	7E-2	1.4E-3
Case 2	1.30E-4	9E-2	1.4E-3

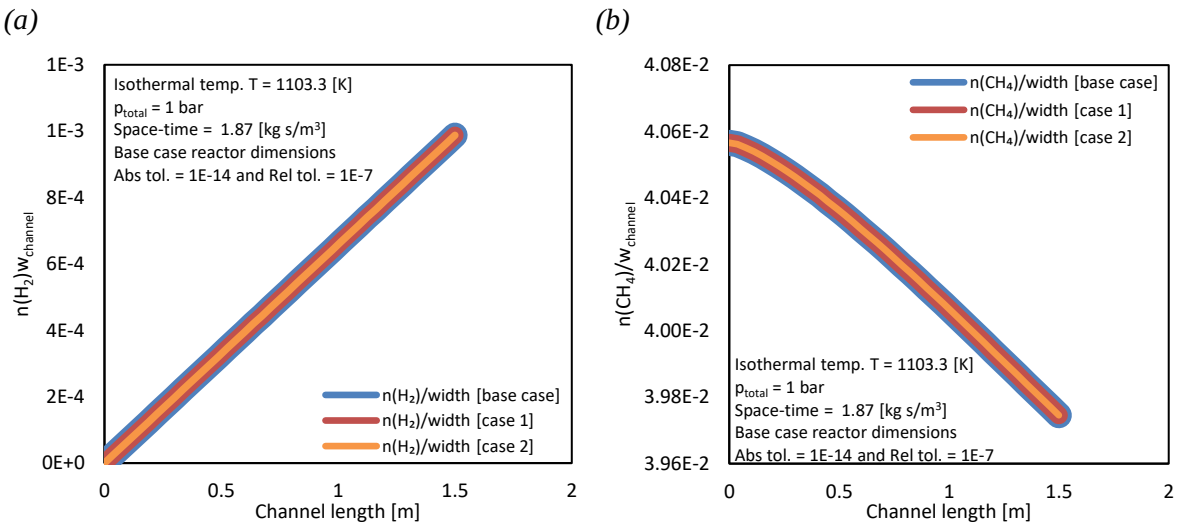

Figure A - 1 : Ratio between (a) $\dot{n}(H_2)$ and $w_{channel}$ (b) $\dot{n}(CH_4)$ and $w_{channel}$ along reactor length

Appendix B

Ethylene price estimation

(1) Catalyst

La_2O_3/caO catalyst pricing was estimated by collecting data from online vendors. La_2O_3 powder was found on Alibaba [129]. The cost of purified CaO is taken from the same source [129]. *Table B - 1* shows the estimated total cost of the catalyst.

Table B - 1: Total catalyst cost

Compound	Price/kg	Atomic concentration [%]	Amount of catalyst used [kg]	The actual price of each compound [$]	The total cost of catalyst [$]
La_2O_3	$5/kg	27	0.27	5	1.35
CaO	$0.9/kg	73	0.73	0.9	0.657

(2) Membrane

In order to estimate the total cost of the membrane (shown in *Table B - 2*), the average cost of all the salts needed to synthesize 1 kg of the membrane in $/kg is collected from online vendors. The amount to synthesize per kg of perovskite and the total weight of membrane needed are based on the membrane designed by Wu et al. [37]. The actual cost of salt is calculated as the product of the average cost and the amount required to synthesize 1 kg of perovskite. Lastly, the total cost is calculated using *Eqn.* (4-9).

Table B - 2: Total membrane cost

Required salts	Average cost [$/kg]	Required to synthesize 1 kg of perovskites [kg]	Total weight of membrane needed [kg/m^2]	Actual cost of the salts [$]	Total surface area membrane [m^2]	Total cost [$]
$La(NO_3)_3 \cdot 6H_2O$	$2.50	1.67		4.19		
$Ca(NO_3)_2 \cdot 4H_2O$	$0.29	0.10	5.76	0.029	0.0103	0.46
$Fe(NO_3)_3 \cdot 9H_2O$	$2.00	1.74		3.46		

(3) Inlet and outlet composition

Assuming that only two reactions occur, a direct OCM reaction from methane to ethylene is assumed, and methane to carbon dioxide is the combustion, as shown in *Eqn. (4-6)* and *Eqn. (4-15)*, respectively. In addition to assuming that complete water removal, inlet, and outlet compositions are calculated and summarized in *Table B - 3.*

According to estimation by Nghiem [15], assuming that only two reactions take place in the reactor and oxygen reacts fully, 1 mol of methane fed in the reactor will produce $\frac{Y_{C_2H_4}}{2}$ mol of ethylene and $X_{CH_4} - Y_{C_2H_4}$ mol of carbon dioxide, while 1-X_{CH_4} mol of methane remains unconverted. 1 mol of oxygen is consumed to produce 1 mol of ethylene. 2 mol of oxygen is consumed to produce 1 mol of carbon dioxide. Assuming total oxygen conversion, $2X_{CH_4}$-$1.5Y_{C_2H_4}$ mol of oxygen must be available along with 1 mol of methane to produce $\frac{Y_{C_2H_4}}{2}$ mol of ethylene and $X_{CH_4} - Y_{C_2H_4}$ mol of carbon dioxide.

Table B - 3 : Inlet and outlet composition

	Methane	**Oxygen**	**Ethylene**	**Carbon dioxide**	**Total**
Molecular mass					
Methane		16			
Oxygen		32			
Ethylene		28			
Carbon dioxide		44			
Methane feed, [mol]					
Inlet	1	2X-1.5Y	0	0	1+2X-1.5Y
Outlet	1-X	0	Y/2	X(1-S)	$1-\frac{Y}{2}$
Consumption	X	2X-1.5Y	0	0	3X-1.5Y
Ethylene production, [mol]					
Inlet	$\frac{2}{Y}$	$\frac{4-3S}{S}$	0	0	$\frac{2+4X-3X}{Y}$
Outlet	$\frac{2-2X}{Y}$	0	1	$\frac{2-2S}{S}$	$\frac{2-Y}{Y}$
Consumption	$\frac{2}{S}$	$\frac{4-3S}{S}$	0	0	$\frac{6-3S}{S}$
Ethylene production, [g]					
Inlet	$\frac{8}{7Y}$	$\frac{32-24S}{7S}$	0	0	$\frac{8+32X-24Y}{7Y}$
Outlet	$\frac{8-8X}{7Y}$	0	1	$\frac{22-22S}{7S}$	$\frac{8+14X-15Y}{7Y}$
Consumption	$\frac{8}{7S}$	$\frac{32-24S}{7S}$	0	0	$\frac{40-96S}{7S}$

** S and Y are selectivity and yield of ethylene, while X is the methane conversion.

Appendix C

Oxygen trend analysis

C.1. Initial trend

Table C - 1: Change in oxygen molar flow rate $\Delta\dot{n}$ (O_2), the destruction rate $\dot{W}(O_2)$, and oxygen flux (initial trend)

x [m]	Δx [m]	$\dot{W}_{O_2}$ [mol/s m]	$J_{O_2} \times w_{membrane}$ [mol/s m]	$\Delta\dot{n}_{O_2}$ [mol/s]
0	2.44E-6	0	4.57E-5	1.11E-10
2.44E-6	2.43E-6	-6.86E-7	4.57E-5	1.09E-10
4.87E-6	2.44E-6	-9.06E-7	4.57E-5	1.09E-10
7.31E-6	2.44E-6	-1.07E-6	4.57E-5	1.09E-10
9.75E-6	2.45E-6	-1.20E-6	4.57E-5	1.09E-10
1.22E-5	2.45E-6	-1.31E-6	4.57E-5	1.09E-10

Table C - 2 : Reaction rates along reactor length (initial trend)

x [m]	r_1	r_2	r_3	r_4	r_5	r_6
0	0	0	0	0	0	0
2.44E-6	1.45E-8	7.54E-6	1.33E-8	2.86E-16	2.48E-12	2.41E-19
4.87E-6	2.44E-8	9.92E-6	2.38E-8	1.56E-15	9.78E-12	2.95E-18
7.31E-6	3.31E-8	1.16E-5	3.36E-8	4.15E-15	2.03E-11	1.27E-17
9.75E-6	4.12E-8	1.30E-5	4.28E-8	8.27E-15	3.33E-11	3.48E-17
1.22E-5	4.87E-8	1.42E-5	5.16E-8	1.41E-14	4.89E-11	7.49E-17

* Reaction rates units: [mol /g s]

Table C - 3: Sweep side species partial pressures along reactor length (initial trend)

x [m]	P_{O_2}	P_{CH_4}	$P_{C_2H_4}$	P_{H_2O}	$P_{C_2H_6}$	P_{CO_2}	P_{H_2}	P_{CO}
0	0	7E+4	0	0	0	0	0	0
2.44E-6	3.67E-2	7E+4	4.30E-9	5.93E-4	5.90E-4	1.10E-6	1.00E-6	9.96E-7
4.87E-6	7.31E-2	7E+4	2.72E-8	1.92E-3	1.91E-3	3.98E-6	3.76E-6	3.73E-6
7.31E-6	1.09E-1	7E+4	7.94E-8	3.55E-3	3.53E-3	8.22E-6	8.02E-6	7.94E-6
9.75E-6	1.45E-1	7E+4	1.66E-7	5.36E-3	5.31E-3	1.36E-5	1.37E-5	1.35E-5
1.22E-5	1.81E-1	7E+4	2.89E-7	7.37E-3	7.31E-3	2.02E-5	2.07E-5	2.04E-5

* Partial pressures units: [Pa]

C.2. peak trend

Table C - 4: Change in oxygen molar flow rate $\Delta\dot{n}$ (O_2), the destruction rate $\dot{W}(O_2)$, and oxygen flux (peak)

x [m]	Δx [m]	$\dot{W}_{O_2}$[mol/s m]	$J_{O_2} \times w_{membrane}$ [mol/s m]	$\Delta\dot{n}_{O_2}$[mol/s]
4.9514E-2	1.1344E-3	-4.2856E-5	4.567E-5	3.1889E-9
5.0648E-2	1.1344E-3	-4.3384E-5	4.567E-5	2.5905E-9
5.1783E-2	1.1233E-3	-4.3898E-5	4.567E-5	1.9873E-9
5.2906E-2	1.1232E-3	-4.4399E-5	4.567E-5	1.4248E-9
5.4029E-2	1.1233E-3	-4.4885E-5	4.567E-5	8.7847E-10
5.5152E-2	1.1233E-3	-4.5357E-5	4.567E-5	3.4845E-10
5.6276E-2	1.1226E-3	-4.5814E-5	4.567E-5	-1.6451E-10
5.7398E-2	1.1227E-3	-4.6255E-5	4.567E-5	-6.5996E-10
5.8521E-2	1.1226E-3	-4.6681E-5	4.567E-5	-1.1375E-9
4.9514E-2	1.1226E-3	-4.7090E-5	4.567E-5	-1.5971E-9

Table C - 5 : Reaction rates along reactor length (peak)

x [m]	r_1	r_2	r_3	r_4	r_5	r_6
4.951E-2	1.258E-5	2.405E-4	2.557E-5	3.615E-6	2.671E-5	2.597E-5
5.065E-2	1.261E-5	2.407E-4	2.564E-5	3.814E-6	2.732E-5	2.713E-5
5.178E-2	1.264E-5	2.408E-4	2.569E-5	4.018E-6	2.791E-5	2.828E-5
5.291E-2	1.266E-5	2.408E-4	2.573E-5	4.227E-6	2.848E-5	2.944E-5
5.403E-2	1.267E-5	2.407E-4	2.576E-5	4.439E-6	2.905E-5	3.058E-5
5.515E-2	1.267E-5	2.406E-4	2.576E-5	4.656E-6	2.959E-5	3.172E-5
5.628E-2	1.267E-5	2.405E-4	2.576E-5	4.877E-6	3.013E-5	3.284E-5
5.740E-2	1.267E-5	2.403E-4	2.574E-5	5.101E-6	3.065E-5	3.396E-5
5.852E-2	1.265E-5	2.400E-4	2.571E-5	5.330E-6	3.115E-5	3.505E-5
4.951E-2	1.264E-5	2.397E-4	2.566E-5	5.558E-6	3.164E-5	3.610E-5

* Reaction rates units: [mol /g s]

Table C - 6: Sweep side species partial pressures along reactor length (peak)

x [m]	P_{O_2}	P_{CH_4}	$P_{C_2H_4}$	P_{H_2O}	$P_{C_2H_6}$	P_{CO_2}	P_{H_2}	P_{CO}
4.95E-2	2.73E+2	6.83E+4	9.34E+1	7.63E+2	4.63E+2	2.90E+1	1.33E+2	9.36E+1
5.06E-2	2.74E+2	6.83E+4	9.74E+1	7.87E+2	4.73E+2	3.01E+1	1.38E+2	9.86E+1
5.18E-2	2.75E+2	6.82E+4	1.02E+2	8.13E+2	4.84E+2	3.13E+1	1.44E+2	1.04E+2
5.29E-2	2.76E+2	6.82E+4	1.06E+2	8.38E+2	4.94E+2	3.24E+1	1.50E+2	1.09E+2
5.40E-2	2.76E+2	6.81E+4	1.10E+2	8.63E+2	5.04E+2	3.35E+1	1.56E+2	1.14E+2
5.52E-2	2.76E+2	6.81E+4	1.14E+2	8.89E+2	5.14E+2	3.47E+1	1.62E+2	1.20E+2
5.63E-2	2.76E+2	6.81E+4	1.18E+2	9.15E+2	5.23E+2	3.59E+1	1.68E+2	1.26E+2
5.74E-2	2.76E+2	6.80E+4	1.22E+2	9.40E+2	5.33E+2	3.71E+1	1.74E+2	1.31E+2
5.85E-2	2.76E+2	6.80E+4	1.27E+2	9.67E+2	5.42E+2	3.83E+1	1.81E+2	1.37E+2
4.95E-2	2.75E+2	6.79E+4	1.31E+2	9.93E+2	5.52E+2	3.95E+1	1.87E+2	1.43E+2

* Partial pressures units: [Pa]

Table C - 7: Oxygen flux permeation network parameters along reactor length (peak trend)

x [m]	C_{O_2} $(X_{O_2,surf} \times C_{sweep,total})$	C_{H_2O} $(X_{H_2O,surf} \times C_{feed,total})$	Chemical potential term	Oxygen flux [mol/m^2 s]
4.9514E-2	2.9085E+1	8.3315E+3	9.2273	4.567E-4
5.0648E-2	2.9161E+1	8.3279E+3	9.2152	4.567E-4
5.1783E-2	2.9217E+1	8.3242E+3	9.2064	4.567E-4
5.2906E-2	2.9253E+1	8.3206E+3	9.2007	4.567E-4
5.4029E-2	2.9271E+1	8.3170E+3	9.1979	4.567E-4
5.5152E-2	2.9271E+1	8.3134E+3	9.1980	4.567E-4
5.6276E-2	2.9253E+1	8.3097E+3	9.2007	4.567E-4
5.7398E-2	2.9219E+1	8.3061E+3	9.2061	4.567E-4
5.8521E-2	2.9169E+1	8.3025E+3	9.2140	4.567E-4
4.9514E-2	2.9103E+1	8.2989E+3	9.2244	4.567E-4

C.3. Valley

Table C - 8: Change in oxygen molar flow rate is affected by the destruction rate of oxygen and the oxygen flux along the reactor length (valley)

x [m]	Δx [m]	$\dot{W}_{O_2}$[mol/s m]	$J_{O_2} \times w_{membrane}$ [mol/s m]	$\Delta\dot{n}_{O_2}$[mol/s]
2.7732E-1	1.2658E-3	-4.5693E-5	4.566736254E-5	-3.2862E-11
2.7859E-1	1.2928E-3	-4.5685E-5	4.566736249E-5	-2.3335E-11
2.7988E-1	1.2928E-3	-4.5678E-5	4.566736245E-5	-1.3235E-11
2.8117E-1	1.2928E-3	-4.5669E-5	4.566736241E-5	-3.0458E-12
2.8247E-1	1.2928E-3	-4.5662E-5	4.566736236E-5	7.0156E-12
2.8376E-1	1.3217E-3	-4.5654E-5	4.566736232E-5	1.7331E-11
2.8508E-1	1.3217E-3	-4.5647E-5	4.566736228E-5	2.7364E-11

Table C - 9 : Reaction rates along reactor length (valley)

x [m]	r_1	r_2	r_3	r_4	r_5	r_6
2.773E-1	5.439E-6	1.406E-4	9.790E-6	3.198E-5	2.773E-1	5.439E-6
2.786E-1	5.436E-6	1.405E-4	9.782E-6	3.211E-5	2.786E-1	5.436E-6
2.799E-1	5.432E-6	1.404E-4	9.775E-6	3.223E-5	2.799E-1	5.432E-6
2.812E-1	5.429E-6	1.402E-4	9.768E-6	3.236E-5	2.812E-1	5.429E-6
2.825E-1	5.426E-6	1.401E-4	9.761E-6	3.249E-5	2.825E-1	5.426E-6
2.838E-1	5.423E-6	1.400E-4	9.755E-06	3.262E-5	2.838E-1	5.423E-6
2.851E-1	5.420E-6	1.398E-4	9.748E-6	3.274E-5	2.851E-1	5.420E-6

* Reaction rates units: [mol /g s]

Table C - 10 : Sweep side species partial pressures along reactor length (valley)

x [m]	P_{O_2}	P_{CH_4}	$P_{C_2H_4}$	P_{H_2O}	$P_{C_2H_6}$	P_{CO_2}	P_{H_2}	P_{CO}
4.95E-2	9.74E+1	6.03E+4	1.17E+3	5.34E+3	8.86E+2	4.63E+2	1.78E+3	1.49E+3
5.06E-2	9.74E+1	6.03E+4	1.17E+3	5.36E+3	8.86E+2	4.66E+2	1.79E+3	1.49E+3
5.18E-2	9.74E+1	6.03E+4	1.18E+3	5.39E+3	8.85E+2	4.70E+2	1.80E+3	1.50E+3
5.29E-2	9.73E+1	6.02E+4	1.18E+3	5.41E+3	8.85E+2	4.74E+2	1.81E+3	1.51E+3
5.40E-2	9.73E+1	6.02E+4	1.19E+3	5.43E+3	8.84E+2	4.77E+2	1.82E+3	1.51E+3
5.52E-2	9.73E+1	6.01E+4	1.19E+3	5.45E+3	8.83E+2	4.81E+2	1.83E+3	1.52E+3
5.63E-2	9.73E+1	6.01E+4	1.20E+3	5.47E+3	8.83E+2	4.85E+2	1.83E+3	1.53E+3
5.74E-2	9.74E+1	6.03E+4	1.17E+3	5.34E+3	8.86E+2	4.63E+2	1.78E+3	1.49E+3
5.85E-2	9.74E+1	6.03E+4	1.17E+3	5.36E+3	8.86E+2	4.66E+2	1.79E+3	1.49E+3
4.95E-2	9.74E+1	6.03E+4	1.18E+3	5.39E+3	8.85E+2	4.70E+2	1.80E+3	1.50E+3